Towards Smarter Rock Breakage

A Framework for Blast Design in Sublevel Stoping Using Fuzzy Logic and Measure While Drilling Data

AESM7000: Master Thesis

M.E.Y. de Jonge

Delft University of Technology

TU Delft

NEW BOLIDEN

Towards Smarter Rock Breakage

A Framework for Blast Design in Sublevel Stoping Using Fuzzy Logic and Measure While Drilling Data

by

M.E.Y. de Jonge

Student Name	Student Number
Maximiliaan de Jonge	4688643

Master Thesis

Presented at the Resource Engineering Department of the Faculty of Civil Engineering and Geosciences.

Delft University of Technology

to be defended publicly on Friday August 22nd, 2025 at 15:00.

In partial fulfillment of the requirements for the degree of Master of Science in Applied Earth Sciences

Thesis committee:	Dr. M.W.N. Buxton
	Dr. ir. A.C. Dieudonné
	Ir. M. Keersemaker
External committee:	Ir. D. Sandström
	M. Andersson
	Ir. A. Rijsenbrij
Project Duration:	March, 2025 - August, 2025
Faculty:	Faculty of Civil Engineering and Geosciences, Delft
Company:	Boliden Mineral AB

Cover:	Kankberg Mine, Sweden by Fotograf Jonas Westling AB
Style:	TU Delft Report Style, with modifications by Daan Zwaneveld (Modified)

Abstract

The depletion of shallow ore deposits is pushing the mining industry toward deeper underground operations, where efficient rock breakage remains a critical challenge. This thesis develops a mainly geotechnical, data-driven blast design framework for sublevel stoping in Boliden's Kankberg mine in northern Sweden. By combining established empirical methods with innovative computational approaches such as fuzzy logic, which handles uncertainty and variability much better and is ideal for subjective variables such as rock mass properties. This study enhances Lilly's Blastability Index and integrates Measurement While Drilling (MWD) data as a real-time proxy for in situ rock behaviour to complement and indirectly validate traditional blastability assessments. Site-specific geological and geotechnical data, together with laboratory tests, inform the development and calibration of this blasting framework. The results demonstrate the potential of the proposed Fuzzy Blastability Index (FBI) and the MWD rock factor to guide theoretical opening slot adjustments, with the intention of optimising slot raise design and reducing overall drilling costs. The methodology proposes a robust feedback loop between design and operations, contributing to a more scientific approach to underground drilling and blasting. Ultimately, this research offers a transferable approach for a next-generation blast design support tool in underground stope blasting. Although large-scale field validation is still required, the framework establishes a foundation for smarter, real-time design practices for the Kankberg mine.

Contents

List of Figures

List of Tables

Glossary

Blastability	The susceptibility of a rock mass to fragmentation by blasting..
Blastability Index (BI)	An empirical index to quantify blastability, developed by Lilly (1986)..
Blasthole	A drilled hole filled with explosives..
Booster	An explosive booster is a sensitive explosive charge that acts as a bridge between a (relatively weak) conventional detonator and a low-sensitivity (but typically high-energy) explosive..
Burden	The shortest distance between a blasthole and a free face or adjacent distance between rows of blastholes that are orthogonal to the free face; a critical factor in blast design..
Crushed Zone	The zone around a blasthole where the rock is pulverized by intense detonation pressure..
Defuzzification	The process of converting fuzzy output into a crisp, single value in fuzzy logic systems..
Density Influence Index (RDI)	A parameter in Lilly's BI accounting for the rock density..
Discontinuity	A fracture or weakness in the rock mass such as a joint, fault, or fissure..
Drill and Blast (D&B)	A rock excavation method using drilling and explosives, common in mining..
Free Face	An exposed rock surface towards which the explosive charge can break out..
Fuzzy Blastability Index (FBI)	An enhanced version of the Blastability Index that uses fuzzy logic for improved precision..
Fuzzy Inference System (FIS)	A framework that uses fuzzy logic rules to produce outputs from imprecise inputs..
Fuzzy Logic	A system of mathematical reasoning that allows for partial membership in categories, handling uncertainty better..
Joint Plane Orientation (JPO)	The angle between rock joints and the free face; a parameter in Lilly's BI..
Joint Plane Spacing (JPS)	The average distance between joints; a parameter in Lilly's BI..
Measure While Drilling (MWD)	Real-time data collection system during drilling operations, capturing parameters like penetration rate and pressure..
Membership Function (MF)	A mathematical formulation that assigns a membership value (often between 0 and 1) to each element in an input space, indicating the degree to which that element belongs to a fuzzy set..
Overbreak	Rock broken outside the planned excavation boundaries..

Penetration Rate	The speed at which a drill bit advances into rock, used to infer strength and structure..
Powder Factor	A ratio that expresses the amount of explosive used in a blast to the amount of rock to be broken..
Raise/Winze	A vertical or inclined underground excavation used for access, ventilation, or blasting..
Reamer hole	An unloaded blast hole that has been reamed (widened) to serve as a free face..
Rock Factor	An index derived from MWD data, combining strength and structural indicators of the rock mass..
Rock Mass Description (RMD)	A qualitative classification of rock mass condition; a parameter in Lilly's BI..
Rock Quality Designation (RQD)	A measure of rock mass integrity based on the percentage of intact core pieces..
Spalling	Breakage of rock slabs parallel to the free face due to tensile wave reflection..
Stope	Large underground cavity excavated for ore extraction..
Strength Factor	A component of the Rock Factor indicating rock resistance, based on MWD torque and pressure data..
Structural Factor	A component of the Rock Factor representing the degree of fracturing in the rock, based on MWD signal variation..
Sublevel Stoping	A mining method involving large-scale blasting between sublevels to extract ore efficiently..
Unconfined Compressive Strength (UCS)	The maximum uniaxial stress a rock can withstand before failing; a proxy for hardness..
Underbreak	Incomplete rock breakage within the planned excavation area..
Virgin Stress	The stress state of a rock mass before any human-induced disturbance, such as excavation..

1 Introduction

The continuous depletion of easily accessible shallow ore deposits has resulted in a significant shift from opencast to underground (UG) mining methods. To keep up with the increasing demand for raw materials worldwide, the mining industry must maintain target production. Traditionally, open-pit mining favours high production rates. Large-scale blasting is therefore an efficient method for UG operations to perpetuate. Scientists, engineers, and practitioners alike have been busy dealing with the challenges that come with the increasing scale of UG mining. Statistical, empirical and numerical methods continue to advance to better predict the response of rock masses and allow efficient and fast-paced production (Kumar Himanshu et al., 2023).

1.1. Kankberg Mine

The Kankberg UG gold-tellurium mine, located in northern Sweden and owned and operated by Boliden Mineral AB, has recently switched to a more productive and larger-scale mining method. The mine has started developing sublevel stopes at depths between -550 m and -650 m. However, the extremely hard and brittle rock conditions prove challenging for drilling and blasting (D&B). For example, the rock conditions result in low drilling rates, which are a costly undertaking due to the frequent need for drill bit changes and extensive man-hours. Poor fragmentation, in turn, results in losses throughout the entire mine-to-mill production chain.

The current D&B design procedure assumes homogeneity within the rock mass, which is hypothesised to be at least partially responsible for the poor blast performance currently observed. The D&B design of the slot raise (winze) in particular has proven problematic. The lack of a free face for the accumulation of broken rock makes it the hardest blast within every stope. These raises are the initial connection between production levels and are therefore crucial to commence production blasting within the stopes. In large-scale operations, raises are developed using raise borer machines (RBM). However, the scale of operations at Kankberg did not yet justify the high capital cost of such equipment. So, D&B remains the preferred method for the development of the slot raise. The problems are believed to be partially due to the lack of site-specific adaptation and the absence of proper post-blast reconciliation.

Research tells us that, to reduce these problems, precise D&B design is essential (Z. Zhou et al., 2024). In addition, to arrive at the right design, understanding the response of the rock mass to blasting is fundamental. Geological blasting related indices are key to modern underground blasting improvements (Sellers & Jackson, 2018). Blastability indices combine multiple influencing variables, making assessment of the failure response semi-quantitative. Thorough blastability evaluation is crucial for proper blast design (Latham et al., 2006). Classifying the Kankberg stopes in terms of blastability will support production by enabling engineers to make informed decisions and allocate resources more effectively, distinguishing between harder and easier blast areas. This will allow for a more efficient use of resources. Given the geological complexity and the current lack of feedback mechanisms in Kankberg its D&B process, this site provides an ideal setting for developing and applying a methodology that links rock properties with blast design.

1.2. Research Goal

The purpose of this research is to develop a rock parameter-based blast design tool to enable more efficient and responsive D&B operations in the Kankberg sublevel stopes. By integrating geology and geotechnical parameters obtained from existing site data and laboratory tests in the TU Delft Rock Mechanics Laboratory, the work uses and calibrates an empirical blastability index (BI), enhances it using the introduction of fuzzy logic (FBI), and explores the application of measurement while drilling (MWD) data in a similar system. The thesis is conceptualised from the inexistence of post-blast information, but offers site engineers practical tools for potential usage. The blastability and results of the MWD model are utilised to guide theoretical pattern and charging adjustments aimed at reducing excess drill meterage and better fragmentation under favourable blast conditions. Finally, the research offers a theoretical reconciliation framework to improve post-blast evaluation and to allow solid feedback mechanism development. The

structure outlined in this thesis is intended to support Kankberg-specific data-driven decision making and constitutes a first step toward next-generation, cost-saved D&B operations in a complex stoping environment.

1.3. Research Questions

The thesis will focus on the integration of rock type and geotechnical properties into D&B design, and how site-specific design can benefit from this, based on grounded theorems and widely accepted techniques. To structure the research and guide it methodologically, the following research questions will be used:

- *How can site-specific data be used to classify stopes based on their expected blast performance to inform D&B design?*
- *To what extent does MWD data support the blastability index as a predictor of rock behaviour during blasting?*
- *How can theory, blastability index results and MWD data guide theoretical improvements in opening slot design?*

Together, these research questions synthesise the main research question of this thesis.

- *How can rock mass data be used for an actionable drill and blast methodology to improve operational efficiency in the sublevel stoping area of Kankberg?*

1.4. Originality and Contribution

Although blastability indices have been widely discussed in the literature, their practical application remains limited. This thesis contributes by implementing a blastability-informed approach in a site where constraints are clear: unconventional stope geometries, quartz-rich ultra-hard rock, and no clear established system for evaluating blast performance. Rather than developing a theoretical model from scratch, this work reuses existing theorems, site data, and supplements it with targeted laboratory tests to build a relevant blastability index. The index is then supplemented by MWD signals with the purpose of raising confidence in the models and subsequently linked to decision making to show its practical use. This is where the true originality lies. This thesis combines empirical indices, fuzzy logic, and real-time MWD data in an integrated blastability framework, which is a novel approach for UG operations with limited data, linking site-specific conditions with real-world drill and blast decisions in a way that is repeatable, low-cost, and tailored to operational needs. In doing so, it proposes a method for D&B optimisation in not only Kankberg, but also many similar UG operations.

1.5. Scope

The thesis will attempt to create a holistic framework that guides the reader from the fundamentals of rock breakage to a proposition for theoretical opening slot design within the stopes based on theory and data. The theory is intentionally more detailed than required for the immediate implementation of the blastability framework. This was done with the intent to inform the academic reader and practising engineers, who may benefit from a broader understanding of the blasting topic, beyond the index-driven approach later in the thesis. However, the thesis will not cover all the intricacies that concern the difficult and specialist field of D&B. Topics that are out of the scope are found below.

- Large-scale field testing or operational validation of the proposed designs
- Explosives engineering, selection and the physics behind it
- Drill bit wear and rig performance
- Cost analysis

1.6. Thesis Structure

Overall, the structure of this thesis more or less follows how the work developed in practice. It starts by laying out the theory needed to ground the research in something scientifically rigorous, from the fundamentals of rock breakage to how blastability works, why an index is useful, and how fuzzy logic and MWD data can be applied. After that, the focus shifts to the study area; The Kankberg stopes themselves. Providing a detailed look at the geological setting, the mining method, and current drill and blast practices for context. The methodology chapter then explains how site and laboratory data were used, how the empirical blastability index was built and improved with fuzzy logic, and how MWD data were used to add to this framework. The results chapter shows what came out of the data processing, how sensitive the models are to different inputs, and how they compare with MWD trends. Based on that, the design implications are explored, including some theoretical adjustments and worked examples for a stope. These design ideas are not tested yet, but are based on what theory and site conditions suggest is realistic. The final chapters tie everything together with a discussion of the main limitations, assumptions, and data gaps, and the conclusion sums up the key takeaways and recommendations for how this framework could move towards a real feedback-based design process in future work.

2
Theoretical Background

This chapter provides all the theoretical foundation for the methods and models that will be encountered later in the thesis, and slightly more. To improve D&B design in the Kankberg mine, a thorough understanding of the physical mechanisms at play, their influence on blastability, and the tools available to quantify them are needed. Together, these concepts will ground the data-driven classification methodology and support the D&B strategies proposed later on. The reader should take note that D&B is incredibly complex. Despite the attempt to provide a detailed overview of mainly the geotechnical aspects of D&B design, one could write similar chapters on explosives theory, mine-logistics, or economics.

2.1. Mechanisms of Rock Breakage

Understanding how rocks respond to the release of energy during blasting is fundamental to optimising D&B design. Although the energy released in a typical blast is immense, only a small fraction (20–40%) is actually used to break the adjacent rock mass (Ouchterlony et al., 2004). The rest is lost in the form of heat, ground vibrations, air overpressure, etc. This low energy efficiency stresses the importance of understanding the complex breakage mechanisms in order to maximise energy use and minimise losses. Proper D&B design starts with intense collaboration between the D&B engineer and the geotechnical engineer, since understanding how the rock behaves lies at the root of the design (Thin, 2019).

2.1.1. Characteristics of Rocks

When dealing with rock break mechanisms, it is vital to recognise the fundamental characteristics of rocks that can directly influence how they fracture. Rocks are typically made up of a combination of minerals, each of which has different physical and mechanical properties. For this reason, rocks are inherently heterogeneous. In other words, they behave unevenly and uniquely when stressed as a result of varying grain size, mineral arrangement, and grain-force interaction. The boundaries between these grains can vary from strongly bonded to weakly bonded and filled with secondary fillings such as clay or air pockets. These boundaries have a major impact on the overall strength of the rock (Dessureault, 2004). Even more important are discontinuities, which include cracks, joints, faults, fissures, and bedding planes, all existing on different scales and orientations. These features can be the dominant control variable, as joints and faults can steer cracks or prevent them from spreading (Zhang, 2016). One of the main contributors of rock breakage are the (nearly) invisible microcracks formed by stress imposed on the rock, such as tectonic or temperature stresses. The goal in a blast is to extend these microcracks so that they link and result in fine fragmentation. These microcracks will connect much easier when a rock is experiencing tensile loading. On average, rocks are 5 to 10 times weaker in tension than compression, so in blasting most rock is broken during tensile loading (Persson et al., 1994). Porosity, which can be defined as small cavities in the rock, reduces its crushing strength, allowing for easier breakage. Rocks containing a lot of quartz tend to be harder and more abrasive. This also impacts production, for example, by making tool wear much more prominent (SECOROC, 2004).

The nature of most rocks is brittle. Under stressed conditions, fracturing is more likely than other forms of deformation. However, at greater depths, where rocks are subjected to higher pressures and temperatures, their behaviour becomes more ductile, as illustrated by the textures of many metamorphic rocks (Dessureault, 2004). In addition, the rate of loading has a significant effect on the way rocks break. Dynamic rock strengths tend to be greater than under quasi-static loading conditions, as rapid loading increases not only compressive and tensile strength but also fracture toughness. This is caused by crack branching, higher energy absorption, and greater kinetic energy in the fragments, all of which become more pronounced at higher loading rates. As stated in the introduction of this chapter, only a portion of the input energy is used directly for fracturing, much of it is lost to friction, wave reflections, and other forms of energy. Consequently, energy efficiency decreases with increasing load rate, suggesting that slower loading can be more effective from an energy utilisation perspective (Zhang, 2016).

2.1.2. Waves

Wave theory is another foundational basis for an engineer to improve the safety, quality, and efficiency of D&B. Solids deal with two types of stress waves: body- and surface-waves. In blasting, the main concern lies with body waves, since these are the only ones that actually travel through solid rock. Body waves can be divided into P-waves (compressional) and S-waves (shear), and their velocities can be calculated using the density and elastic moduli of the rock mass as demonstrated by equations 2.1 and 2.2.

$$C_p = \sqrt{\frac{E(1-\nu)}{\rho(1+\nu)(1-2\nu)}} \tag{2.1}$$

$$C_s = \sqrt{\frac{E}{2\rho(1+\nu)}} \tag{2.2}$$

Here, C_p and C_s are the velocities of the P- and S-wave [m/s], E is the Young's modulus (level of stiffness), ν is the Poisson's ratio (level of deformation perpendicular to loading), and ρ is the density of the solid. A key attribute of S-waves is that they cannot travel through fluids. This is crucial when dealing with fractured or saturated rock. Discontinuities, especially if they are orthogonal to the wave direction, tend to absorb or scatter a large portion of the energy of the S-wave over a distance (Zhang, 2016). In blasting, it is important to consider the interaction between different P- and S-waves. When two stress waves of the same type meet, their displacements and stresses transmitted to the rock will either beneficially superposition and sum or, if out of phase, destructively interfere and cancel each other. P-S wave interactions work differently because they act in different directions. Here, no reinforcing or cancelling occurs, but they co-exist and their stress can be derived from the vector sum. P- and S-waves are linear elastic waves, which means that they travel through the rock without permanently altering the structure of the material, provided that the stresses remain below the yield point. However, if the stress exceeds the elastic limit, the rock deforms plastically, giving rise to plastic waves. At even higher stress levels, such as those near the detonation front, shock waves form. Unlike P- and S-waves, shock waves are non-linear, can involve plastic deformation, and do not travel at constant velocity dictated by the medium. Their speed depends on pressure and particle velocity, as described by the Rankine-Hugenoit equations (Anderson, 2003).

When a wave hits an interface-boundary in the rock, part of it is reflected, and part is refracted. The incoming wave will split into new P- and S-waves, depending on the interface geometry and impedance of the two media. Impedance is defined as the product of the density of a medium (ρ) and the velocity of acoustic waves passing through it (c). When a stress wave passes from one medium to another, the ratio of their impedance is given by:

$$\mu = \frac{\rho_a c_a}{\rho_b c_b} \tag{2.3}$$

If $\mu = 1$, no reflection occurs. When $\mu > 1$, the reflected wave typically manifests as an S-wave, while if $\mu < 1$, it tends to reflect as a P-wave (Persson et al., 1994).

Attenuation describes the drop in wave amplitude over distance. It is mainly caused by geometry, internal friction, material damage, and the many small-scale discontinuities in the rock mass. Dispersion refers to how the wave pulse stretches as it travels. This is mainly due to differences in wave velocities (such as between P and S), internal friction, and wave interactions at interfaces. Since natural rock is full of irregularities and complexity, attenuation tends to be quite significant in practice (Zhang, 2016).

2.1.3. Breakage by Blasting

Fracture Mechanics

Fracture mechanics provides the basis for understanding how rocks fail during blasting. It relies on the assumption that the microcracks concentrate the stresses in the crack tips. When stress at a crack tip exceeds the crack toughness of the material, the crack will spread. Based on linear elastic fracture mechanics, the stress will theoretically be infinite at the tip of the crack and will dissipate quickly in an inverted square root fashion (Persson et al., 1994). Crack propagation occurs primarily in the three basic modes: Mode I (opening), Mode II (sliding), and Mode III (tearing). Most rocks break in Mode I, due to their tensile weakness, as stated in Section 2.1.1. Blasting takes advantage of this by generating high strain rates that push cracks past their strength limits, causing them to grow and link up.

Breakage Mechanisms

Where fracture mechanics explains the initiation and growth of cracks, the actual fragmentation process involves several distinct, yet overlapping, phenomena (Figure 1). The first response to detonation is the formation of a crushed zone directly around the blasthole, where the stress transmitted by the shock wave exceeds the compressive strength

of the rock and pulverises the material. Beyond this zone, one reaches the fracture zone. Here, radial cracking occurs because the shock wave induces tensile stress in the tangential planes, leading to fractures radiating outward from the blasthole. These are usually followed by tangential cracks, due to the build-up of tensile stress perpendicular to the radial cracks. Together, these two define the primary geometry of the rock fragments. Beyond the fractured zone, the seismic zone can be found. In the seismic zone, no fracturing tends to occur.

Once the energy of the initial shock wave passes, the explosion gas rapidly expands into newly formed cracks. Due to extreme pressures, the gases force them wider and drive them deeper. This goes on until the pressure eventually drops, usually due to plug failure or full penetration up to the free face. Additionally, pressure differences working on the rock near the gas-filled blasthole can induce a flexion-type breakage, similarly to a flexing beam anchored at one end. Spalling is another desired method of failure when blasting. When the P-wave generated by the explosive hits the free face and the reflected S-wave is stronger than the tensile strength threshold of the rock, they can initiate failure parallel to the free surface, causing thin layers or slabs of rock to detach. This process is most prominent in hard and brittle rocks and can significantly influence fragmentation near bench faces or tunnel walls. Thus, the charge is required to be close to the free face to minimise attenuation losses. Unlike radial or tangential cracking, spalling does not originate at the blasthole but rather at some distance away, where tensile reflection is maximised. Lastly, the final moment of fragmentation occurs once the rock is ejected and forcefully collides with neighbouring fragments. All of these types of breakage contribute to effective blasting and the resulting particle size distribution (Persson et al., 1994; Zhang, 2016).

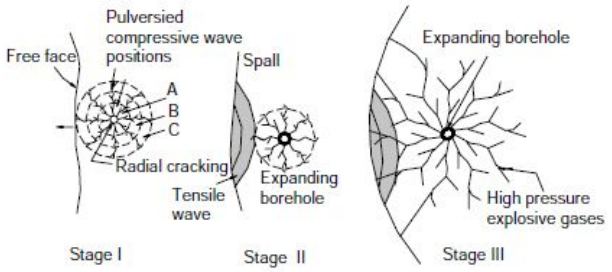

(a) Blasting stages of a charged hole, ABC represent different zones

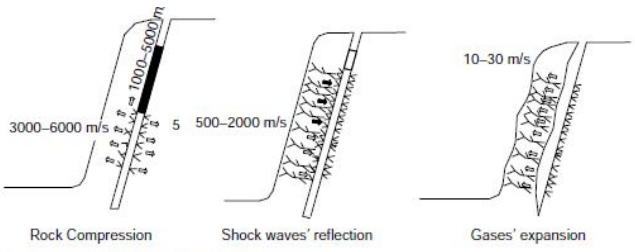

(b) Blasting stages of a charged hole, highlighting the relative speeds of different breakage phenomena

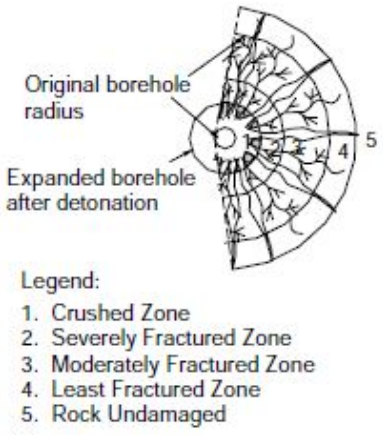

(c) Schematic of different blasthole zones

Figure 1: Schematic overview of a single blasthole fracture mechanisms (Online Mining Exam, 2015).

2.2. Blastability

With theoretical knowledge on how rocks tend to fragment, scholars started looking for ways to implement this in actionable metrics, including the blastability metric. The terminology of blastability refers to the susceptibility of the rock mass to blasting. Similarly to rock mass classifications (RMC), which have been primarily developed for geotechnical studies, blastability indices use similar input variables and sometimes RMCs itself. Blastability defines the expected response of the rock to a certain blast design (Dey & Sen, 2003), or to the rock mass within which it lies (Lilly, 1986). In recent decades, many have attempted, suggested, and developed new blastability indices. There have been several different approaches to estimating blastability. Some researchers have focused on linking it to laboratory and field data from rock property testing. Another common method is to estimate the blastability based on drilling

rates or observed blast performance in the field. The early versions follow mainly an empirical approach, while the newest versions tend to use computer-aided solutions, such as fuzzy models, due to their ability to interpret the qualitative values that are common with these index input variables (Azimi et al., 2010). Modern blasting design, with improved efficiency and safety, requires accurate blastability estimates of a rock mass. Although a universal methodology is believed to be possible (Dey & Sen, 2003), it has yet to be achieved (Z. Zhou et al., 2024). This section covers the selection of the right index for a job, commonly used indices, and highlights critical input parameters that influence blasting. Z. Zhou et al. (2024) provides a comprehensive review of blastability and its critical input parameters. Many of the key topics discussed in this section are explored in greater detail in their work.

2.2.1. Index Classes

The methodologies behind blastability indices are evolving rapidly and have undergone significant changes in their approach. Z. Zhou et al. (2024) classifies the blastability methodologies into four distinct categories as listed in Table 2. Apart from the single-index empirical class, which defines blastability using only one variable and clearly oversimplifies the blasting process, the other classes each have their own advantages and limitations. One should weigh fast and rough against slow and detailed based on the on-site specifics like data availability and production pace.

Table 2: Overview of Blastability Index Classes.

Class	Description	Evaluation Methods
Single Index Empirical	Uses a specific input variable to describe blastability. Straightforward and simple, but outdated.	BC (Hino, 1959); W_i' (Bond & Whitney, 1959)
Multiple Index Aggregation	Multiple input variables, aggregated by summing or multiplication. Reminiscent of geotechnical classification schemes, still in wide use today.	GBI (Ghose, 1988); BI (Lilly, 1992)
Comprehensive Evaluation	Structured, multi-input approach using weighted variables and synthesis methods to evaluate blastability	Fuzzy Sets (Azimi et al., 2010); Entropy/UMT (J. Zhou & Li, 2012; J. Zhou et al., 2022)
Machine Learning	Self-learning algorithms that reduce subjectivity but require large datasets, limiting current application	ANN (Han et al., 2000); RS-SVM (Jiang et al., 2017)

2.2.2. Index Selection

Using the right index for a specific blasting problem is a must. Some indices are specifically designed and tested for open pit blasting, and some for UG operations (Dey & Sen, 2003). One should also consider which parameters are readily available in order to minimise assumptions and reduce the risk of misclassifications due to data inaccuracies. Z. Zhou et al. (2024) studied 42 different blastability indices and the frequency of their respective input parameters (Figure 2). One can observe a great dependence on the rock properties and to a lesser extent the external factors or blasting parameters. Problems may arise if the selected variables are too strongly correlated, which is often the case with rock properties. Using such parameters can lead to redundancy and an unnecessary long computation time (Latham & Lu, 1999). Potentially, the most important criterion for the selection of the right index is its ease of use. Since it is generally applied in a high-pace production environment, it is unpractical to dedicate excessive resources and time to the acquisition of hard-to-obtain variables. Once selected, one should always consider how well developed and robust a blastability index is. The robustness of an index is typically dependent on the level of testing, in various case studies, with different geologies (Latham & Lu, 1999).

2.2.3. Variables Affecting Blasting

The complexity of rock breakage is mainly due to the large number of factors that influence the process. Organising all these influencing variables Z. Zhou et al. (2024) has divided them into four distinct classes. Characteristic parameters, structural parameters, blasting parameters and external factors (Figure 2). Much research has been conducted since the 1950s to describe the relevance of these individual variables. Characteristic parameters, such as UCS, density and seismic velocity, often form the backbone of blastability indices due to their availability from relatively straightforward tests and their importance to rock breakage as outlined in Section 2.1. Structural parameters, including joint spacing and fracture frequency, are powerful but more variable in quality and harder to quantify reliably. Blasting parameters, such as the powder factor, and external conditions, such as virgin stresses, undoubtedly influence the results, but tend to act as modifying factors rather than primary drivers. In other words, theoretically all parameters that describe

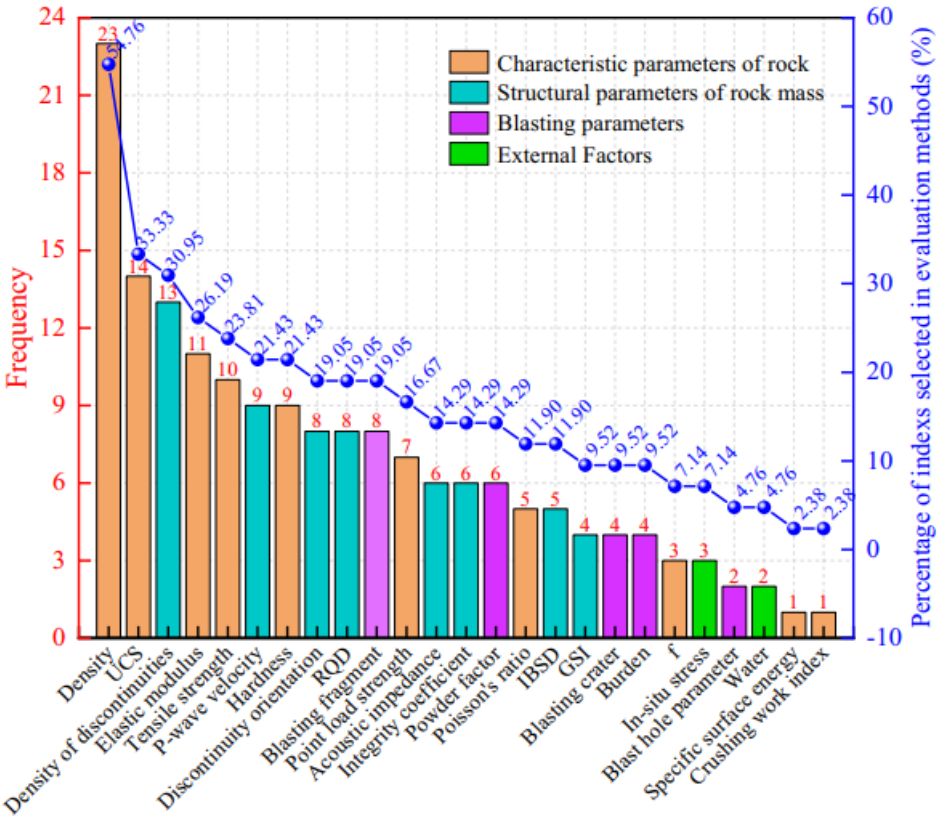

Figure 2: Frequency percentage of variables for 42 studied blastability indices (Z. Zhou et al., 2024).

a rock mass will have some influence on the rock mass's response to blasting. However, for practical engineering purposes Lilly (1986) describes that parameters with significant influence are few. That is, the structural nature of the rock mass, the spacing and orientation of the weakness planes, the specific gravity of the rock mass, and its hardness. Moreover, in practice, the selection of variables comes down to a balance between what is influential and what is available. For this reason, the variables used in this thesis are drawn not from theoretical completeness but from what can realistically be measured or inferred at Kankberg. This approach aims to limit assumptions, avoid parameter overlap, and keep the blastability assessment grounded and applicable.

2.2.4. Lilly's Blastability Index

The blastability index (BI) proposed by Lilly (1986) is among the most widely used and recognised empirical methods for evaluating the ease with which a rock mass can be fragmented by blasting, in both surface and underground applications. To this day, it remains one of the most cited and implemented indices in both academia and operational mine design. Many case studies and planning tools either incorporate or benchmark against Lilly's BI (Navarro et al., 2021; Segaetsho & Zvarivadza, 2019; Z. Zhou et al., 2024). Originally developed for surface mining applications, Lilly's BI has since been adapted and successfully applied in various underground mining contexts due to its simplicity and practical utility (Lilly, 1992). Lilly's method belongs to the multiple index aggregation class of blastability models, as described in Table 2. The key advantage of this model is its balance between complexity and usability, enabling meaningful blastability predictions without requiring excessive computational resources or hard-to-obtain inputs. Lilly's BI is closely related to the powder factor by a site-specific equation (Azimi et al., 2010). The BI is calculated as the average of five dimensionless rating factors, which correspond to the critical rock mass parameters that influence blast performance:

$$BI = 0.5 \cdot (RMD + JPS + JPO + RDI + H) \tag{2.4}$$

Where:

- *RMD* (Rock Mass Description): Describes the general condition of the rock mass.
- *JPS* (Joint Plane Spacing): Account for the overall size of the block.
- *JPO* (Joint Plane Orientation): Reflects structural complexity with respect to the free face.
- *RDI* (Density Influence Index): Represents the density of the material.
- *H* (Hardness): Indicates the compressive strength of the rock.

Each factor is assessed based on field observations or test results, using a standardised rating system. For example, rocks with widely spaced planar joints might receive a high JPS rating, while highly fractured zones would score lower. Similarly, UCS values are used to infer the hardness component (H), with harder rocks receiving higher BI ratings due to their resistance to blasting. The original BI value ranged between 20 and 100, due to the fact that the initial test locations (Australian open-pit iron mines) tended to vary between these values. However, the BI value ultimately depends on the input parameters, with lower values indicating more favourable conditions for blasting. The method proposed by Lilly has found popularity due to its straightforward interpretation, as shown in Table 3.

Table 3: Lilly's Blastability Interpretation (Lilly, 1992).

BI Value	Blastability Class	Description
High	Poor	Highly competent rock, difficult to blast
Medium	Moderate	Average blast performance expected
Low	Good	Easily fragmented, well-jointed rock

The original scoring ranges can be found in Table 4, these ranges function as weighting factors. From these weighting factors, it is clear that the BI is heavily dependent on the nature and orientation of pre-existing planes of weakness, described by RMD, JPS and JPO. However, the density and hardness of the rock mass play a relatively minor role. Table 4 includes the RQD scores; these are not original and were added by the author to describe the friable, blocky and competent rock masses.

Table 4: Original scoring ranges for Lilly's BI input parameters.

Parameter	Description / Classification	Score
RMD	RQD < 25% (friable)	10
	RQD 25% - 50% (blocky)	20
	RQD > 50% (competent)	50
JPS	Very close spacing < 0.1 m	10
	Moderate spacing 0.1–1.0 m	20
	Wide spacing > 1.0 m	50
JPO	Joints sub-horizontal / parallel to face	10
	Joints dipping out of face	20
	Joints striking normal to face	30
	Joints dipping into face	40
RDI	Calculated from density (ρ) as $RDI = 25 \cdot \rho - 50$	—
H	Calculated from UCS as $H = 0.05 \cdot UCS$	—

Although Lilly's BI was initially intended for surface operations, the conceptual framework remains applicable underground, particularly in development headings or stopes where rock fragmentation and muckability are key concerns (Alipour et al., 2018). However, due to differences in face dimensions, burden, and confinement, underground adaptations may involve recalibrating the input parameter weightings or using the BI as a qualitative indicator rather than a precise powder factor predictor. For the purposes of this thesis, the Lilly index serves as the empirical baseline method for the classification of blastability at the Kankberg site. It provides a fast and intuitive way to relate geological observations to expected blast performance, supporting both operational planning and comparative evaluation alongside more advanced computational models. Despite the widespread applications in practice, the BI tends to have deficiencies which can result in uncertainties in their usability. Sharp transitions between classification classes and subjective input parameters inevitably require a more nuanced approach.

Fuzzy Set Enhanced Blastability Index

Fuzzy set theory offers a solution to tackle the inherently problematic crisp transition between variables. This mathematical framework allows variables to have degrees of membership between 0 and 1, instead of a fully binary classification (Figure 3). This allows for a more nuanced approach to uncertainty and vagueness. Scholars such as Azimi et al. (2010) and Alipour et al. (2018) have evaluated the performance of the fuzzy set theorem on blastability indices and discovered that fuzzy models operated more consistently, with lower uncertainty and greater precision.

Fuzzy models are represented by Fuzzy Inference Systems (FIS), which have three main components: a rule base, a database, and an inference mechanism. The rule base is a set of if-then rules designed to mimic human expertise and

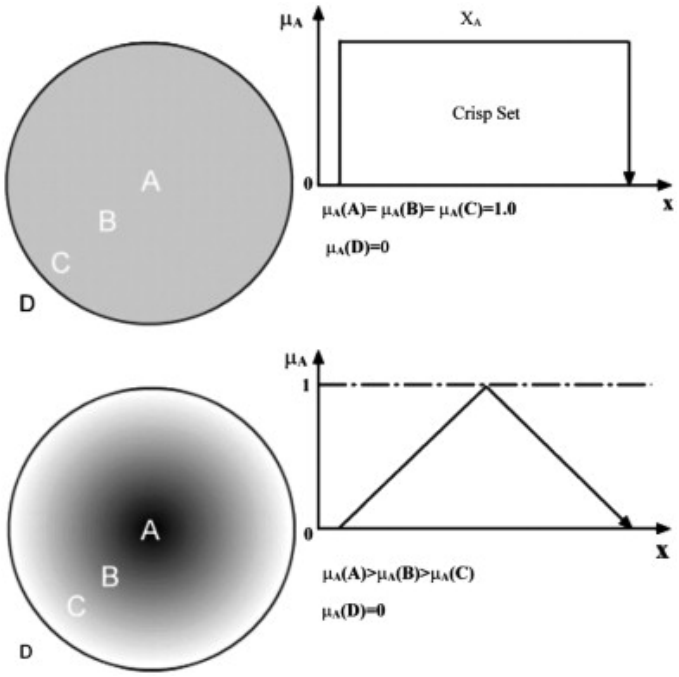

Figure 3: Fuzzy sets compared to crisp sets (Azimi et al., 2010).

judgment. If-then rules are commonly referred to as fuzzy rules. The database represents the shape of membership functions, which are functions that specify the degree to which inputs belong to a set. Inference mechanisms are the drivers that weigh the imposed fuzzy rules on the input data to deliver the output. In the blastability domain, the Mamdani FIS has found particular popularity due to its easy interpretability and visual transparency (Alipour et al., 2018), and will therefore be used in this thesis.

To construct a fuzzy BI model, each of Lilly's BI inputs will have to be translated into a fuzzy set with suitable membership functions. These membership functions typically follow triangular or trapezoidal formulations. For example, the parameter 'hardness' might have fuzzy sets labelled 'low', 'medium', and 'high', each with overlapping membership functions that allow smooth transitions between categories. These fuzzy inputs are processed through a rule base, where each rule might take a form such as:

IF X is high AND Y is low THEN Z is high.

The output of each rule is aggregated and subjected to a defuzzification step. Often using the Centroid of Area (COA) method, to define a crisp blastability value. This process mitigates abrupt changes between blastability classes that can arise from small variations in input parameters in traditional models. This will make the BI less sensitive to small changes coming from the qualitative database, making the index behave more consistently. An intuitive visualisation of the Mamdani FIS method is shown in Figure 4. The illustration here has two input variables and two rules. Illustrating both the handling of fuzzy and crisp input variables. The output variable is obtained by taking the geometric centre of the output distribution, in other words, COA is applied.

Unsurprisingly, fuzzy models also have pitfalls. The major issue with the methodology is the accurate definition of fuzzy rules. Models are highly dependent on the quality and coverage of fuzzy rules. Selecting defuzzification strategies also requires additional careful calibration. Despite clear challenges, the more flexible and context-sensitive fuzzy Mamdani model will be applied to the Kankberg site, offering a comparative analysis alongside Lilly's BI.

2.3. Measurement While Drilling as a Blastability Proxy

MWD is a feature that collects real-time information while drilling. This acquired data contains signals of many drilling variables, which include penetration rate, percussive pressure, feed pressure, rotational pressure, flush pressure, and damp pressure. These drilling parameters will respond dynamically to changes in rock mass (Isheysky et al., 2021; Van Eldert, 2019). However, in addition to these desired geological factors, there are more influences that can affect MWD signals, including operational factors, such as drilling settings, bit wear, and operator variability (Heydari et al., 2024; Isheysky et al., 2021). The likely interdependence of these variables can make the extraction

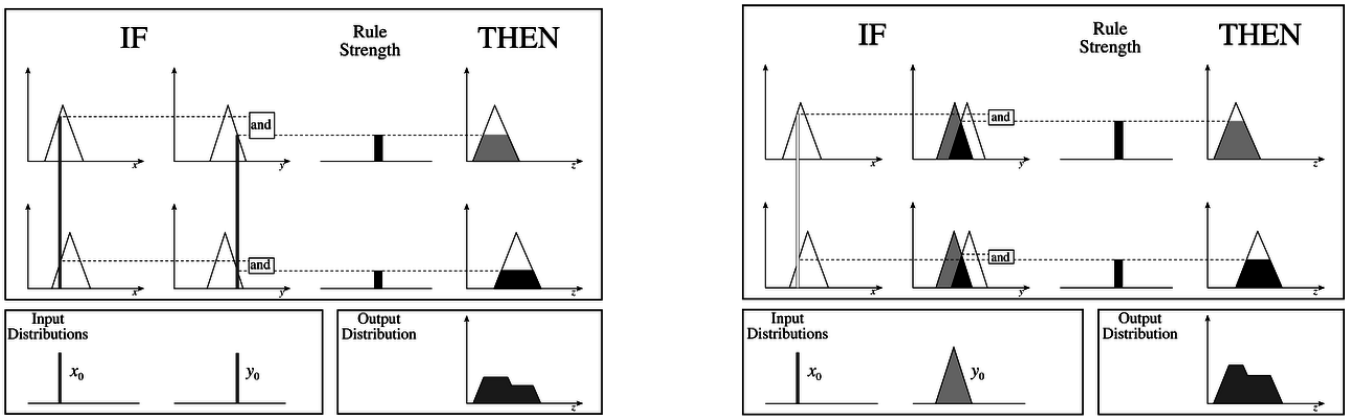

(a) Crisp input handling

(b) Fuzzy input handling

Figure 4: Mamdani FIS visualization (Knapp, 2004).

of reliable geotechnical insights rather difficult unless adequate filtering, outlier removal, and other processing techniques are applied beforehand. For example, variations in penetration rate could indicate changes in rock strength, but can also be altered by drilling system adjustments, idle rotation of the drill bit, or borehole deviation (Fernández et al., 2024). Studies indicated that in highly fractured rock formations, torque values could potentially increase due to drilling tool jamming, which may then result in misinterpreting the data as variations in rock hardness rather than an operational issue (Schunnesson, 1996). Despite these challenges, research has focused on the development of MWD-derived indices, such as the Hardness Index for drillability assessment, the Fracture Index for quantifying rock heterogeneity and the Water Index for detecting water-bearing structures based on flush pressure (Schunnesson, 1996; Van Eldert, 2019). However, the applicability of these indices remains site-specific, which requires on-site research and development of methods to interpret MWD data. At this moment in time, a complete standardisation of MWD data handling is still out of reach due to extreme complexity and uniqueness of the Earth's rocks. However, advances in computer-aided solutions could prove to be the initial step toward this goal (Fernández et al., 2024).

Nevertheless, MWD has been growing in popularity within the industry to acquire rock mass parameters, as can be seen by efforts to create MWD-based indices. The underlying assumption is that the interaction between the drill bit and the rock serves as an indirect indicator of the rock's strength, condition, and anomaly detection. Recent research by Navarro et al. (2021) showed the possibility of deriving a Rock Factor index from MWD data, which can be roughly interpreted as an index for blastability (Z. Zhou et al., 2024). Navarro et al. (2021) achieved this by deriving two key factors from the raw MWD data.

1. Structural factor: A proxy for the degree of fracturing, based on the variability of drilling signals.
2. Strength factor: A proxy for the rock's strength, based on required pressure and rotation assuming that strong rocks resist more.

Together, these two factors formed the rock factor. Since this factor is only built up by the MWD data, it can theoretically serve as a real-time in situ rock response validation tool for the BI. Even with MWD its setbacks that have been discussed earlier, it provides a method to check the derived BI's to real-time measurements. Of course, it may appear problematic to validate one derived quantity (BI) using another (MWD-based index), especially if neither can be independently validated in their current stage. Yet, this approach holds value if both show similar trends despite having different data sources. Their alignment could suggest internal consistency, increasing confidence in their reliability and usefulness for operational decision making.

2.4. Drill and Blast in Sublevel Stoping

2.4.1. Sublevel Stoping

Sublevel stoping is a medium to large scale UG mining method. The mining method knows both up- and down-sides. Key advantages include the high productivity of the method, relatively low exposure to unsafe conditions, and the possibility of simultaneous unit operation. Disadvantages include slow and complex development and safety risks accompanied by large-scale blasting, such as excessive ground vibrations (Harraz, 2014). Due to the opening of large stopes, it is crucial that both the ore and host rocks are competent in nature to allow stable excavations. Total ore recovery is possible if primary stopes are back-filled to allow excavation of the initial pillars. For this thesis, it is important to highlight the three critical development steps of this mining method, which will create an understanding

of the different types of blast that are necessary for general production and why slot development was particularly selected.

Step 1: Access Development
In order to get access to the planned stopes, one first needs to create the infrastructure to get there. This includes cutting drifts at different levels. In the simplest representation of the mining method, these levels will either be used to drill the blastholes from, or create a haulage level and drawpoint for the muckpile. Since the drifting methodology is not different from any other infrastructure development present in a mine, this development step will not be discussed further. Figure 6 gives a schematic overview of the general evolution of a sublevel stope. Depending on site-specific factors such as the geometry of the ore body and the geotechnical characteristics of the rock mass, the shape and size of a stope can vary significantly.

Step 2: Slot Development
Within stope development, creating the initial opening is generally considered the trickiest part. One needs to open a large enough slot raise to allow material movement in the subsequent production shots. It is a tedious process to connect the production levels effectively by drilling and blasting. The longer the slot raise, the more confined the rock will be and the harder it will be to remove the material, especially since adequate tools such as RBMs are not always available. Therefore, D&B remains the most common method, but as mentioned before, constrained conditions make it challenging to mitigate problems such as face jamming and boulder generation. Little literature is available on D&B design for slot raises, the few available specify the analogy with burn-cut face patterns (Figure 5) used in drift excavations (Kumar Himanshu et al., 2023). The only difference being the direction of material movement (Liu et al., 2018). The usual slot excavation involves reamer holes to create additional relief for the rock mass to move. An uncharged reamer hole requires a diameter larger than a charged blasthole (115–165 mm vs. 75–115 mm). These reamer holes facilitate breakage by facilitating tensile stress conditions within the rock mass. For charging and initiation of the blastholes, it is crucial to adjust the explosive density, as slot development requires stronger explosives in the central blastholes and weaker explosives in the cut holes along the outer rim to prevent unwanted overbreak. Therefore, emulsion or slurry explosives are preferred, especially site-mixed types, because of their flexibility to adjust the desired energy density. Initiation points must be strategically chosen; numerical studies have concluded that detonators should be placed between 20-30% of the blasthole length from the bottom plug. Enhanced breakage efficiency and uniform rock fragmentation can be achieved with this approach. Delay sequencing typically ranges from 100 to 500 ms between blastholes (Kumar Himanshu et al., 2023). An advanced and promising method is the incorporation of guided slot drilling, known as the Swedish slot method (Figure 5), developed and tested in LKAB's Malmberget mine. This method creates a linear slot of reamer holes that are physically interconnected. The first reamer hole is traditionally drilled, whereas consecutive holes utilise a guided hammer installed on a drill to maintain parallel alignment. A study comparing simulations of traditional drilling patterns with the guided slot drilling pattern concluded the superiority of the Swedish slot method, indicating improved fragmentation uniformity and reduced risk of drillhole deviation. Logically, even if the first reamer hole experiences deviation, the adjacent reamer holes will follow its path, stabilising the overall deviation. In contrast, it requires an accurate drilling of the initial reamer hole to prevent misalignment of the entire set. The analysis also suggested potential for optimisation, indicating a reduction in the drill meterage without compromising the quality of fragmentation (Kumar Himanshu et al., 2023).

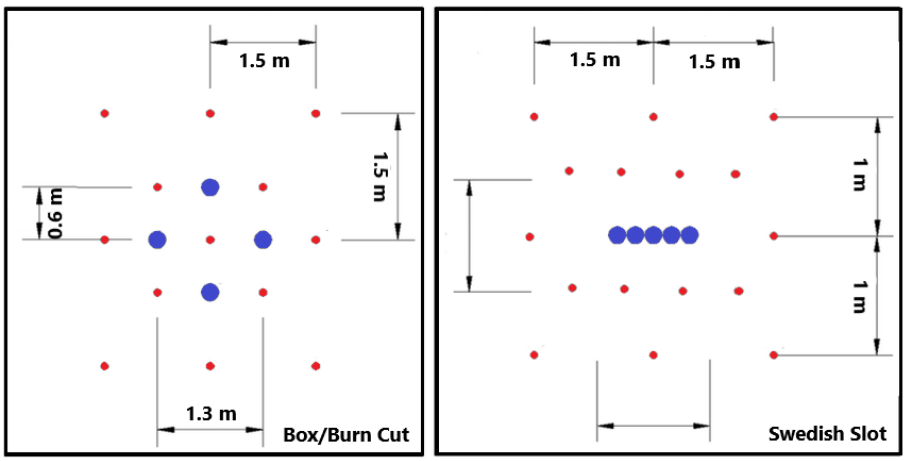

Figure 5: Schematic of discussed drill patterns, blue represents reamer holes, reds are blastholes.

Step 3: Production Blasting
For the production blasts of a stope, the most common method is ring blasting. Here, blastholes are drilled in a systematic fan-shape. Generally, this method allows for efficient extraction of large volumes when blasting toward a free face, which is created by the slot raise. Ring configuration designs converge toward the centre of the stope, optimising energy distribution by keeping the highest energy density in the central part of the volume. Optimal performance in these production blasts is dictated by careful selection of blasting parameters, such as the diameter, burden, spacing, and explosive charge distribution of the blastholes. These parameters require tailoring for the site-specific geotechnical conditions (Onederra & Chitombo, 2007). To manage the accuracy of drilling long holes, since drillhole deviations can significantly jeopardise blast operations (Persson et al., 1994), larger blastholes that are less susceptible to such inaccuracies are preferred. This comes with the disadvantage that larger blastholes can result in excessive ground vibrations and higher drill bit costs. Despite the efficiency of ring blasting, it presents challenges such as ground vibration control, suboptimal fragmentation, and ore dilution. To address these issues, modern blasting techniques employ methods like multi-deck firing, where charges within a single blasthole are separated by inert material to improve energy distribution. In addition, electronic delay detonators allow for precise control of timing sequences and explosive placement, further enhancing blast performance (Kumar Himanshu et al., 2023).

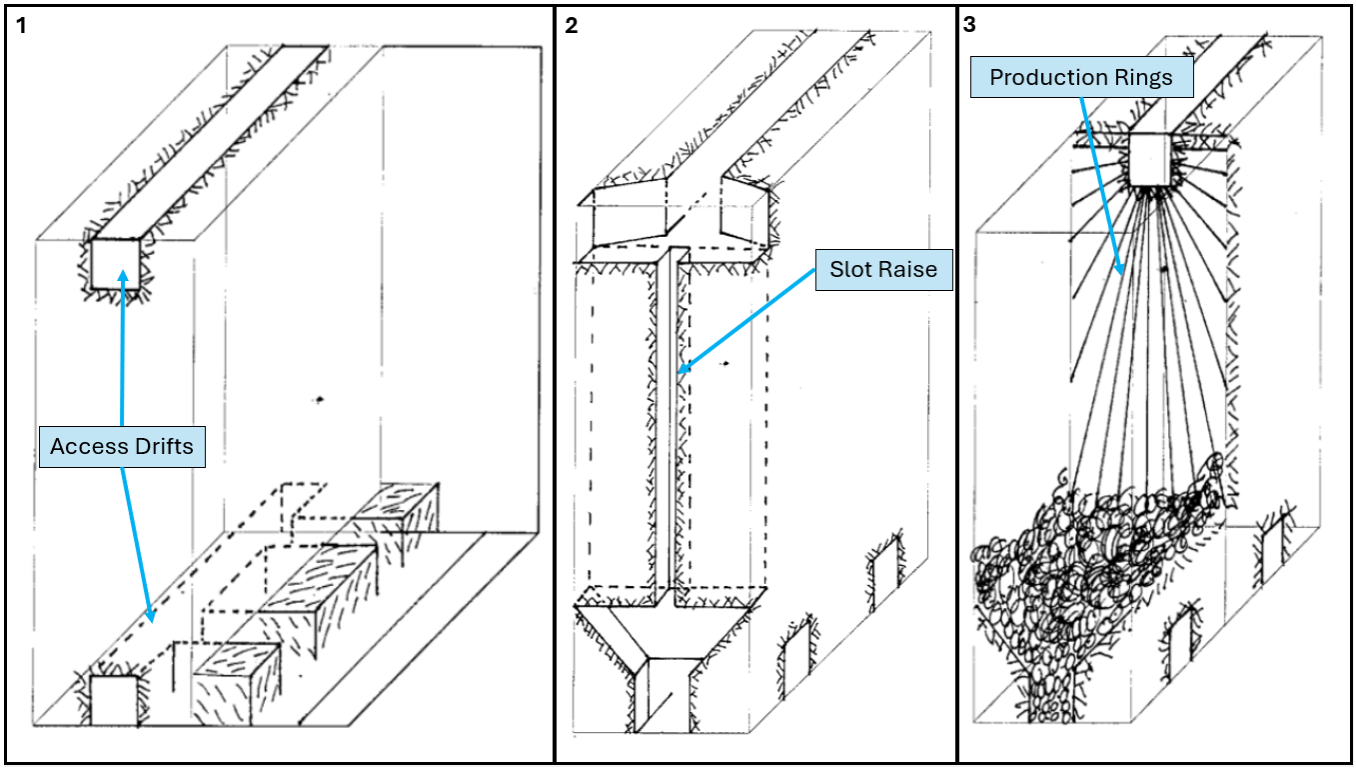

Figure 6: Sublevel Stoping Schematic: 1) Development of access to planned stope 2) Opening of stope initiated by slot raise 3) Production of stope by means of ring blasting (adjusted from Harraz (2014)).

2.4.2. Pattern Design in Practice

To understand how BIs can be applied effectively, it is important to first consider how pattern design is typically performed. As this thesis focusses primarily on the slot raise, the design of this feature will be the main focus of the section. As mentioned in the previous section, the slot raise is critical for a successful blasting campaign of a stope, since the quality of the slot its geometry dictates the effectiveness of the entire blast. The three necessary elements for the design are (Kay, 2002):

1. Availability of a free face; to enable tensile cracking
2. Sufficient void; to accommodate swelling
3. Adequate relief time; to prevent jamming

Void creation, in particular, is usually the first parameter considered to improve performance. It is represented by the void ratio, which can be defined in multiple ways, but the most commonly used is Lovitt and Collins (2013)'s definition:

$$V_r = \frac{A_r}{A_c - A_s} \tag{2.5}$$

where V_r is the void ratio, A_r is the area of the reamer holes, A_c is the cut area for the first blasthole and A_s is the blasthole area. Smaller voids also require longer relief times than larger voids to function effectively, increasing the need for proper timing. An example of the importance of the void ratio is illustrated in Tshabalala and Pretorius (2021). They increased their void ratio by increasing the size of their reamed holes from 152 to 204 mm without changing the slot pattern. This increased slot compliance from 56% to 73% in a year. Further support is illustrated in Chandrakar et al. (2021). They studied the influence of the void ratio on blast pull, which is the level of advancement achieved in a shot of (mainly horizontal) development headings through test blasts. It showed that a higher void ratio is strongly correlated with an improved advancement factor, that is, the percentage of pull with respect to the total length of the blastholes. Their experiments showed that void ratios as low as 20% could still yield over 90% pull. In contrast, in more confined headings, larger void ratios were crucial to achieve a higher level of pull. Confinement is defined by the confinement factor:

$$C_f = \frac{l}{w \cdot h} \tag{2.6}$$

where l is the depth of the drillhole, w is the width of the face and h is the height of the face. Furthermore, Chandrakar et al. (2021)'s study investigated how strata factors, specifically rock type, mineralisation, and Q-value, impacted performance. Observations showed that, on the basis of the strata, different void ratios were necessary for optimal blasting. Although their study derived a linear relationship for the void ratio and the confinement factor, it does not transfer to other rock mass conditions. This illustrates the inherent heterogeneity that makes a standardised approach difficult. A later study by the same author focused specifically on long-hole (single-shot) raising, which is the preferred method for vertical raising up to 40 m (Tatiya, 2005). Here Chandrakar et al. (2023) studied the void ratio again and successfully shot multiple 25 m raises in a single blast using a box cut pattern in four different UG mines. As in the development drive study, empirical linear models were derived. Here, linear relationships were found between the void ratio and the blasthole length as such (Chandrakar et al., 2023):

$$V_r = 3.582 + 1.091 \cdot l \quad \text{for } Q = 4\text{–}10 \tag{2.7}$$

$$V_r = 6.539 + 1.118 \cdot l \quad \text{for } Q = 10\text{–}40 \tag{2.8}$$

where one can observe that a higher void ratio is required for a better quality rock mass (higher Q). One should be wary that, while a higher Q indicates better structural quality, it does not necessarily imply better blastability. The study also found a relationship for the optimal delay timing, roughly 22 ms per metre of blasthole. This value was determined from the kinematic equation of the downward motion of the falling rock mass.

$$l = V_b \cdot t_{minimum} + \frac{1}{2} \cdot g \cdot t^2_{minimum} \tag{2.9}$$

where $t_{minimum}$ represents the minimum delay time between adjacent blastholes, g the gravitational acceleration, and V_b the range of burden velocity that can be obtained from various pieces of literature that estimate burden velocities based on blasthole diameter (Olsson et al., 2009; Wimmer et al., 2013; Zhang, 2016). Key takeaways from this critical study include the finding that low void ratios and short delay times are the primary drivers of failed raise excavations. Effective blasting was achieved using fully coupled charges, with double boosters for holes longer than 12 m, and a top and bottom stemming of about 2 m to retain energy. Lastly, precise drilling proved essential. Therefore, blasthole deviations should remain within 1–2% to avoid misfires and poor fragmentation. Otherwise, re-drilling is recommended.

More rules of thumb exist for slot design. Kumar Himanshu et al. (2023) found by means of numerical rock deformation simulations that the ratio between reamed holes and blastholes should be greater than one for optimal breakage and that both square and offset hole arrangements are effective for blasting. Furthermore, it was concluded that an offset hole arrangement results in better deformation control but lowered drilling productivity. Kumar Himanshu et al. (2023) mentions that delay sequences depend not only on the length of the blasthole, but also on rock conditions. For example, Indian conditions tend to favour 100 - 500 ms delay between holes, whereas in Sweden's Björkdal mine successful slot raises were blasted with inter-hole delay times of over 1 s.

These findings show that understanding the properties of the rock mass is vital for optimised blasting results. However, in practice, it is extremely common to use the same D&B designs continuously, irrespective of the rock mass and its properties, even between different mines. These decisions tend to be motivated by the high production rate that does not allow for detailed or experimental studies. However, substantial gains could be achieved by implementing rapid rock property assessment methods, such as a classification system tailored for blastability, and allowing for multiple D&B designs tailored to the distinct BI associated with different strata within a mine.

2.4.3. Reconciliation in Blasting Operations

Post-blast reconciliation is the only way to systematically optimise blasting outcomes. Although many mining operations around the world recognise the value of reconciliation and have implemented some level of assessment, these practices often remain basic or inconsistent (Thin, 2019). This section will explore the reconciliation approaches currently in place and discuss possible improvements that can enhance the accuracy, consistency, and, most importantly, utility of these assays.

Status Quo of Reconciliation Practices

The most widely used form of reconciliation is visual inspection of the degree of achieved fragmentation, with particular eye to degree of boulder formation. This is an immediate and intuitive indicator whether a blast performed as expected, but is inherently subjective and limits any quantifiable feedback loops in future design (Persson et al., 1994; Zhang, 2016). Another common and more advanced assaying method is LiDAR scanning. Here the focus is to map out over- and underbreak zones within the stope. Although quantifiable and valuable, it will not suffice for successful feedback loops on its own (McFadyen et al., 2020). There are many factors that can affect walls, such as rock mass, precision of drilling, misfires, or poor execution of charging crews. Therefore, operations that value reconciliation additionally measure drillhole deviations by means of blasthole probing. Vibration monitoring is also common. It is used to determine whether the shots fire as designed and whether the vibrations remain within safety limits to not harm the surrounding infrastructure (Persson et al., 1994).

The latter four techniques are currently in place at the Boliden Kankberg mine to some extent. However, other KPI's are also occasionally used as indirect proxies. For example, muck cycle times can be used as a proxy for fragmentation uniformity, assuming that finer and more consistent fragmentation enables faster mucking. Another indirect method is to assess crusher throughput or monitor mill performance. While insightful, these methods are dependent on the correct attribution of processed material to a specific stope. In practice, muck from multiple blast rounds or even different faces is often mixed during transport or in stockpiles, making attribution difficult. This challenge is worsened in multi-mine operations such as the Boliden area, where shared processing facilities introduce further ambiguity despite batch processing and separate processing lines within the mill. This is due to potential residual material in the processing lines from previous processing campaigns. These can blur the analysis and reduce the clarity of mill-derived reconciliation data.

Next-Generation Reconciliation

Recent advances in sensor technologies, data analytics, and machine learning offer more sophisticated methods and software that can provide greater accuracy and potentially more actionable insights. As mentioned in the previous section, there are many strategies that can be employed for reconciliation. However, to the author's knowledge, two methods have seen remarkable advancements in recent years, which will now be discussed.

Cavity Measurement Systems

Cavity measurement systems (CMS), which is the overarching term for scanning and measuring underground environments (including LiDAR-based systems), have rapidly increased in importance. Typical metrics used are Equivalent Linear Overbreak Slough (ELOS) and Equivalent Linear Lost Ore (ELLO).

$$ELOS = \frac{Volume_{overbreak}}{Area_{stopeface}} \tag{2.10}$$

$$ELLO = \frac{Volume_{underbreak}}{Area_{stopeface}} \tag{2.11}$$

These metrics allow for performance comparisons across stopes and convert complex shapes and volumes into simple, interpretable metrics. They are central to performance analysis in targeted blast design improvements. CMS over- and underbreak reconciliation is usually done across an entire stope, where higher resolution is achieved by looking at different faces within the stope. However, if the rock type varies greatly in a stope, it is unacceptable to compare the performance of the stope to geotechnical parameters using this method (McFadyen et al., 2020). Therefore, a recent octree-based stope reconciliation technique represents the next generation of performance analysis. The technique divides faces into octrees, submetre blocks, which significantly enhance resolution. This allows for a much better isolation of local geotechnical influences. In a study of 192 stopes conducted by McFadyen et al. (2020) using this technique, it was revealed that the hanging walls were the dominant source of overbreak, driven by low RQD, high effective radius factors (geometric proxy of local stress condition), and small blasthole stand-off distances (blasthole distance from the designed wall). However, the underbreak was mainly concentrated at floors and sidewalls, often in stope regions with poor blasthole coverage. Additionally, the study revealed that deeper stopes exhibited systematically greater overbreak, despite similar design parameters. This indicated depth-amplified stress responses. In general, the study highlighted that high-resolution analysis is worthwhile. For this reason, commercial products

such as the `mXrap` software platform offer these advanced diagnostics in a practical and scalable way for engineers to improve their reconciliation practices.

Fragmentation Analysis
Fragmentation modelling is a key part of blast design. The most widely used is the Kuz-Ram model, which is an empirical method that combines Kuznetsov's equation to estimate the mean fragment size with the Rosin-Rammler distribution to generate a full particle size distribution (PSD) curve (Cunningham, 1983, 2005). It is a crucial metric that enables performance analysis, where a narrow PSD around a desired mean value is sought. The method combines rock, explosive, and design parameters to predict the mean size of fragmentation. One of the inputs is, for example, the powder factor, which is closely correlated to Lilly's BI (Lilly, 1986). A key flaw in this promising method is the need for a thorough local calibration. In other words, an advanced system to measure actual fragmentation to close the feedback loop is vital. Dated 2D image analysis methods that use photography do not provide enough resolution, and many problems persist. These include suboptimal lighting conditions, accuracy in capturing complex shapes, and handling rock fragment overlap (Faramarzi.H & Esmaeili, 2025; Ikeda et al., 2023). Therefore, modern 3D techniques are combined with deep learning models. Ikeda et al. (2023) introduced a photogrammetry-based method that assesses PSD. They managed to achieve over 96% accuracy in predicting their fragmentation size. Faramarzi.H and Esmaeili (2025) used a LiDAR-based method that achieved 77% accuracy. Since PSD analysis provides a qualitative metric and is a direct indicator of pattern design, it is extremely valuable for blast reconciliation. So much, so that it has seen several highly advanced commercial implementations. For example, FRAGTrack^{TM} by Orica is a stereoscopic tool and deep learning model that allows real-time PSD analysis (Orica, 2023). High resolution cameras equipped on board of loaders and shovels allow for continuous monitoring and make detailed PSD measurement possible whilst accounting for the inherent sorting of fragmentation in the muckpile.

2.5. Theory Synthesis

The concepts and models discussed within this chapter constitute the overall theoretical foundation for the thesis's methodology and analysis. Among them is the realisation that performance in stope raises is governed by a multiscale interaction between rock mass properties, stress wave dynamics, and the geometry of the blast itself. The mechanics of rock breakage, and in particular the preference for tensile failure and the significance of wave behaviour, directly prescribe why certain variables are always emphasised in measuring blastability. They are not ambiguous measures, but formulations of the governing physics that control how and why rock fails under explosive loading.

The use of BI's, and Lilly's BI in particular, is a continuous effort to make such data useful for mining practice. Despite being empirical, Lilly's BI has a basis in the mechanics of breakage. Each of its parameters represents a measurable proxy for one or more of the significant physical behaviours described previously. However, empirical models are notorious for their limitations. The abrupt input classifications and the reliance on subjective judgment make them susceptible to input uncertainty and to not being able to describe the full spectrum of the inherent heterogeneous rock behaviour. Fuzzy set theory offers a natural step forward in translating this input into continuous functions more reflective to the vagueness and gradational character of geotechnical data. This improves not only the stability of outputs but also the robustness and interpretability of the index in practice.

Drilling data, such as that provided by MWD tools, introduce a dynamic component. Because it captures both the drill bit's interaction with rock in real time, MWD data can serve as an in situ, high-resolution marker of changing rock conditions. Although obviously plagued by a lot of operational noise and equipment inconsistency, it represents an opportunity to cross-validate the BI in an indicative manner and could raise confidence in local blastability predictions. Here, the connection to drilling is vital, because it closes the loop between theoretical expectation and observed response, and allows all theory to be refined with operational data.

Finally, placed in the context of opening slots in sublevel stoping, this theoretical framework provided a direction for improvement. As some literature suggests, problems encountered in slot raise design and stope production are not simply the result of poor execution, but are instead the result of a lack of correspondence between generalised design decisions and highly localised rock conditions. By making D&B decisions based upon the mechanics of breakage, supported by the use of quantitative indices and indicative verification with MWD data, it is possible to better design for rock conditions. Together, this will enable one to intentionally shift from a reactive approach to a proactive design stance, with theory serving as the guide and the performance metrics as the gauge.

3

Study Area – Kankberg Stopes

This chapter introduces the study area of this thesis: the Kankberg UG mine. It provides a general overview of the geology, the mine, with a particular focus on the stopes and available data.

3.1. Geological Setting

3.1.1. Regional

The Kankberg mine (64°55'20"N, 20°16'00"E) is located within the Fennoscandian Shield, a geologically ancient region that covers most of Scandinavia. It is primarily composed of Archean and Proterozoic crystalline rocks. The Fennoscandian shield can be subdivided into smaller regions, Sweden falling mostly under the Svecofennian domain, whose amalgamation dates back to about 2 - 1.8 Ga. This orogeny set the stage for most of the current-day mineralisation. Glaciation in the Quaternary eroded much of the sedimentary cover, exposing these ancient metamorphic and igneous rocks at the surface (Allen et al., 1996). Within the Svecofennian domain lies the Skellefte mining field, a magmatic province hosting over 85 pyritic massive sulphide deposits, gold vein deposits and porphyry deposits. The district is thought to be a remnant of a volcanic marine arc that accreted to the northern continental margin, the Arvidsjaur Group (Weihed, 2001). Many of these VMS deposits are spatially associated with felsic submarine volcanic domes, which acted as localised centres of mineralisation during periods of extensional volcanism (Allen et al., 1996). Over time, the district has experienced multiple deformation events that have greatly influenced the geometry and distribution of its deposits (Bauer et al., 2014). Bauer et al. (2014) states that the metamorphism has both overprinted initial hydrothermal alteration zones and reconcentrated metals of interest within current-day deposits.

3.1.2. Local

The Kankberg mine taps into the Åkulla deposit, which is a unique ore deposit in the Skellefte mining field. The ore body strikes 298°, dips 80°, and lies within an E–W principal stress regime (Rijsenbrij, 2024). Its key characteristic is the high levels of topaz-quartz alteration and the low levels of sulphur near the main ore concentration (Nordfeldt et al., 2019). Felsic volcanic rocks of dacitic to rhyolitic composition, occurring as quartz-feldspar porphyries, are the primary host of the ore body. Mafic dykes of post-genetic origin cut through the altered felsic host rocks and are associated with late-stage brittle deformation. The general trend of the ore body is vertical due to extensive deformation. Mineralised zones are found mainly within quartz-feldspar porphyry, volcaniclastics, and breccias. Epigenetic hydrothermal alteration has resulted in a highly competent and highly altered ore body (Voigt & Falshaw, 2024).

3.1.3. Stopes

In Figures 7 and 8 one can see the stopes intersecting geological units. The geology is complex, with a large variety of different units and structures. The andesite dykes are notable structures that cross the stopes at various locations as thin sheets. These dykes are also associated with high levels of alterations in the surrounding rock. Adjacent to the andesite dykes fuchsite sheets are commonly observed. Table 5 presents the volumes and percentage distribution of rock types within the stope limits. The primary rock types, shaded grey in Table 5, are porphyry, sericite quartzite, volcaniclastic, breccia, andalusite quartzite, and andesite. Together, they make up over 95% of the total volume. A small difference between stope volume and actual volume is observed because of either the presence of small amounts of other rock types not considered in the analysis or processing losses due to polyfaces not properly closing into solids. These six distinct rock types will be the focus for the remainder of this study.

The geologies depicted in Figure 8 show the geologies as recorded by the geological model. In Figure 7 only a selection that truly intersects with the stopes is visualised and the names are simplified, hence the difference. The model in question represents a simplified interpretation of the actual conditions of the subsurface. The geological block model

at Kankberg, constructed through interpolation of diamond drilling exploration logs, employs one of the smallest block sizes within Boliden (10m), reflecting the recognised complexity of the deposit's geology. Despite the aim of high-resolution modelling, the resulting model remains a smoothed approximation of reality.

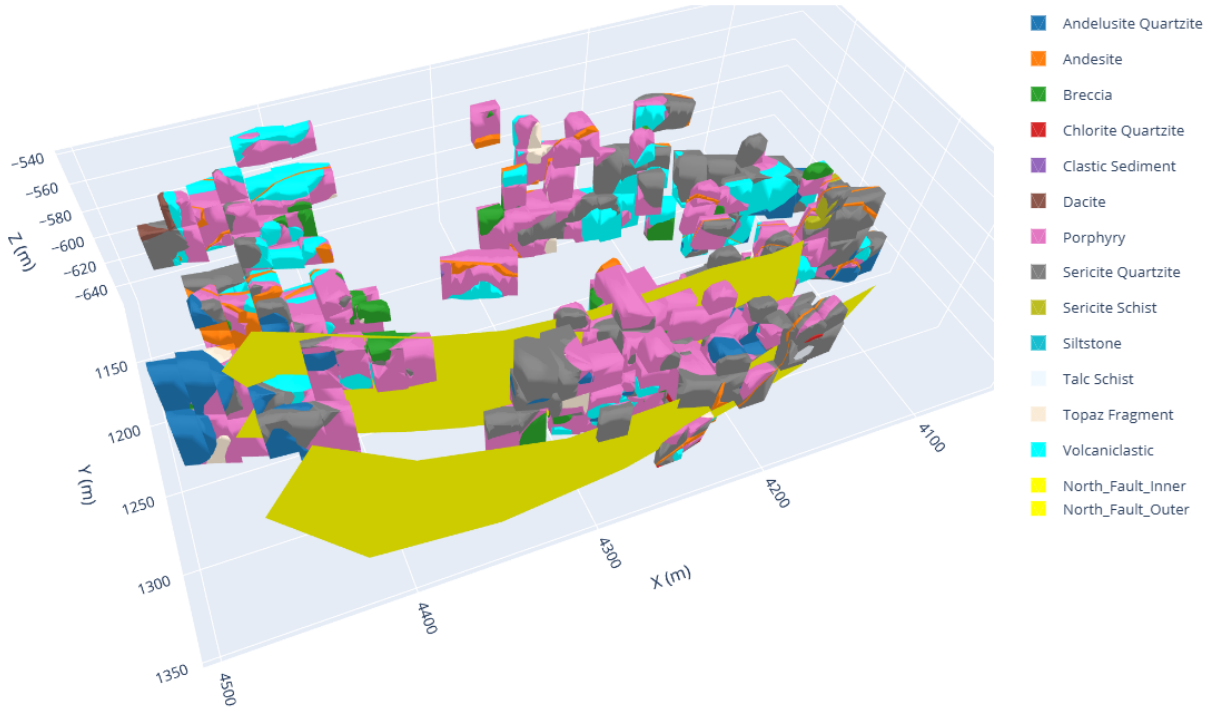

Figure 7: 3D visual of intersecting geologic units within the stope bounds.

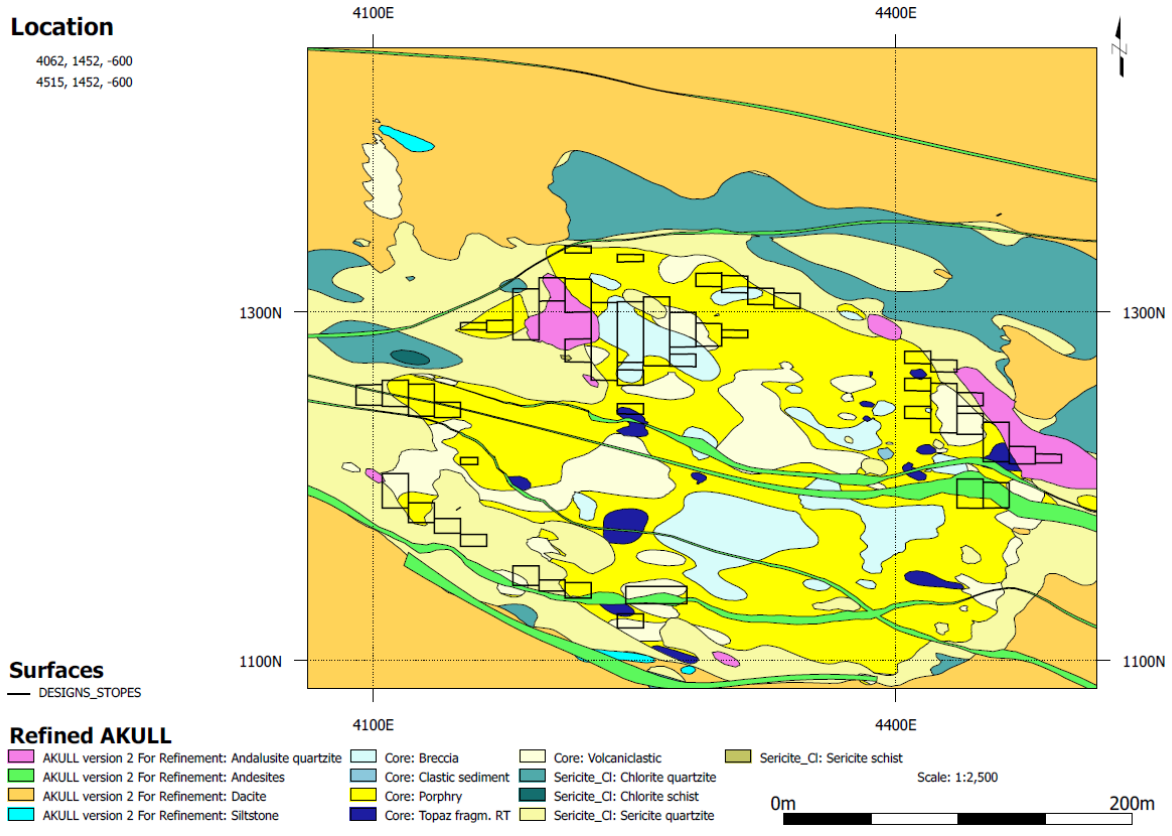

Figure 8: Plan view of stope geology (z=-600m).

Table 5: Volume and Percentage Distribution by Rock Type.

Rock Type	Volume [m^3]	Percentage
Designed Stopes	806259	100.00%
Porphyry	360263	44.68%
Sericite Quartzite	162986	20.22%
Volcaniclastic	113863	14.12%
Breccia	74534	9.24%
Andalusite Quartzite	49399	6.13%
Andesite	22321	2.77%
Topaz Fragment	17508	2.17%
Chlorite Quartzite	2115	0.26%
Sericite Schist	1556	0.19%
Talc Schist	782	0.10%
Dacite	654	0.08%
Clastic Sediment	243	0.03%
Siltstone	35	0.00%

Rock Types

The classification of rock types within Kankberg is done in an operational context and should not be confused with the more formal petrographic sense of the word. The classes are used in the mine for exploration, logging, and mining operations. A total of 57 rock types have been distinguished (Voigt & Falshaw, 2024), of which 14 occur in the stoping area. Within some of these rock types, a subdivision is additionally used on the basis of their levels of andalusite and topaz alteration. The following section briefly introduces these rock types. A more detailed description of these can be found in Jönsson et al. (1999) and Rijsenbrij (2024). No systematic study has previously been conducted on the blasting performance of these units. Therefore, some of the following descriptions are based on the observed rock characteristics and reasonable assumptions about their likely influence on fragmentation and stability. These interpretations are revisited in later chapters of this thesis.

Porphyry

(Quartz-Feldspar) Porphyry is the most common rock type in the stopes and is a fine to medium-grained, coherent unit. The rock is massive and generally homogeneous with minimal internal variation. It is commonly strongly silicified, but structural features, such as foliation, are poorly developed. Due to its homogeneity, porphyry is expected to fragment relatively consistently under blast loading. However, its stiffness may contribute to stored elastic energy, which could increase the potential for overbreak or localised bursting if the charge distribution is not well controlled.

Sericite Quartzite

Sericite quartzite is a fine-grained, altered rock with variable foliation. The structure ranges from massive to weakly schistose depending on the intensity of the alteration. This anisotropy may influence stress redistribution and cause uneven breakage during blasting. Despite the tendency of the rock to break up well, thin foliation planes or weak zones may result in undesired breakage, oversized fragmentation, or slabbing. In other words, the anisotropic nature of the rock will likely favour certain blast directions.

Volcaniclastic

Volcaniclastic rock is characterised as an inhomogeneous unit comprising various grain sizes and clastic textures. The class is used as an overcoupling term that comprises various subtypes that have not been individually classified. It is relatively common within the stope volume and is moderately to strongly altered locally. Inevitable internal variability can result in unpredictable blasting with mixed fragmentation and irregular break profiles as a consequence.

Breccia

Breccia is characterised by angular clasts in a finer matrix, often highly silicified. The rock is heterogeneous and spatially variable, with changes in clast size, orientation, and degree of cementation occurring over short distances. Its brittle nature may promote spontaneous fracturing, particularly near open faces or unsupported areas. Blasting in breccia may result in excessive overbreak and, in some cases, localised rock bursts due to its stiffness and potential for energy release.

Andalusite Quartzite
Andalusite quartzite is a fine- to medium-grained, dense rock that often contains visible aluminium silicate minerals. The rock mass is usually massive and homogeneous with low deformability. High strength and hardness reduce drillability and may hinder fragmentation efficiency. Occasional joint fills, such as muscovite or talc, may locally reduce stability and add anisotropy to the rock mass, both of which can contribute to poor blasting.

Andesite
Andesite occurs as a fine-grained, visibly darker rock and intersects the other rock as dykes. These dykes are generally thin sheets less than a metre in width. It has moderate strength, but it may show local variability depending on the intensity of the alteration. In more altered areas, the presence of chlorite or fuchsite can reduce joint friction. From a blasting perspective, andesite may behave consistently. However, the key concern are their sheet like structures that create large interface boundaries within the extent of the stope. These large boundaries may introduce unwanted energy losses that make blasting behaviour less predictable.

3.2. Rock Mass Data

Concerning the stopes of Kankberg, large amounts of data are available. All of these data sets can be viewed and altered in various software, including Deswik and Leapfrog. However, Python enables free, user-friendly and efficient data processing, visualisation, and infinite analysis possibilities and is therefore the primary used software.

3.2.1. Geotechnical Properties

In total, 165 cores have been geotechnically logged, of which 141 intersect fully or partially with the stoping area (Figure 9). Data currently recorded during logging are rock type, core discing, joint spacing, degree of joint roughness, joint fill, and BRQD (Section 4.1.1). Data availability can vary significantly per core sample, some samples include extensive logging whereas others only have one logged parameter. Because the equipment does not allow for orientation readings, no data is available on the joint orientation. In Figure 9, it can be seen that the available core data is limited to a specific region within the stoping area. However, this region corresponds to the first area scheduled for development according to the mine plan. Furthermore, a point-load test (PLT) has previously been performed to analyse the strength of some rock types that are present within the stopes. The 76 PLT tested samples have a mean distance of 76 m to the nearest stope, with a maximum of 228 m. The compressive strength values range from 64 MPa to 751 MPa for the different types of rock, and no trend of increasing strength over depth is observed. The reliability of the PLT has been questioned, especially for very soft or hard rocks where tip penetration/deformation of the loading head can falsify readings (Akbay & Altindağ, 2020).

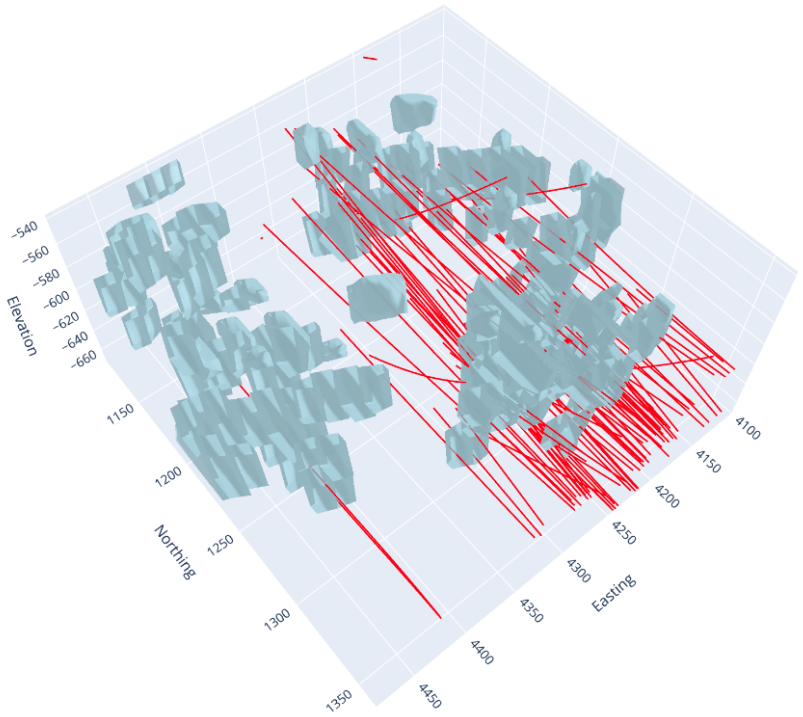

Figure 9: Visual of the geotechnically logged diamond drillholes in the stoping area.

3.2.2. Face Mapping

In addition to drill core data and the geological model, face mapping exists for the access drifts of the stopes. Such observations provide direct outcrop exposure to lithological contacts, vein intensity, and structure at the free face. They are a useful marker against which to compare the modelled geology and can help to catch local variations such as unmodelled units and anomalous alteration patterns. Figure 10 shows an example of one of the face maps taken into account in this study, the transparent section shows the outline of the mined out stope solid.

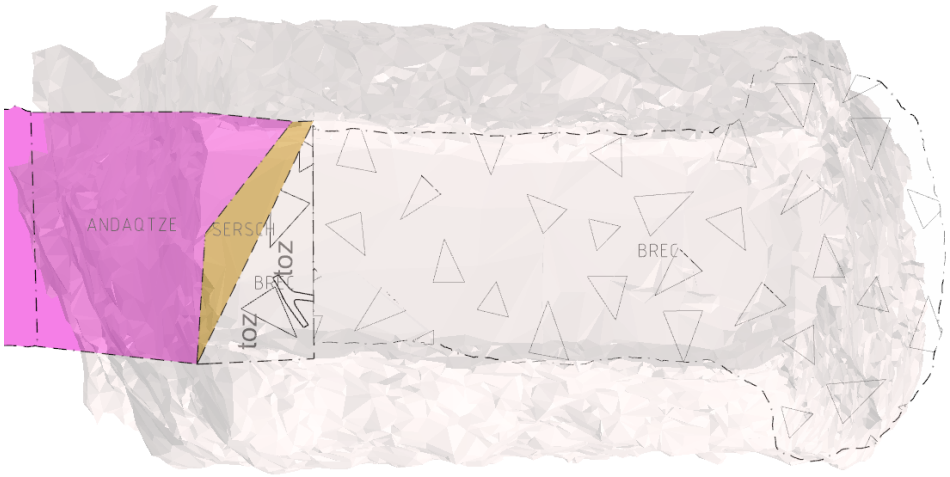

Figure 10: Facemap of bottom access drift for S0 (z=-647m).

3.2.3. Water

The Kankberg mine generally operates under dry conditions, although certain levels within the mine have some clear signs of water influences. An example is the cut-and-fill level 310, where water tends to fall from the roof in large quantities. Deeper parts of the mine, including the current sublevel stoping levels tend to not experience similar problems. No extensive hydrogeological surveys have been conducted for this level and, therefore, data are unavailable. For this reason, water conditions will be largely neglected, and overall rock conditions are assumed to be dry.

3.3. Layout & Mining Method

The Kankberg mine is an underground gold and tellurium mine, owned and operated by Boliden Mineral AB. The main mineralisation zone lies between 300 and 650 m below the surface (Figure 11), accessed via a ramp from the historic open pit, the Old Kankberg Mine. Mining began in 2012 and has continued uninterrupted, with total mine life production reaching approximately 5.26 Mt of ore. In 2024 alone, the mine produced 455 kt of ore with average grades of 3.63 g/t Au, 9.6 g/t Ag, and 164 g/t Te (Voigt & Falshaw, 2024). The mine has relied on cut and fill mining since the beginning. However, in 2025, deeper sections of the mine (red and white zones in Figure 11) are being developed using a long-hole sublevel stoping method to improve productivity and reduce costs. A total of 180 stopes are planned, typically 30 m high and 15 m wide, with lengths ranging from 4.5 m up to several tens of metres, which makes stope volume primarily dictated by length. Stopes are extracted in a primary–secondary sequence, allowing systematic backfilling and geotechnical control. The new mining method yields a significant improvement in mining costs.

- Cut and fill: 620 SEK/t
- Sublevel stoping: 520 SEK/t

3.4. Current D&B Practices

At the time of writing, only two stopes have been blasted thus far, using a similar pattern, with minor changes in the amount of holes and the burden. The current pattern was recommended by Forcit Explosives. Figure 12 provides an overview of the current progress within the stoping area. Table 6 gives an overview of the stope average CMS performance. This section will go over the current stope notes available for the blasted stopes, and briefly discuss the blasted uphole slots. The overview is a combination of the team's effort and the author's own reconciliation analysis.

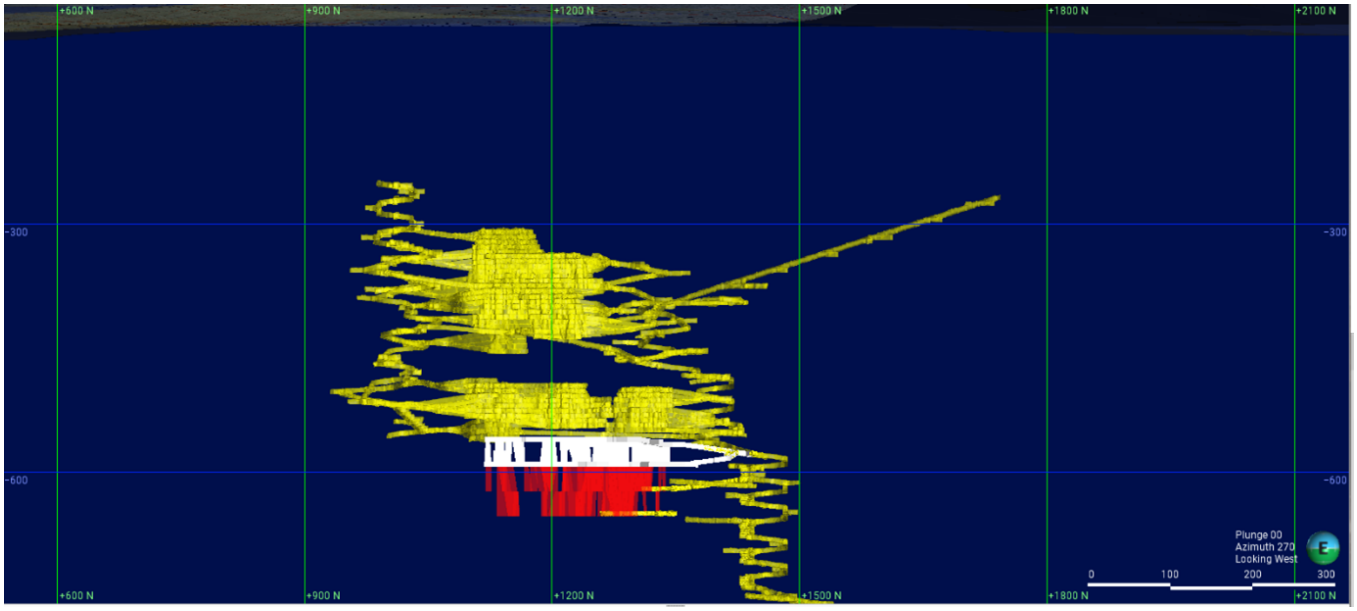

Figure 11: Mine overview: Excavated sections (yellow), Planned stopes (red & white)

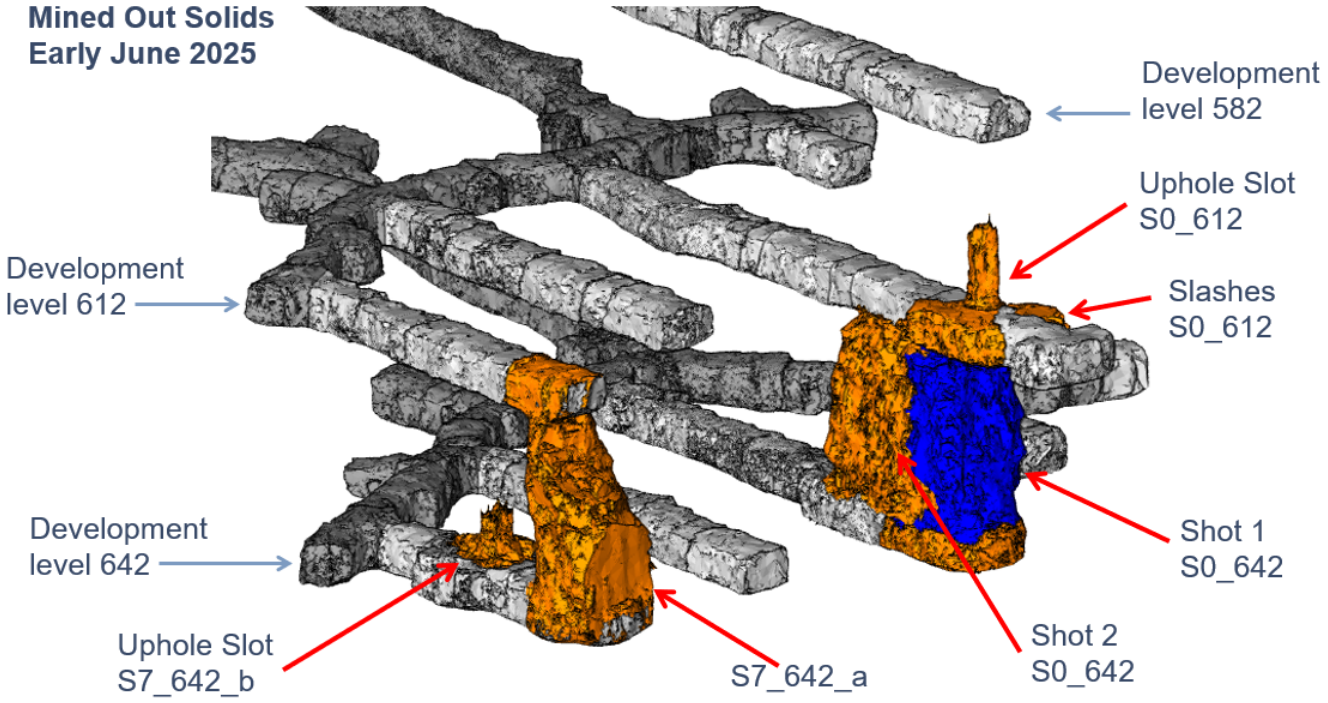

Figure 12: Overview of mined out solids in the stoping area (early June 2025).

Table 6: Overbreak and Underbreak Summary.

Stope	Planned Volume (m^3)	Overbreak (m^3)	Overbreak (%)	Underbreak (m^3)	Underbreak (%)
S0	8629	538	6.2	594	6.9
S7	2733	808	29.6	224	8.2

3.4.1. Stope Note

A stope note is currently in place that captures valuable information of pre- and post-blast results. The documentation contains 7 headers, respectively, Planning, Vent/Media/Backfill/Safety, Geology, Rock Mechanics, D&B,

Reconciliation, and Evaluation. The following checklist will briefly go over the most crucial data that are currently recorded.

1. **Planning**: working level, slashes (Yes/No), tonnage, grade and NSR
2. **Vent/Media/Backfill/Safety**: ventilation power, backfill recipe and method, distance to rescue chamber
3. **Geology**: rocktype, drill rates for development drifts, face mapping
4. **Rock Mechanics**: Geotechnical parameters from nearby drillhole data, various RMCs, ELOS prediction from stability graph, stress modelling
5. **D&B**: Uphole/Longhole, number of blasts, planned drilling meters, sub drilling (Yes/No)
6. **Reconciliation**: Over-/Underbreak per face within stope including volume, tonnes and grade
7. **Evaluation**: Comments on process in Swedish

The first stope that was blasted (S0 642) was thoroughly documented, serving as a strong reference. However, from the second stope onwards, documentation has become inconsistent or, in some cases, has not been maintained. This highlights a challenge. That is, collecting detailed information is valuable only when it is integrated into a feedback loop that informs and improves future designs. Ensuring that stope notes are consistently completed and actively used in design reviews will strengthen operational performance.

3.4.2. Stope 642 S0 / 1388C75

Figure 13a provides a plan view of the drill pattern used for the S0 stope. Figures 13b and 13c show the design of the planned stope. The contractor that conducts the charging and blasting made a report to assess the blast of S0. The vibration report noted the loss of blastholes 300, 600, 2100 and 4000 and suggested sympathetic detonation with blasthole 0. The reason for this poor result probably stemmed from high drilling deviations, as the probing measurements indicated severe deviations. For the same reason, blastholes 1800 and 2700 were destroyed. The opening had to be shot again. After the opening was created, the rest of the stope was successfully blasted according to plan. The key takeaways from Forcit Explosives were the significant drilling deviations, which should be addressed by adjusting drilling parameters such as slower drilling of larger holes or the purchase of an RBM. In addition, it was suggested to construct a clear structure for what documentation is needed at what stage. Specifically, analysis of measurements prior to charging, so that last-minute tweaking can be performed.

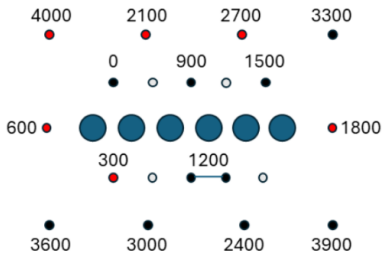

(a) S0 opening slot blast pattern (plan view), numbers indicate detonation delays in milliseconds

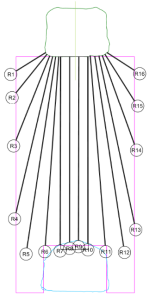

(b) Stope front profile of the opening slot (viewing North)

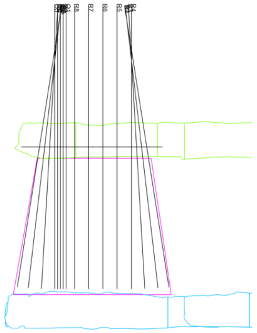

(c) Stope side view (viewing West)

Figure 13: Stope 642 S0 blast pattern and D&B geometry from multiple views.

Figures 14a and 14b show the scanned contours of the blasted stope compared to the planned shape. It displays the effective radius factor (ERF), which is the distance from the planned stope outline to the actual LiDAR-scanned outline. Distances were computed from each triangle face centroid on the actual mesh to the planned stope shell. Since the original data files were constructed by coarse triangles, the distance values were smoothed using a Gaussian filter for enhanced visuals. The subsequently smoothed values were assigned per vertex for the creation of the heatmap. Red zones mark excessive overbreak, and blue zones mark underbreak.

One can observe bellying at the stope side walls where the blastholes were located, resulting in significant underbreak. This suggests that the blast energy did not reach the middle sections between the outer toes of the blastholes, creating the need for either sub-drilling of the toes or closer toe spacing. In addition, a major overbreak is observed at both hanging walls of the trapezoid. One can also see that the stope was blasted in two rounds, where the first shot had more underbreak on the side walls, whereas the second shot had significantly higher levels of overbreak in the walls. This can be an indicator that blast-induced damage to the surrounding rock mass is visibly contributing to the blast

results. This is an interesting observation that can be crucial in D&B design, particularly for the secondary stopes where one may assume that the rock has been subjected to substantial blast-induced damage. However, another possibility that explains these observations is the direction of blasting. Here, the initial shot was directed inward (towards the slot raise), while the second shot was directed along the length of the stope. Intuitively, a combination of the two arguments seems most plausible. The transparent colouration (gold/breccia, purple/porphyry, and cyan/sericite quartzite) does not show patterns of significantly different overbreak and underbreak. During inspection of the facemaps drawn by the mine geologist, it was concluded that the upper level (617) was largely in agreement with the geologic model used here. However, the lower level also showed the presence of sericite schist, which was not included in the model. This mismatch implies the need for continuous updating of the geologic model, or decisions should not solely rely on the model.

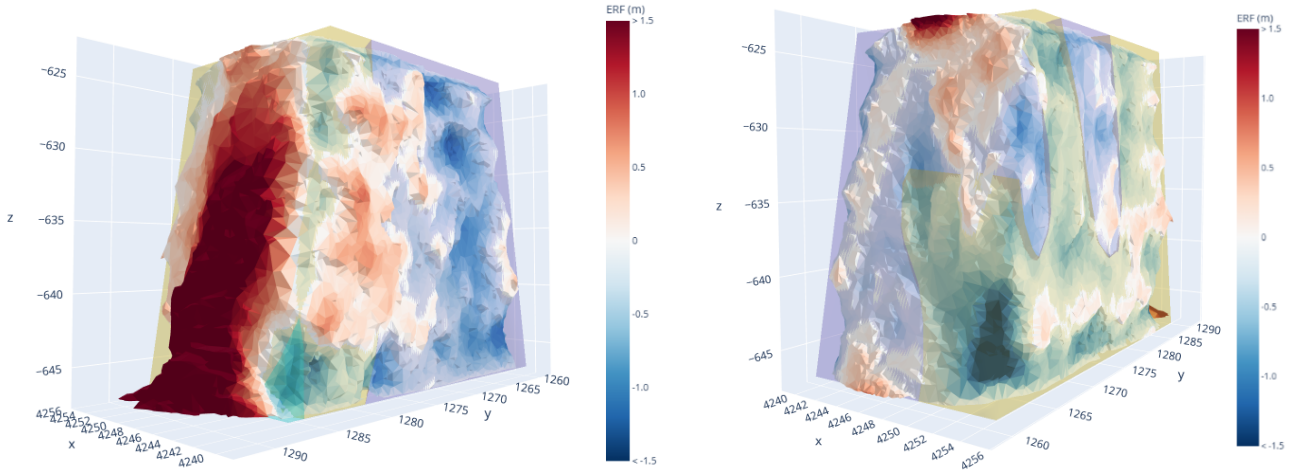

(a) Viewing South-East **(b)** Viewing North-West

Figure 14: Mapped stope face of 642 S0 ERF from two opposing perspectives.

3.4.3. Stope 642 S7a / 1388C76

The most recent stope, S7a at floor level 642, followed a similar D&B pattern. Subsequent reports on this blast's performance were not made. The blast result was poor, with boulders (Figure 15a) in the upper section of the stope, making mucking from the lower drift hazardous. Acceptable levels of cratering were observed in the top section of the stope. However, brow damage at the bottom access drift and high levels of overbreak are undesirable. The variation in blast performance between the foot and the hanging wall of the stope as seen in Figures 16a and 16b is striking. The geological face map indicated that four geological contacts were observed at the end of the bottom access drift. These geological contacts might have been potential weakness planes that caused severe overbreak. Furthermore, severe bellying can be observed similar to the first stope, with additional sidewalls where it appears that the drilled blastholes did not detonate at all. Differentiating between blast performance is difficult between the rock types (orange/andalusite quartzite, purple/porphyry, cyan/sericite quartzite, and gold/volcaniclastic), but Figures 16a and 16b do potentially show a more severe level of bellying at the blasthole toes in the sericite quartzite wall than in the porphyry wall.

Figures 17, 18 and 19 show the drillhole deviations of stope 642 S7a. It contains three data sets: blue represents the designed holes, green represents the anticipated heading of the Jumbo drilling rig, and red represents the handheld deviation measurements. The Jumbo drilling rig records the start and end points of each drilled hole, providing basic trajectory information. It was assumed (but not confirmed) that the Epiroc SIMBA E70 Jumbo drill rig does not use built-in gyroscopes to determine the end point but calculates the end point as a function of the collar, programmed direction vector, and the total drill length. Blast hole deviation measurements were performed using a handheld probe with a magnetometer, which captures the 3D path of the hole at 2 m intervals. Figure 18 illustrates serious deviations and a strong correlation with respect to the length of the drillhole. Another observation is that all the measured holes have an offset to the left with respect to both the designed and the Jumbo's anticipated holes. This can originate from multiple theories, and a leading possibility is a problem in the observed offset originating not from the true deviation of the drillhole, but from systematic azimuth errors inherent to magnetometer-based surveying, which can exceed 2° without proper calibration or correction (Twining & Lindsey, 2016). So, a hole length of 24 m can result in lateral offsets of nearly 1 m, consistent with the deviations observed in Figure 18. In future cases this can be solved by aligning breakthrough holes with LiDAR scans from the upper and lower drifts and correcting for the error, or by using more precise tools such as a gyroscope based system. If the deviations are not attributed to the error of

(a) Boulder at 642 S7

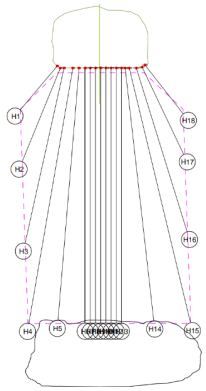

(b) Stope front profile (viewing North)

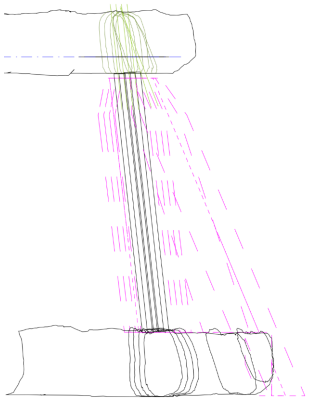

(c) Stope side view (viewing East)

Figure 15: Stope 642 S7a muckpile and development geometry from multiple perspectives.

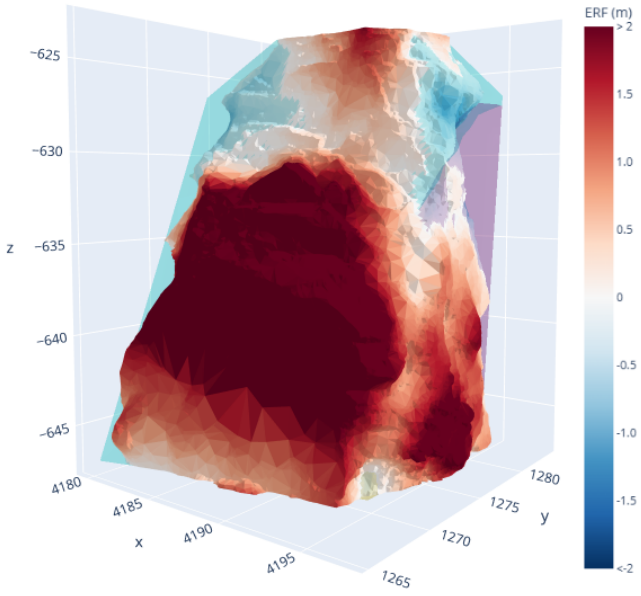

(a) Viewing South-East

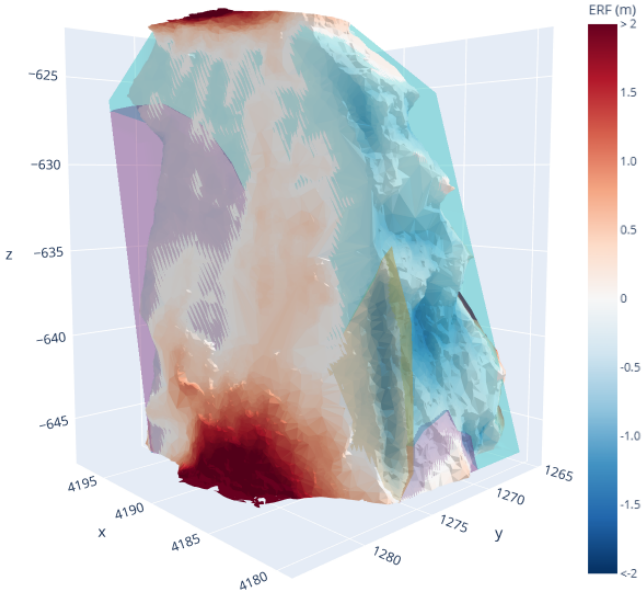

(b) Viewing North-West

Figure 16: Mapped stope face of 642 S7a ERF from opposing directions.

the measurement device, another plausible cause is a misalignment of the fixed point of the Jumbo rig. Despite the machine thinking it was in a certain position and drilling at a specific angle, instead it did the same from a wrong origin point. Another, less likely theory, the presence of magnetic ore nearby. According to geological understanding, Kankberg has no magnetites or similar minerals. However, other mines in the area, such as Kristineberg, face serious distortions for this reason. All in all, it is clear that these deviations make blasting an opening slot extremely difficult and that a design that accounts for these measurement inconsistencies and/or difficult drilling conditions would be beneficial.

As illustrated above, 642 S7a is by far the most complete data set available in this thesis and will be highlighted in later parts of the thesis as well. Both MWD and blasthole deviation data were obtained for this stope, making it particularly rich in data availability. The first stope (S0) did have deviation measurements as mentioned in the Forcit Explosives report, but on further inspection it was missing most of the opening slot holes. Furthermore, Forcit's conclusions were very much linked to the deviation measurements, yet no comment on correction was present. This suggests that poor performance could have been mislabeled as the result of deviations. Additionally, no MWD data was collected for S0, making it less suitable for deep analysis.

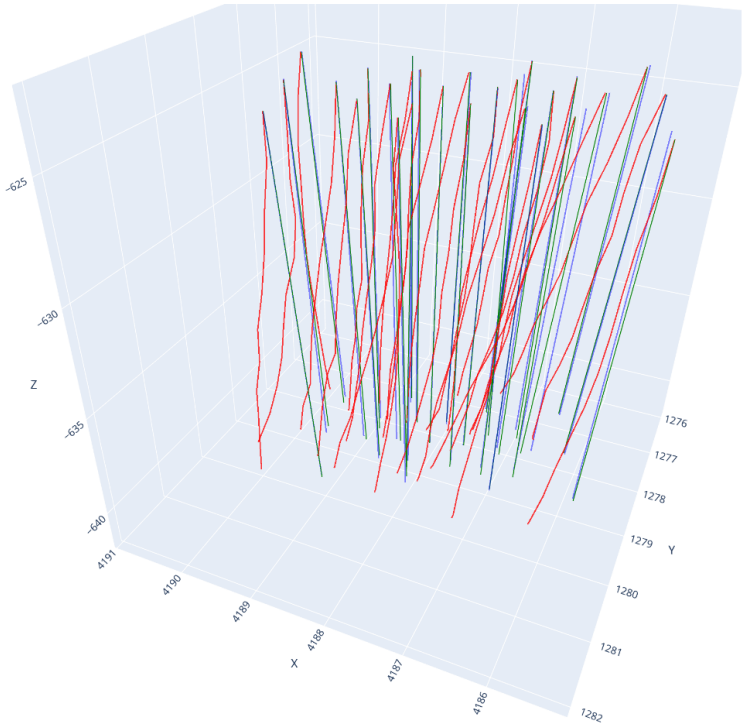

Figure 17: 3D visual of s7a 642 drillhole profiles.

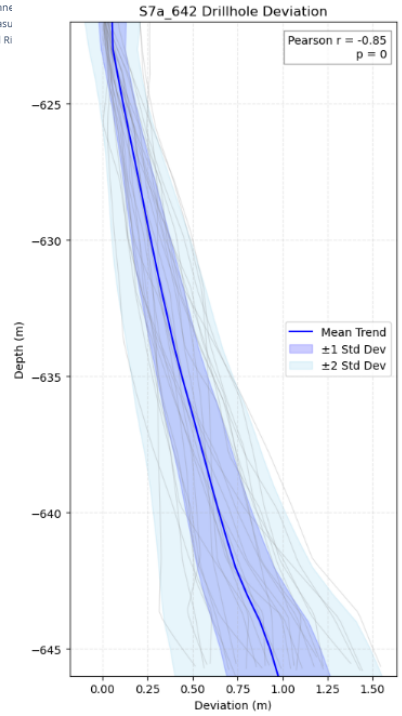

Figure 18: Drillhole deviations and correlation with depth in S7a 642.

Figure 19: Opening slot plan views, collar and toe level.

3.4.4. Future Stopes

The next two stopes, 612 S0 and 642 S7b (Figure 12), are being drilled in two parts. First, up-hole drilling and blasting of the opening slot is performed from the lower drift, and secondly, down-hole drilling of the upper slot and the production blastholes is performed. This reduces the necessary pull by 50%, and is expected to result in a better blasting outcome. From the scans made of the initial uphole opening slots moderate results were observed. The S0 612 uphole slot showed a clean slot wall, but did not fully reach the desired pull of 12 m. The S7b 642 uphole slot showed poor performance because it did not reach the desired level of pull and had severe brow damage. In the process of writing this thesis, more and more data became available. However, the core analysis will primarily use S7a 642 as a vocal point.

4 Methodology

This chapter presents the methodological steps taken to construct a blastability classification for Kankberg. The work includes the processing of relevant datasets, the execution of laboratory tests, and the formulation of Lilly's BI for Kankberg as well as an enhanced version developed using fuzzy theorem. Each stage is described in detail to establish a transparent and reproducible framework for generating the indices, while later chapters focus on comparing these indices with external proxies and exploring their implications for drill and blast (D&B) design.

4.1. Data Acquisition and Handling

To obtain all parameters for a BI, data that feed into the BI calculations need to be selected and prepared to provide relevant information. The availability of data is vast, as was described in Chapter 3. Therefore, it is crucial that careful consideration is taken to properly select the right data.

4.1.1. Geotechnical Drillhole Data

A large part of the data that feed into the BI is geotechnical in nature. As such, much of the data used come from geotechnically logged diamond drillholes. The drillhole data set is extensive and covers a much greater volume than the stoping region. Of particular interest when selecting from this data set are the BRQD (Section 4.1.1) and the joint spacing parameters. Although the data set includes more categories, such as joint roughness and joint fill, which are interesting to study for model evaluation or future validation, these variables do not directly feed into the BI. The data were therefore included in the overall drillhole analysis without seeing direct utilisation in the model.

To make sure that the BI reflects conditions specific to the stoping area, only values from drillholes that intersect the stope volume were selected. This was done by defining a rectangular bounding box around the full stoping extent and intersecting all drillholes that fall within this box. Statistics were then run on the resulting subset. For BRQD and RMR, the mean values and standard deviations were calculated. Joint roughness, joint fill, and joint spacing were categorised by frequency of occurrence per rock type.

Rock Quality Designation

The RQD (Deere, 1964) uses drill core logs to quickly obtain a quantitative estimate of the quality of the rock mass. It is often the only method used for the determination of jointing density. The procedure can be summarized with the following equation.

$$RQD = \frac{\sum \text{Length of core pieces} > 10\text{ cm}}{\text{Total length core}} \cdot 100\% \tag{4.1}$$

Samples with a low RQD percentage are classified as poor and vice versa. RQD is considered an assessment of in situ conditions, therefore, drilling and handling induced fractures should be accounted for. Boliden has developed a correction for the Kankberg mine as illustrated in Figure 20. While the robustness of this correction can be questioned due to the limited sample size used for the polynomial fit (N=7), it is considered acceptable for the purposes of this thesis. From Figure 20, we can observe that the correction factor then becomes:

$$RQD = BRQD \cdot (-8 \cdot 10^{-5} \cdot RQD^2 + 0.0006 \cdot RQD + 1.2089) \tag{4.2}$$

This correction factor is non-linear and should be solved numerically. This was done using the Newton-Raphson method, which is an algorithm that guesses a starting point and iterates until convergence is reached within a tolerance limit over a set amount of iterations. In this report the initial guess was the input BRQD, the tolerance limit used was $1 \cdot 10^{-8}$ and the maximum number of iterations was iter_max = 1000.

It is important to note that RQD is generally debated in the field of rock engineering. Drawbacks are, the dramatic changes based on borehole orientation due to the method inherently being directionally dependent, and the lack of

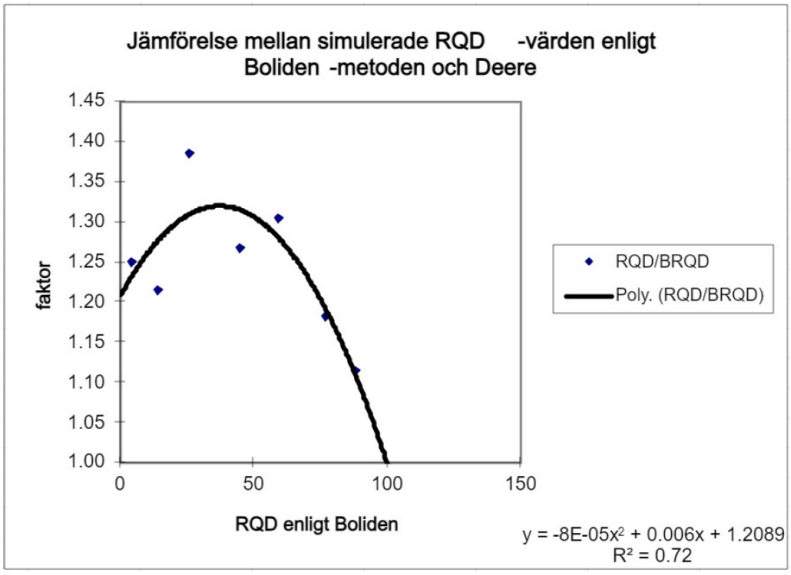

Figure 20: Conversion Factor BRQD to RQD.

consistency in assessment (Figure 21) (Palmström, 2001). Nevertheless, this parameter is still widespread within the domain of rock engineering.

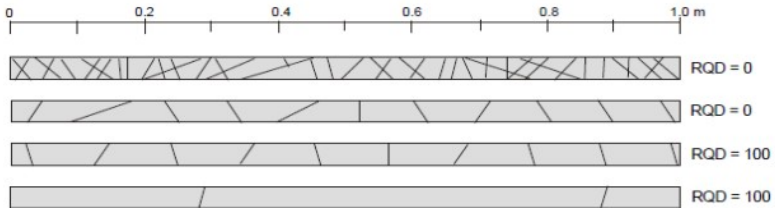

Figure 21: Example of RQD inconsistency (Deere, 1989).

4.1.2. Joint Orientation Data

Joint plane orientation data is difficult to assess if the drillholes are not oriented. Underground, especially in early-stage development like the stoping area, exposure to clean rock faces is slim. No datasets outlining orientation data are available to infer JPO with any level of confidence. Therefore, a more practical approach was adopted to estimate JPO values based on the relationship between the principal stress direction and the general stope orientation. The underlying assumption is that the dominant joint sets align with this stress field, due to joints tending to form perpendicular to the least principal stress.

This thesis tests this assumption by observations from the S7 blast round. Figure 15c revealed significant overbreak within a caved section of the hanging wall, which is assumed to have failed along a significant natural joint surface. The LiDAR scan will be analysed in the GEM4D software package. The software allows retrieving orientations of surfaces and comparison with the believed principal stress direction. Although this approach offers only a restricted solution in comparison to oriented core data or detailed face mapping data, it is deemed adequate to proceed with the creation of a BI.

4.1.3. Laboratory Tests

As previously discussed, it is essential to understand rock mechanical behaviour and therefore also the testing procedures. The selection of appropriate tests depends heavily on the desired measurable parameters and the limitations of both the methods and the available equipment. UCS and density measurements will directly feed into the BI's, the elastic moduli and acoustic wave velocities form a strong addition to data interpretation beyond the use in the BI's.

This research targets the compressive strength specifically, since it is a highly usable rock property and key ingredient for the BI's. Laboratory testing requires a similar selection process, considering the specific rock properties and apparatus constraints. Since only data on inferred UCS values is available, the need to do additional direct UCS tests

is present. In combination with the UCS. The following sections explain the testing methodology and review the applicability and accuracy of these methods.

Unconfined Compressive Strength (UCS) Testing

Laboratory tests offer controlled conditions by eliminating the variability and unknowns present in field measurements. The UCS tests, as described by Goodman (1991), remain a standard method for determining the true compressive strength of rocks.

As described in Goodman (1991), the stress-strain curves of the UCS have characteristic domains (Figure 22). Initially, the curve exhibits a concave-up region, which reflects seating effects and closure of pre-existing microcracks. This is followed by a nearly linear section, the elastic domain, where deformation is recoverable and stress is proportional to strain. The slope of this linear region defines the Young's modulus of the material. Beyond the elastic limit, the curve enters the yielding domain, where plastic deformation begins and microcracks propagate and nucleate. As stress continues to increase, the material reaches its peak strength (σ_{UCS}). Post-peak, stress typically drops as localised failure zones develop, forming the post-peak domain, which reflects strain-softening behaviour or brittle failure.

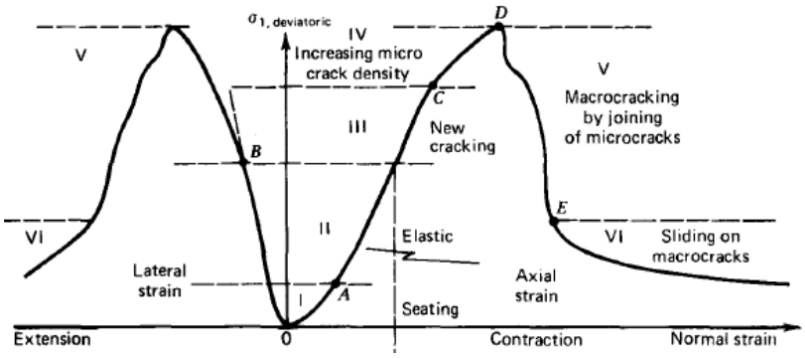

Figure 22: Stress-strain curve of an arbitrary sample during UCS test (Goodman, 1991).

The elastic constants of a rock can be determined because of the continuous measurement of the samples. The two measurable moduli are, respectively, the Youngs Modulus (E) and the Poisson's Ratio (ν). Young's Modulus is found by taking the slope of the axial strain curve in the elastic domain, and can be described by the equation:

$$E = \frac{\sigma}{\epsilon} \tag{4.3}$$

It is not uncommon for rock to have multiple linear elastic domains, with their respective Young's Modulus. This special case is usually referred to as the dynamic elastic modulus. The Poisson's ratio, which describes the materials' tendency to deform perpendicular to the loading direction, is described by the following equation:

$$\nu = -\frac{d\epsilon_{radial}}{d\epsilon_{axial}} \tag{4.4}$$

where the Poisson's ratio is the fraction between the change in radial strain and the axial strain.

Standards and References

The laboratory testing procedures for UCS were conducted in accordance with ASTM International (2017). Where applicable, the testing methodology was supplemented by the ISRM by Ulusay and Hudson (2007). According to ASTM International (2017), a sample should maintain a length-to-diameter ratio between 2.0 and 2.5. ASTM also recommends a minimum diameter of 47 mm. However, mining-related samples often deviate from this as a result of extraction limitations. Although the standards recommended the length-to-diameter ratio, some samples used in this study had slightly lower ratios due to sample preparations. This deviation is acknowledged and any potential influence on the test results is considered in the interpretation and discussion of the data.

Test Setup

UCS tests apply an axial and constantly increasing load on a cylindrical rock specimen until failure. An optional radial strain chain enables multidirectional strain measurement, used for elastic property analysis. The UCS configurations used are illustrated in Figure 23. Three different setups were used during the tests. Initially, the setup was intended to measure the acoustic wave velocities during the UCS test (Setup 0). The axial strain is measured by two LVDTs that function as displacement gauges, and the radial strain is measured by a sensitive chain in the centre of the

cylindrical sample. Two iron holders carrying S-wave transducers shoot an acoustic pulse every 10 seconds to gather acoustic data. The sending transducer shoots a pulse generated by an oscilloscope and amplified by an amplifier through the rock sample. The receiving transducer sends the signal back to an oscilloscope which is then translated into a readable signal by a computer. Once the sensors are placed and a shear-wave paste is applied between the S-wave transducers and the specimen, the samples undergo constant loading by a 500 kN hydraulic press. This press is set to achieve a continuous strain rate (0.005 mm/s). A computer connected to the strain gauges records the data at a sampling rate of 1 Hz. Once a sample visibly fails or the stress drops significantly, the test is stopped.

As mentioned, multiple setups were used. During the first test, which exceeded 150 MPa, the iron holders that carry the acoustic transducers showed signs of deformation. For this reason, the author could not continue using Setup 0 with S-wave transducers, since uniform test conditions could no longer be guaranteed. Setups 1 and 2 do not measure acoustic velocities simultaneously. In these cases, the acoustic wave velocities were measured prior to loading the sample into a separate setup. The use of multiple setups does not affect the test results as long as the measured strain accounts for the strain behaviour of the setup. To ensure this, one needs to calibrate the machine accordingly, which is explained in the following section.

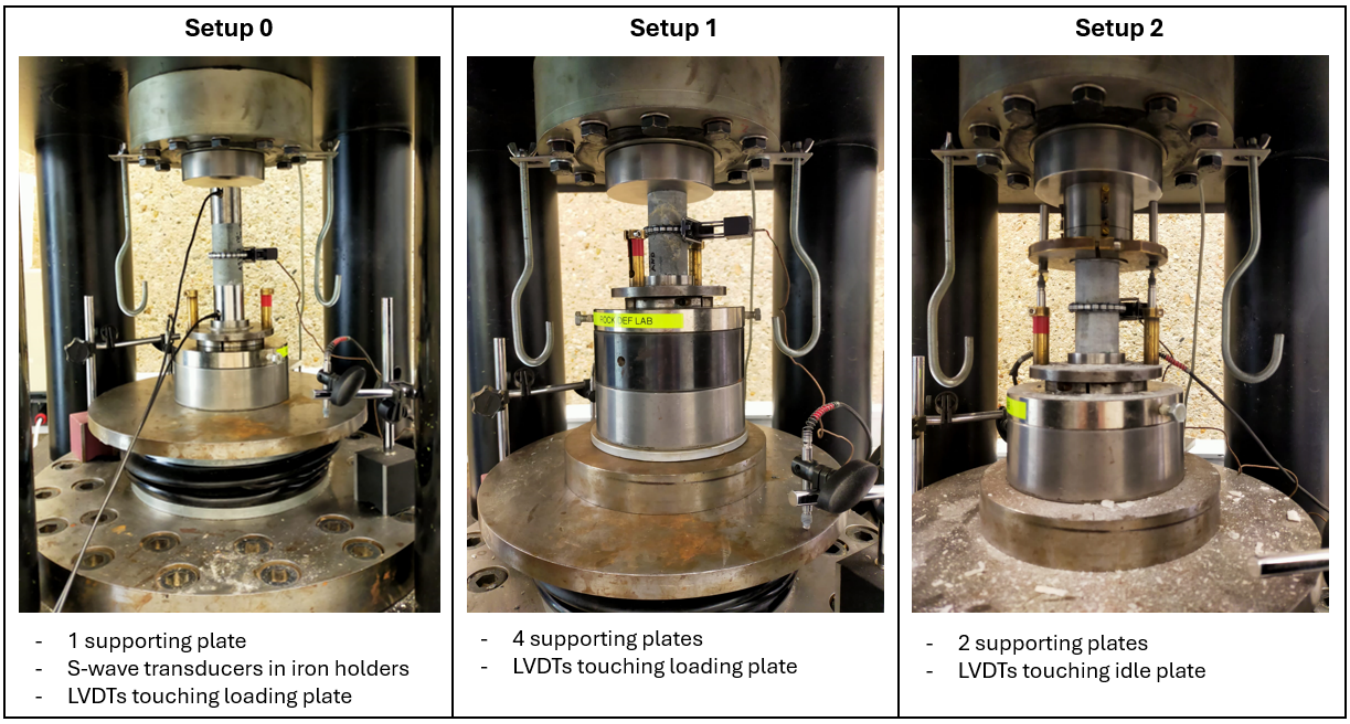

Figure 23: UCS test setups 0, 1 and 2.

Machine Calibration

The UCS testing setup uses LVDTs to measure the axial displacement of the lower loading piston. This displacement includes not only deformation of the rock sample, but also elastic deformation of the supporting loading frame and plates. To isolate the true strain of the sample, a correction must be applied. A calibration test is performed using an aluminium dummy, which has a known Young's Modulus of 70 GPa (M.I.T., n.d.). The deformation of the dummy is measured under load and compared to the theoretical elastic response:

$$\epsilon_{\text{al,ideal}} = \frac{\sigma}{E_{\text{aluminium}}} \tag{4.5}$$

The difference between the measured strain and the ideal strain is attributed to the machine's compliance. Assuming linear elastic deformation of the system, a machine compliance term is defined as:

$$C_{\text{system}} = \left(\frac{1}{E_{\text{fit}}} - \frac{1}{E_{\text{aluminium}}} \right) \tag{4.6}$$

This compliance is then used to correct all subsequent UCS tests.

$$\epsilon_{\text{sample}} = \epsilon_{\text{measured}} - C_{\text{system}} \cdot \sigma \tag{4.7}$$

This approach assumes that the frame behaves linearly throughout the full stress range. Although the aluminium calibration test is limited to lower stresses to prevent yielding, the extrapolation is justified for a stiff, elastic frame.

Sample Description and Preparation
Before performing the tests, the samples required adequate preparation to make the conditions of testing equal. The samples were initially cut with a handsaw, but upon inspection of the levelness of the edges the samples were not deemed fit for testing. Levelness is critical for UCS to spread the load evenly across the samples. Therefore, it was decided to grind the samples. The rock samples were ground to be perfectly level. This was done by removing 1 mm on both edges at a 0.015 mm/cut rate. This resulted in some samples falling below the original threshold value of 2:1 for the H:W.

Since the samples were not drilled simultaneously, their exposure to surface conditions was unknown. To remove as much variation as possible, it was decided to dry all samples at 60° Celsius for 24 hours to remove excess moisture. Therefore, it is assumed that all rock samples were tested under dry conditions.

Before testing, the rock samples were carefully measured, weighed and described by the author. This information can be found in Table 7 below.

Sample ID	H (mm)	W (mm)	Ratio	ρ (Kg/m^3)	Alteration	Note
AND1353_1354	77.48	38.75	2.00	2977		Competent, mineralized
AND1360_13615	76.71	38.55	1.99	2818		Competent, mineralized
AND1310_13115	77.68	38.68	2.01	2839		Fractures, mineralized; no cross-cut
AND600_6015	77.19	38.69	2.00	3011		Competent
AND1201_1202	78.64	38.73	2.03	2769		Major fractures; full cross-cut
AND6875_689	77.59	38.72	2.00	2965		Fractures; no cross-cut
ANDAQTZ1084_1085	76.38	38.80	1.97	2865	A4, T3	Competent, mineralized
ANDAQTZE13185_1320	74.70	38.57	1.94	2872	A4	1 major fracture, mineralized; no cross-cut
ANDAQTZE1831_1833	77.91	38.73	2.01	3318	A4	Competent, highly textured
ANDAQTZE22195_2221	76.25	38.79	1.97	2825	A5, T3	Competent, highly textured
ANDAQTZE2240_22415	78.57	38.77	2.03	2801	A5, T1	Competent, some texture
BREC2133_21345	78.15	38.90	2.01	3198	T4	Fractures, colour boundaries; no cross-cut
BREC19345_1936	78.99	38.86	2.03	2804	T4	Fractures, mineralized, veins; no cross-cut
BREC1947_19485	76.68	38.98	1.97	2805	T4	Major fractures, textured; full cross-cut
BREC7655_767	74.62	38.91	1.92	3467	T5, A1	Highly textured, fractures; no cross-cut
BREC935_9365	76.72	39.01	1.97	2866	T4, A1	Competent, veins
BREC15705_15715	77.72	38.61	2.01	3111	T4	Competent, colour boundaries
QTZFSPPO1764_17655	77.06	38.79	1.99	2648	A1, T1	Major fractures; full cross-cut
QTZFSPPO1780_17815	77.48	38.80	2.00	2693	A2	Fractures, brecciated; full cross-cut
QTZFSPPO1860_18615	75.94	38.95	1.95	2646	A2	Minor fractures, mineralized; no cross-cut
QTZFSPPO17055_1707	76.44	38.79	1.97	2709	A3, T1	Highly textured
QTZFSPPO9215_923	77.63	38.95	1.99	2641	T2, A1	Fractures at the rims, colour boundaries
SERQ6755_677	76.55	38.73	1.98	2837		Competent, some texture
SERQ610_6115	77.61	38.85	2.00	2728		Major fractures, some texture
SERQ6365_638	76.94	38.89	1.98	2747		Competent, highly textured, mineralized
SERQ6015_6025	77.08	38.87	1.98	2711		Competent, some texture
SERQ6105_612	77.75	38.89	2.00	2713		Fractured, some texture; no cross-cut
VOLCCL9315_933	77.17	39.00	1.98	2799		Minor fractures, mineralized; no cross-cut
VOLCCL1023_10245	77.25	39.02	1.98	2729		Competent, mineralized
VOLCCL1277_12785	77.09	38.60	2.00	2929	A2	Competent, mineralized
VOLCCL7445_746	77.60	38.71	2.00	2767	A3	Competent, mineralized
VOLCCL843_844	76.76	38.74	1.98	2753	A1	Competent, highly textured, mineralized

Table 7: Sample properties prior to testing.

Data Processing
After testing, the data are ready to be processed. Before any interpretation was performed, the raw data were corrected by machine calibration. Then, using Python scripts, stress-strain plots were created and visually inspected. UCS values were found by finding the maximum stress within the data file. To derive the Young's Modulus from the stress-strain curves, automated linear regression is performed to find the most linear part of the curve, i.e. the elastic

domain, by means of optimising the fit with the best R^2 possible. From the same linear section, the Poisson ratio is subsequently calculated. For UCS values, the international standard requires that correction factors be applied for specimens that do not meet the dimension requirements. The most commonly used correction factor is suggested by Brown (1981):

$$\sigma_c = \sigma_m \left(\frac{L}{D} \right)^{0.2} \tag{4.8}$$

where σ_c is the corrected UCS, σ_m is the measured UCS, and L/D is the length-to-diameter ratio of the specimen. The ISRM by Ulusay and Hudson (2007) uses a stricter correction using a power of 0.3. However, this strict correction factor is not as commonly used. All reported values in the report will have been processed and corrected accordingly.

Acoustic Velocities
Initially, Setup 0 was designed to measure acoustic P- and S-wave velocities in parallel with UCS testing. The system was configured to take readings at 10-second intervals throughout loading. The second approach yielded a separate acoustic test prior to loading of the samples. However, during post-test data processing, it became evident that the recording microphone had logged the wrong data channel across all samples, and no reliable acoustic velocity data could be recovered.

As a result, this portion of the setup was discontinued in future sections. A workaround was achieved by indirectly estimating the acoustic velocities, based on the density and elastic moduli derived from stress–strain data, as described by Equations 2.1 and 2.2. Despite this workaround, differences persist, the direct measurements were supposed to allow the acquisition of the P- and S-wave prior to loading, and are now limited to the dynamic elastic moduli.

4.2. Blastability Assessment

This thesis ultimately aims to link rock properties to D&B design through the use of an index which is built up of said properties. As discussed in the theoretical background, the widely accepted BI outlined by Lilly (1986) will serve as the basis to bridge this gap between rock properties and practical use in mining applications.

4.2.1. Lilly's Empirical Model

Lilly's empirical model is based on the principle that certain geologic and geotechnical properties significantly affect the blasting behaviour. The complete formulation for the BI is defined in Equation 2.4. Originally, the input variables do not follow a strict formulation and can change based on site-specific knowledge. This allows for the creation of an BI with limited data. The BI score is a composite of the five input variables; RMD, JPS, JPO, RDI, and H. Each of these variables can be assigned a scoring value based on field and laboratory data. The following paragraphs outline how Lilly's input variables were obtained.

The RMD reflects the overall condition and structural integrity of the rock mass. At Kankberg, this was evaluated using RQD values obtained from geotechnical core logging from drill holes within the stoping area. A value of 10 was assigned to RQD with scores below 25%; 20 to 25%-50% ; 30 to 50-65%; 40 to 65%-80% and 50 to BRQD values above 80%. This scoring uses 5 scoring bins instead of the original 3 scoring bins and is used to enhance the discrimination of rock quality for the Kankberg data.

JPS was assessed using the spacing data, also from the geotechnical logs. Since the data showed relatively heterogeneous degrees of joint spacing, the characteristics of the dominant joint spacing were complemented by the second most prominent spacing value using a weighted sum approach. The output value is then rounded to the nearest score. Similarly to the RMD, the JPS scoring adopts a 5-bin system instead of the original 3-bin system, for the same reason, to provide greater granularity in describing the rock mass.

As detailed in section 4.1.2, the JPO value was estimated based on the principal stress direction relative to the stope orientation. This assumes that the dominant joint set aligns with the regional stress field. Based on this, the scoring followed the original approach by Lilly where the joints were subhorizontal, a score of 10 was applied; joints that dipped out of the face received 20; those that struck normal to the face received 30; and those dipping into the face received 40. Due to the need to initially blast an opening slot, careful consideration should be taken to choose the correct nearest free face. For example, depending on the location of the blasthole with respect to the opening slot (free face), the JPO will change.

RDI was calculated on the basis of laboratory-determined densities converted into specific gravity values from core samples. This transformation is typically done to turn the density value unitless for easier interpretation between

different states of matter. The following transformation was used, consistent with Lilly's model (Lilly, 1986):

$$\text{RDI} = 25 \cdot \text{D} - 50 \tag{4.9}$$

where D is the density of the rock mass in tonnes per cubic metre.

H was derived directly from the UCS values obtained by laboratory testing. Rather than relying on the qualitative Mohs scale, which can be subjective and less representative of fragmentation resistance, UCS provides a quantitative measure of the mechanical strenght of the rock. Based on Lilly's guidelines, the strength rating is determined as follows:

$$H = 0.05 \cdot UCS \tag{4.10}$$

where UCS is given in megapascals.

After assigning all input variables, the BI was calculated using the formula provided in Section 2.4. Where direct measurements were unavailable, values were inferred from educated guesses which were supported by either the literature or proxy data. As hinted at before, it is not unlikely that the proposed rating scores may not adequately differentiate between the rock types encountered in the Kankberg rock. For example, some of the scoring characteristics are coarse, which limits the interpretive power. Since the goal is to differentiate between rock types in terms of blastability, the use of more bins than is portrayed in the scoring methodology as outlined above could be used to suit site-specific needs. These adaptations aim to preserve the original's formulation whilst creating more site-relevant contrast. The site-specific score used (increased bins) can be found in Appendix A. Given the observed variability in data quality and the limitations of some input scales, further refinement can include adjusting the weights of input variables based on their reliability, or selectively using inputs, such as UCS, based on the condition of the tested specimen. These adjustments aim to better capture meaningful contrast while reducing the impact of uncertain or inconsistent data.

4.2.2. Fuzzy Set Enhanced Model

To overcome the limitations of rigid class boundaries in empirical models such as the BI, an FIS was developed based on the approach proposed by Azimi et al. (2010) and Alipour et al. (2018). This method should allow for more flexible and accurate blastability prediction in geologically variable environments by incorporating both expert judgment and semi-quantitative data, whilst lowering sensitivity to small changes in variables at classification boundaries.

The five input variables; RMD, JPS, JPO, RDI, H, are expressed using five fuzzy linguistic terms (*Very Low*, *Low*, *Medium*, *High*, *Very High*) and modelled using triangular membership functions.

$$\mu_A(x) = \begin{cases} 0 & \text{if } x \leq a \\ \frac{x-a}{b-a} & \text{for } a \leq x \leq b \\ \frac{c-x}{c-b} & \text{for } b < x \leq c \\ 0 & \text{if } x > c \end{cases} \tag{4.11}$$

where a, b, and c are, respectively, the lower limit, the peak, and the upper limit of the membership functions. The crisp input values derived from the data are converted into fuzzy values by determining their degrees of membership in the associated fuzzy sets using equation 4.11. To better reflect the variability and distribution of site-specific geotechnical properties, non-uniform membership functions were defined for the lab-tested UCS and RDI. Their membership functions were designed to follow the statistical behaviour of the measured samples, by means of the statistic quantiles over all rock types. This approach aims at benefiting the site-specific needs to create contrast between rock types by only using a range of measured values. Uniform triangular MFs were retained for RMD, JPS, and JPO, as these variables were not strongly skewed and reflected a more discrete range of values. An example of both membership functions is found in Figure 24, a table of selected ranges and fuzzy terms can be found in Appendix A. A set of if-then rules was then developed to mimic human-like decision making. Each rule relates specific fuzzy conditions of the input variables to a fuzzy classification of blastability, an example of a fuzzy rule will look as follows:

IF RMD is *High* AND JPS is *Wide* AND H is *Soft* THEN BI is *Moderate*

Since five linguistic terms are given to each input variable, a total number of possible combinations is $5^5 = 3125$. The rule base was designed to cover all meaningful combinations of the five input variables, which means that physically highly implausible combinations were filtered from this rule base. The set of filtered combinations can be found in Appendix C. A total of 4 constraints were implemented and 480/3125 combinations were removed. Instead of manually defining each rule, a scoring scheme was applied: Each fuzzy term was assigned a numerical score (0–4),

and the rule consequence was generated based on the weighted average of the input term scores. The weights can be changed and adjusted based on the domain knowledge of the influence of each input on blastability. For example, a trial favours the UCS and RDI weights by increasing them to 3 instead of 1, due to higher confidence levels based on the testing method. Conversely, JPO is assigned a lower weight, 0 instead of 1, due to lower confidence. The aggregated score was then assigned to one of five fuzzy output terms that represent the FBI.

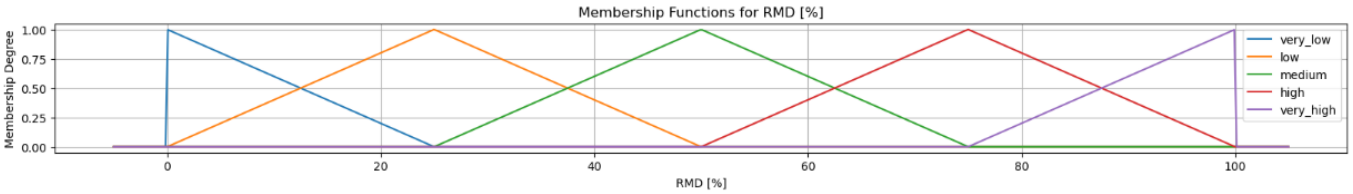

(a) RMD membership function, triangular and uniform.

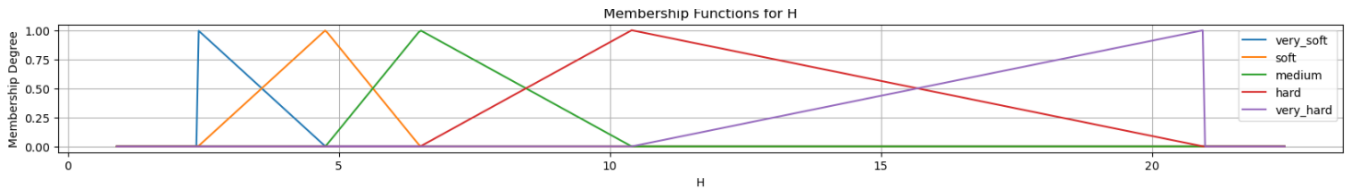

(b) H membership function, triangular and data-driven.

Figure 24: Illustration of the two types of member function utilized in the FIS.

The Mamdani-type inference approach was used for this problem. The degree of activation for every rule was calculated using the minimum operator (AND).

$$\mu_{\text{out}}(z) = \min\left[\mu_{A_1}(x_1), \mu_{A_2}(x_2), \ldots, \mu_{A_n}(x_n)\right] \tag{4.12}$$

where $\mu_{A_i}(x_i)$ represents the degree of membership of the input x_i in the fuzzy set A_i. The outputs of all fired rules are aggregated using the maximum operator:

$$\mu_{\text{agg}}(z) = \max_j \left[\mu_{\text{out},j}(z)\right] \tag{4.13}$$

The aggregated fuzzy output is then defuzzified to a crisp FBI value using a discrete centroid approximation, where the outputs were assigned to a crisp value. This method is favoured over a true centroid of area method due to simplicity and speed. Since the resulting BI will be used categorically, a discrete method is preferred over a continuous one. The final FBI was calculated as the weighted average of said crisp values:

$$\text{FBI} = \frac{\sum_i \mu_i \cdot z_i}{\sum_i \mu_i} \tag{4.14}$$

The initial development and testing of the fuzzy model was performed using the Scikit-Fuzzy Python library, which provides a streamlined implementation of FIS. However, due to performance limitations and breakdowns when working with large rule bases (> 1000 rules), the final model was implemented in a custom Python environment. This custom model allowed for much better performance and full control over membership function design, rule evaluation, and defuzzification logic.

4.2.3. BI and FBI Sensitivity Analysis and Model Comparison

Although the mathematical structure of both the empirical and fuzzy BI models is relatively straightforward, a sensitivity check was included to verify the influence of each input parameter. Given the linear nature of the empirical model, each variable contributes equally to the final BI score. In the fuzzy model, the influence of each input depends more on the shape of the membership functions and their overlap. If the model is implemented correctly, it is expected that variables with broader data ranges or more sharply defined membership transitions show the largest impact on the final BI classification. These results should confirm the intuitive weighting observed during model development. Furthermore, a comparison between the BI and FBI will highlight the added value of using a more complex method and will serve as an assessment of whether the fuzzy enhancement is worthwhile.

4.3. Measure-While-Drilling Rock Factor for S7a Opening Slot

4.3.1. Data Acquisition and Inspection

Raw MWD files were delivered by the drill rig in .xml format and contained time-stamped sensor data sampled every 30 cm of drill advance. Rig data being recorded are the following: penetration rate (PR), rotational pressure (RP), percussion pressure (PP), feed pressure (FP), damp pressure (DP) and flushing pressure (FLP). The initial visual screening revealed three recurrent quality issues from these data sets:

1. Duplicate logs; New drill runs were occasionally written to new files with the same hole identifier (possibly reaming).
2. Interrupted logs; several files end abruptly below the design length (Table 8).
3. Concatenated logs; In some cases, drilling resumes in the same file from random depths after reaching the desired drill depth, indicating that multiple drill holes were likely appended.

The 26 files were manually assigned to their correct deviation drill paths based on their collar coordinates. Five holes contained incomplete depth coverage, but were retained because the valid portion still contributed to subsequent analyses. Files with concatenated data were filtered to include only the first portion up to reaching the desired drill depth.

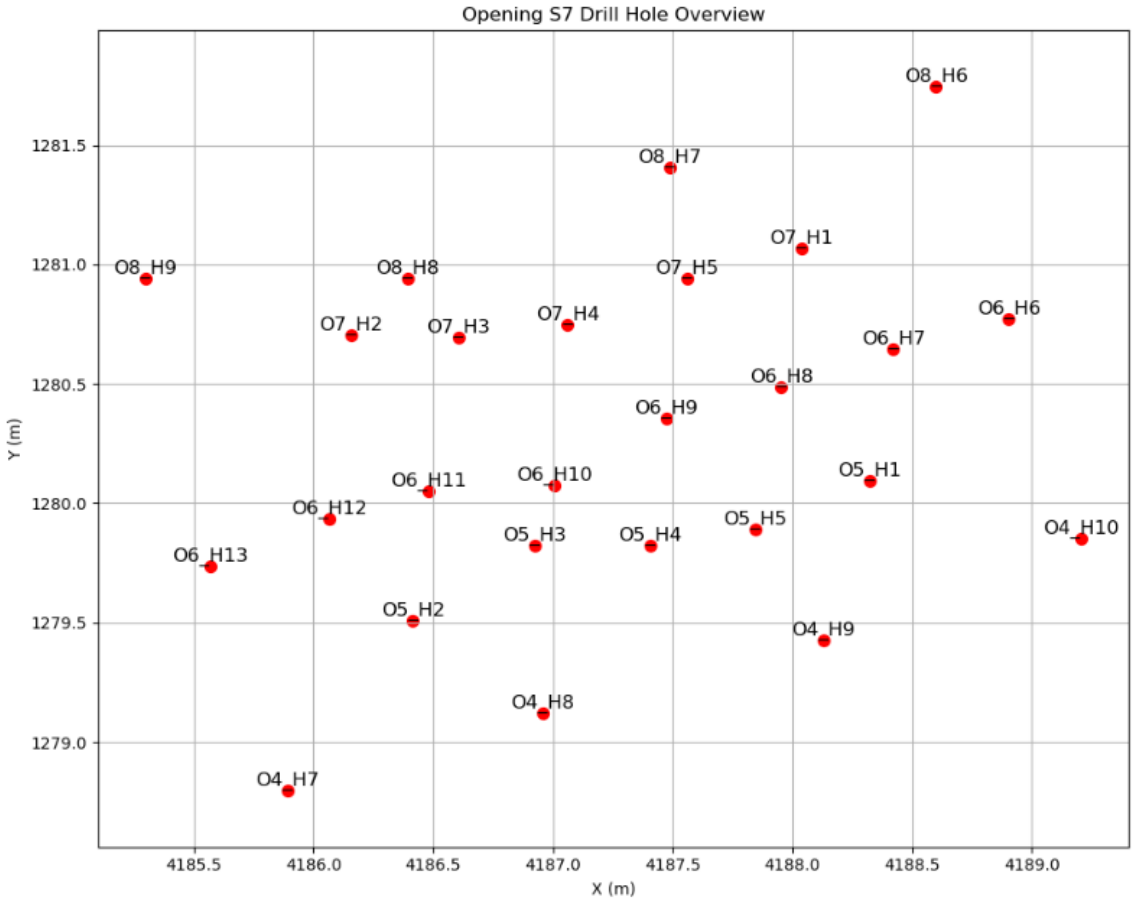

Figure 25: Overview of S7 opening drill holes.

Hole	Max Deviation Path Length (m)	Max MWD Depth Tag (m)
O4_H10	24.00	16.87
O6_H10	24.00	16.70
O6_H12	24.00	9.50
O6_H13	24.00	5.96
O8_H9	24.00	14.47

Table 8: Holes (Figure 25) where the recorded `DepthTag` from MWD data does not reach the end-of-hole distance.

4.3.2. Filtering and Pre-processing

The data processing workflow follows Navarro et al. (2021), with two extensions required to accommodate the Kankberg data set. Firstly, data entries showing drilling pauses exceeding 180 s were removed. These pauses were interpreted as full operational stops, such as drill bit exchanges or coffee breaks. Any value below this threshold was considered a potential rod addition event and was retained for filtering at a later stage. Secondly, the normalisation of the depth trend, originally applied only to the rotation pressure (RP) by Navarro et al. (2021), was extended in this study to multiple data types, including penetration rate (PR), percussive pressure (PP), and flush pressure (FLP), in order to better adapt the processing to the characteristics of the Kankberg data set.

Pause Removal

Pauses were identified using the time difference between consecutive rows within each drill hole. Rows following a pause could have been removed with a one-row buffer to eliminate transients introduced by slowdowns or restarts. However, because of the limited size and coarse resolution of the data set, this additional buffer was deemed unnecessary.

Outlier Removal

To remove implausible sensor spikes and recording errors, a two-sided percentile filter was applied individually to each MWD data channel. Following the approach in Navarro et al. (2021), which used a 99 % confidence interval on a larger data set, a slightly narrower 98 % window was used here due to the smaller sample size (26 holes instead of 302 holes). This threshold retained the main signal while suppressing the tails of the cumulative distribution functions.

Rod Addition Removal

Rod additions occur every 1.83 m and result in a temporary drilling stop. These events are consistently characterised by a penetration rate of $0\,\mathrm{m\,min^{-1}}$. All rows where PR = 0 were therefore removed. This approach mirrors the rod filtering strategy used by Navarro et al. (2021), however, here the entire row of data is discarded since it was not confirmed whether the recording of the other data was automatically stopped.

Depth-Trend Normalisation

Typically, systematic depth trends are caused by mechanical energy losses along the drill string, reduced flushing efficiency, bit wear, or friction from the blasthole walls (Navarro et al., 2021; Schunnesson, 1998). Navarro et al. (2021) applied this correction only to RP, as their other data did not show strong depth trends. However, inspection of the Kankberg dataset revealed depth-trend effects in several other sensors (PP, FLP, and PR). To correct for these biases, a second-order polynomial was fit to the average sensor signal per depth bin. A third-degree polynomial would have improved R^2 by a mere <0.5 % and was not adopted due to the disproportional risk of overfitting. The normalised value was computed by subtracting the depth-dependent trend and re-centering at the surface value as follows:

$$Data_{\mathrm{norm}}(z) = Data_{\mathrm{raw}}(z) - Data_{\mathrm{fit}}(z) + Data_{\mathrm{fit}}(0) \tag{4.15}$$

The feed pressure (FP) and damping pressure (DP) channels did not show a consistent trend with depth and were therefore left uncorrected. Figure 26 shows the trends of an arbitrary hole to visualise the decision for selective correction.

4.3.3. Structural Factor

The structural factor is based on the rolling variability of PR and RP, as these fluctuations have been found to correlate with fracturing and jointing (Navarro et al., 2021; Schunnesson, 1998). Therefore, the structural factor is constructed by the depth-normalised variability of the smoothed (rolling) PR and RP. Unlike Navarro et al. (2021), who did not normalise their PR because no clear trend was visible. For the Kankberg data, a trend was visible in the PR and was thus corrected for. The reason being that, in contrast to purely vertical holes, the downward angled orientation of the Kankberg slot reduces gravity-assisted drilling albeit slightly, especially as the inclination increases. The PR and RP residuals are calculated as follows:

$$\mathrm{PR}_{\mathrm{var},i} = \sum_{j=i}^{i+N} \left| \overline{\mathrm{PR}}_j - \mathrm{PR}_j \right|, \quad \text{with} \quad i = 1, 2, \ldots, L - N \tag{4.16}$$

$$\mathrm{RP}_{\mathrm{var},i} = \sum_{j=i}^{i+N} \left| \overline{\mathrm{RP}}_j - \mathrm{RP}_j \right|, \quad \text{with} \quad i = 1, 2, \ldots, L - N \tag{4.17}$$

Here, N is the size of the sample window, L is the total number of depth rows, $\overline{\text{PR}}$ and $\overline{\text{RP}}$ are the mean of the respective window. The outputs are the variances of the depth-normalised PR and RP respectively and are sub-sequentially used to construct the Discontinuity Index as such:

$$DI_i = \sqrt{\frac{1}{2}\left(\frac{PR_{\text{var},i} - \overline{\text{PR}_{\text{var}}}}{\sigma_{PR_{\text{var}}}}\right)^2 + \frac{1}{2}\left(\frac{RP_{\text{var},i} - \overline{\text{RP}_{\text{var}}}}{\sigma_{RP_{\text{var}}}}\right)^2} \quad i = 1, 2, \ldots, L \tag{4.18}$$

where $PR_{var,i}$ is the variance of an individual row, $\overline{PR_{var}}$ is the global mean variance, and $\sigma_{PR_{var}}$ is the standard deviation. RP is handled in a similar way. All variability traces $PR_{\text{var},z}$, $RP_{\text{var},z}$, the DI, and depth-normalised MWD factors were subsequently smoothed with a central 3-sample moving average and entered into a principal component analysis. The first principal component (PC_1) is referred to as the Structural Factor (SuF). To reduce the impact of noisy fluctuations in the SF and produce geologically meaningful and interpretable zones, a change-point segmentation algorithm was applied to the smoothed SuF signal. This approach, as introduced by Navarro et al. (2021), divides the factor profile of each drillhole into contiguous segments where the mean value remains relatively stable. This procedure uses the PELT algorithm (Killick et al., 2012). Here, segmentation minimises a cost function with the intent of balancing the internal variance within each block against the number of divisions. Each segmented block is then assigned a structural rock class (massive, fractured, or heavily fractured) based on the average SuF value of the block relative to fixed thresholds.

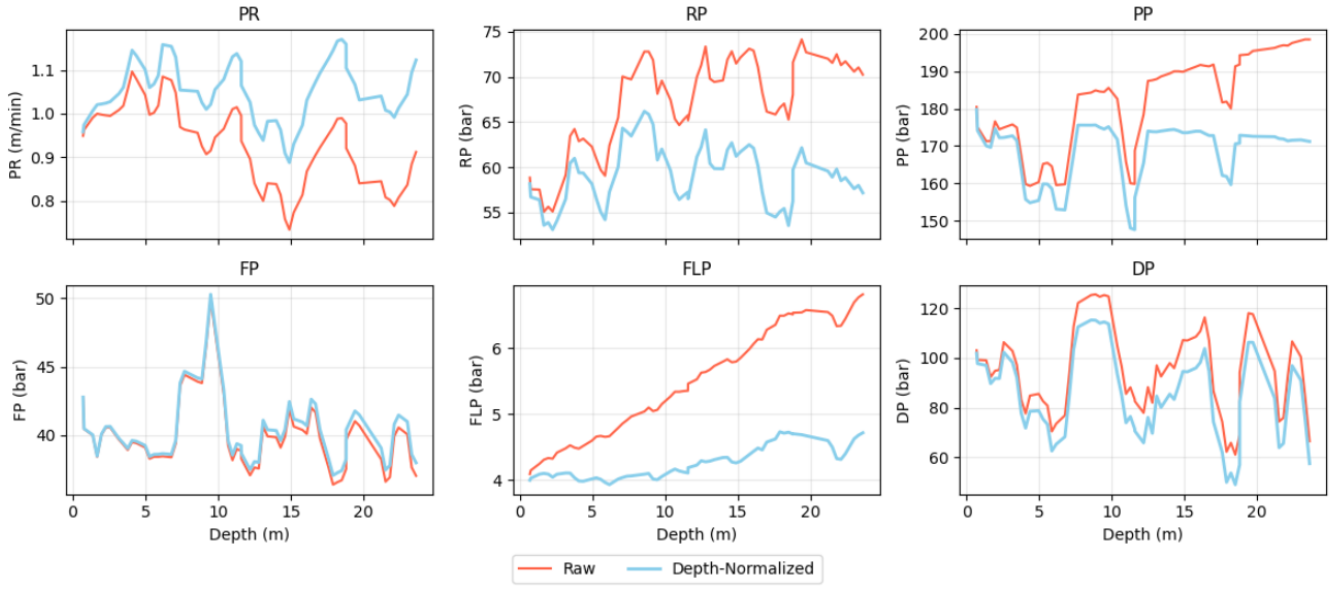

Figure 26: Depth-normalization of a random hole (O5_H5) from S7a_642, smoothed for better visual.

4.3.4. Strength Factor

Where the SuF aimed to find a metric from the variability of the MWD signal related to structures, the Strength Factor (SeF) objective is to quantify the drilling resistance of the rock. It therefore builds the SeF of the MWD signals itself, instead of its fluctuations. It is again derived using PCA on the smoothed data, this time using the input variables (where applicable depth-normalised) PR, FP, RP, PP, FLP, and DP. Here, PC_1 was the SeF.

4.3.5. Rock Factor

The Rock Factor (RF), as suggested by (Navarro et al., 2021), provides a unified proxy of the general behaviour of the rock by integrating the SuF and SeF. To ensure comparability, both factors were normalised by the z-score across each hole. The normalised factors were then combined using a PCA and, similar to the previous factors, the PC_1 was retained as the RF. As with the previous factors, the RF was also smoothed using a moving average. The resulting signal offers a holistic view of in situ rock conditions and can be used to segment the drillhole into geomechanically consistent zones.

4.3.6. Up-hole slot S0_612 cross-check

After finalising the S7 processing, the identical MWD workflow was applied to the available logs from the S0_612 opening slot to assess cross-stope outcomes. This dataset receives a minor role due to greater uncertainty. Firstly, no deviation measurements were available and the slot was drilled up-hole, and secondly, the raw logs showed a higher

incidence of concatenated files and other irregularities noted in Section 4.3.1. In general, large data gaps resulted in less data of likely lower quality than the S7 set. To retain comparability, the same preprocessing was retained as for S7, without re-tuning parameters for S0_612. Figure 27 shows that the depth-normalised trends of the S0_612 dataset were similar, except for the damping pressure, which showed a more pronounced depth trend. Furthermore, the PCA models were fitted separately on the S0_612 data.

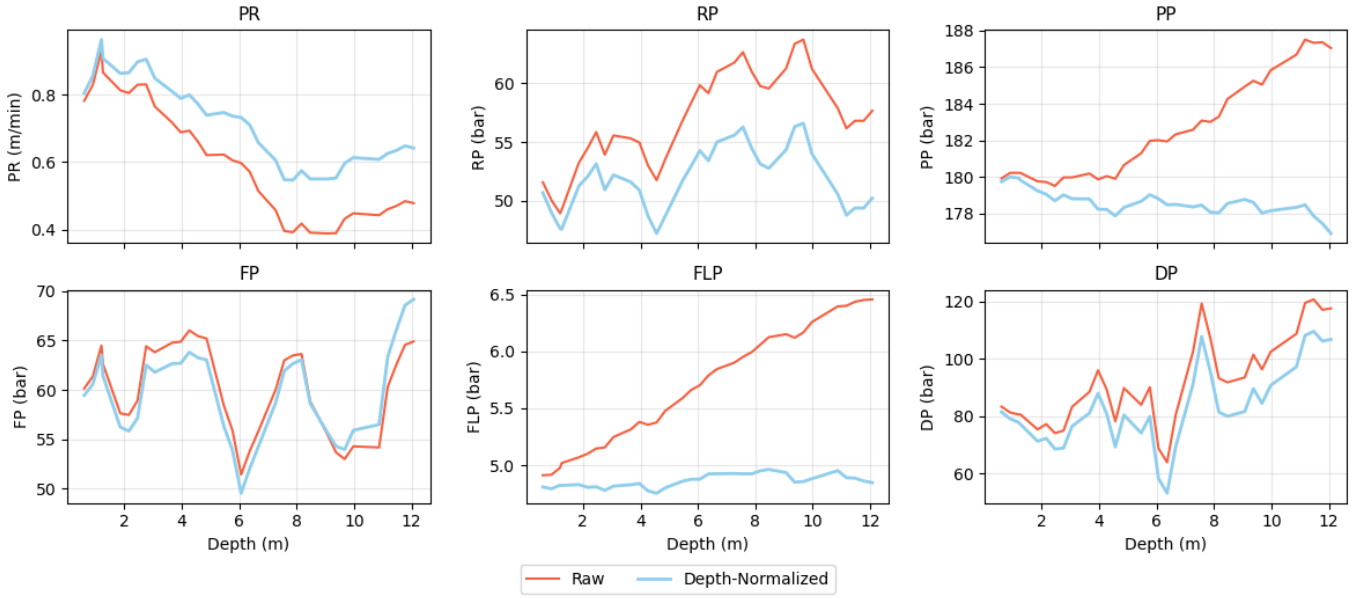

Figure 27: Depth-normalization of a random hole (O3_H8) from S0_612, smoothed for better visual.

5
Results

5.1. Index Variables

5.1.1. Geotechnical Logs

Geotechnical data from 73 diamond drillholes are summarised in Table 9, covering the six primary rock types intersected within the bounding box of the stoping area. BRQD and RMR values are reported as mean ± standard deviation, while joint surface characteristics and spacing are presented as categorical percentages of occurrence. The standard deviations for BRQD and RMR are notably high across all units, indicating a high level of internal variability in rock quality. ANDAQTZE and VOLCCL display the highest average BRQD (82% and 79%) and RMR (both 72), indicating generally more competent ground conditions. BREC and QTZFSPPO also show high values, though with greater variability. In contrast, AND and SERQTZE have lower BRQD and RMR values, suggesting lower rock quality. Joint roughness is predominantly 'slightly rough/discoloured' across all units, though AND and SERQTZE show higher proportions of slickened-sided or altered surfaces. Joint fill is minimal in most cases and most fall into the 0-1 mm category. The joint spacing is primarily 'close' (5-20 cm), but ANDAQTZE, VOLCCL, and QTZFSPPO show higher proportions of 'wide' spacing (60-200 cm), while AND has the most frequent occurrence of 'very close' joints (< 5 cm). Rock types with lower BRQD, such as AND and SERQTZE, tend to show more joint alteration, higher infill, and closer spacing, indicating a positive correlation between reduced rock quality and increased structural degradation.

Geotechnical data were also spatially analysed to observe whether significant trends existed in the X, Y, or Z direction. However, no significant spatial trends were observed in the drillhole logs. The logged data successfully highlighted the presence of the known fault at the edge of the stoping area by means of decreased BRQD values. For further analysis, it was assumed that these localised values did not have a significant impact on the overall blastability index.

Table 9: Summary of geotechnical parameters by rock type within the stoping area, where N represents sample size.

Parameter	AND	ANDAQTZE	BREC	QTZFSPPO	SERQTZE	VOLCCL
RQD						
BRQD [%]	53 ± 33	82 ± 18	70 ± 27	76 ± 23	65 ± 31	79 ± 20
RQD [%]	61 ± 36	88 ± 17	77 ± 29	83 ± 23	72 ± 33	86 ± 20
N BRQD	68	285	373	649	465	287
RMR						
RMR [-]	57 ± 14	72 ± 11	69 ± 11	71 ± 11	62 ± 16	72 ± 12
N RMR	68	285	373	636	443	287
Joint Roughness Occurrence						
Rough	5.9%	8.4%	9.4%	8.8%	5.4%	10.5%
Slightly rough/discoloured	42.6%	65.6%	84.5%	76.1%	52.0%	63.8%
Slickensided/biotitic/chloritic/altered	39.7%	18.9%	4.3%	12.2%	28.8%	20.2%
Slickensided/slippery/talcic/altered	11.8%	6.7%	1.9%	2.8%	12.0%	5.2%
Gouge/clay/strongly altered	0.0%	0.4%	0.0%	0.2%	1.7%	0.3%
N JointType	68	285	373	649	465	287
Joint Fill Occurrence						
0 mm	5.9%	8.4%	10.2%	8.9%	2.8%	11.1%
0–1 mm	85.3%	89.5%	86.9%	88.4%	87.1%	85.7%
1–5 mm	8.8%	1.8%	1.6%	2.2%	7.8%	2.8%
5–100 mm	0.0%	0.4%	1.1%	0.3%	2.4%	0.3%
>100 mm	0.0%	0.0%	0.3%	0.2%	0.0%	0.0%
N JointFill	68	285	373	649	464	287
Joint Spacing Occurrence						
Very Close (< 5 cm)	30.9%	3.5%	12.3%	5.8%	14.9%	4.9%
Close (5–20 cm)	57.4%	49.5%	66.2%	56.4%	57.1%	42.9%
Moderate (20–60 cm)	0.0%	0.0%	0.0%	0.0%	0.0%	0.0%
Wide (60–200 cm)	11.8%	46.7%	21.4%	37.3%	28.0%	50.5%
Very Wide (> 200 cm)	0.0%	0.4%	0.0%	0.5%	0.0%	1.7%
N JointSpacing	68	285	373	636	443	287

5.1.2. Joint Orientation

As noted in Section 4.1.2, limited free faces were available for direct joint orientation analysis. To reinforce the assumption that the dominant joint alignment aligns with the principal stress direction, a natural break observed in Stope S7a was evaluated. Figure 30 presents the stope scan, the interpreted discs, and the resulting stereonet. The discs were generated using GEM4D by fitting planes through three-point selections. The orientations from the overbreak region on the hanging wall were considered representative of natural jointing, not induced by blasting. A total of 18 randomly selected discs were analysed, producing a stereonet with a well-defined WSW–ENE striking set, characterised by steep dips. This trend is consistent with the inferred principal stress orientation reported in regional studies and supports structural interpretation. The minor dispersion in the pole orientation suggests the presence of a secondary joint set, which is also visible in the discs and Figure 15c. These joints are much shorter than the dominant set and roughly oriented perpendicular to the free face, which could mean that these were blast-induced.

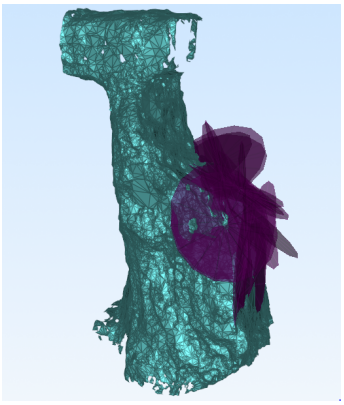

Figure 28: S7 stope scan and created discs

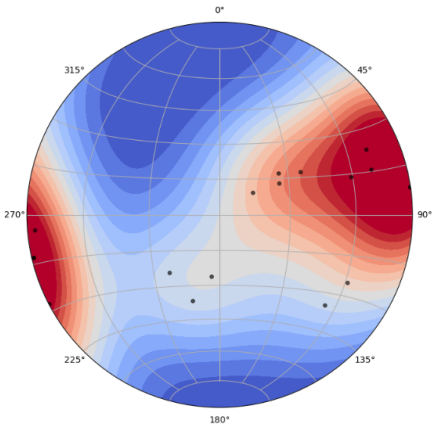

Figure 29: S7a stereonet including poles of individual discs

Figure 30: Orientation analysis of S7 overbreak

5.1.3. Laboratory Test

Machine Calibration

Corrections for machine compliance were applied as described in Section 4.1.3. The true elastic domain was identified to begin at approximately 40 MPa, where the stress-strain response becomes linear. Figure 31 shows the Young's modulus fitted from the calibration tests, alongside the apparent E values. As expected, the results confirm that a greater amount of support steel between the LVDTs and the rock specimen increases the required correction factor. For example, Setup 0, where the LVDTs were most separated from the sample by support steel, shows a difference in measured Young's modulus of nearly 40 GPa. In contrast, Setup 2, which had the least support interference, shows a difference of less than 10 GPa compared to the elastic modulus of the pure aluminium reference sample.

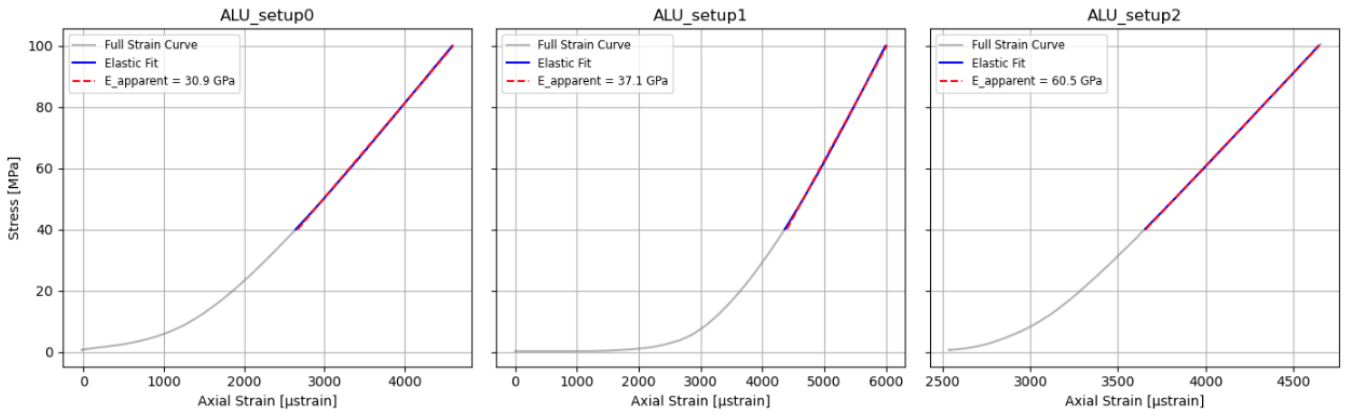

Figure 31: Machine calibration test with aluminium sample.

Unconfined Compressive Strength Test
Here the UCS results are discussed per rock type, this includes the type of failure and the overall behaviour of the rock type. Photographs of the broken specimen were taken and can be found in Appendix B.

Sericite Quartzite
The sericite quartzite samples (SERQ, Figure 33) demonstrate brittle mechanical behaviour, with UCS ranging from 65 to 129 MPa. Stress-strain responses vary: samples like `SERQ6015_6025` and `SERQ6755_677` show slightly more strain, likely due to extended seating before elastic loading. All specimens exhibit a clear peak followed by a rapid drop in stress, indicative of brittle failure. The samples were noted to be competent with some texture, suggesting moderate grain interlocking or foliation. The stiffness is relatively consistent and moderate, with low Poisson's ratios reflecting limited lateral expansion. Radial strain remains low during loading and increases sharply near failure, which is a typical brittle signature. Most samples failed by shearing along a single plane, more or less aligned with foliation, especially in `SERQ6365_6380`. `SERQ6015_6125` was an exception, failing due to a mix of double shearing and axial splitting and being the only sample that did not break catastrophically. This could suggest that while failure was generally structurally guided, pre-existing fractures or other local heterogeneities can locally alter the mode of failure.

Andesite
The andesite samples (AND, Figure 34) show a much wider range, with UCS values between 88 and 354 MPa. Elastic behaviour is much more variable between samples, with moderate to high stiffness. Samples `AND1353_1354` and `AND6875_689` reached the highest strengths and failed explosively, reflecting high internal energy storage and brittle release. Both were mineralised and competent; therefore, one could argue that the failure was structurally driven along the planes of weakness near the mineralised zones. `AND136_13615` and `AND1201_1201` failed along single shear planes, although the latter's failure mode closely resembled a large spalling event. `AND131_13115` showed multi-plane shear, consistent with its pre-existing fractures. While `AND600_6015`, fractured in multiple directions but remained intact, probably due to lower peak stress. Radial strain across samples increases sharply near the peak, aligning with brittle failure. Despite variable peak strength, the failure modes in all samples were abrupt and structurally controlled, with mineralisation and existing fractures strongly influencing fracture geometry and severity.

Volcaniclastic
The volcaniclastic samples (VOLCL, Figure 35) show UCS values between 68 and 143 MPa, with variable elastic moduli and low Poisson's ratios. All samples are mineralised and competent, with varying degrees of texture and fracturing. `VOLCL843_844` failed cleanly along a single shear plane, while `VOLCL9315_933` underwent multiple severe spalling events prior to a final shear failure, which could be explained by its reported fracturing and mineralisation. These events inhibited finding a clear linear elastic domain and, therefore, it is left out of the summary table. `VOLCL1023_10245` and `VOLCL1277_12785` failed by axial splitting and some minor spalling during loading. `VOLCL7445_746` failed by a combination of axial splitting and shearing, although the elastic curve appears artificially steep, best explained by an error arising from the LVDT setup. Differences in failure geometry and post-peak behaviour indicate that volcaniclastic is hard to predict, which aligns with the expectation of the rock type, since volcaniclastic is generally seen as a rock type consisting of multiple minor rock types. At first glance, it appears that textural and structural variations, such as foliation, spalling, and pre-existing defects, are a major control to how brittle failure manifests in this group.

Andalusite Quartzite
The andalusite quartzite samples (ANQTZ, Figure 36) show varied UCS values between 48 and 369 MPa, with high elastic moduli and low to moderate Poisson's ratios, again indicating strong and competent rock. All samples were mineralised and structurally intact prior to testing, although the failure modes vary. `ANQTZ13185_132` broke along a pre-existing fracture with a clean shear plane, which explains its lower UCS. `ANQTZ1831_1833` and `ANQTZ22195_2221` experienced axial splitting and end-to-end spalling, typical of quartz-rich rocks under high stress, but with ambiguous final failure surfaces (Jaeger et al., 2007; Paterson & Wong, 2005). `ANQTZ224_22415` showed a similar failure pattern, though it reached the highest UCS of the group, it remains unclear whether this reflects a true UCS failure or is affected by progressive end-to-end spalling. `ANQTZ1084_1085` developed small, erratic fractures and likely underwent axial splitting, although no full separation occurred. Post-peak stress drops are present but more gradual in some samples, particularly those that did not fully fracture, suggesting that energy was dissipated through internal cracking and spalling. In general, the rock type behaves as strong and brittle rock, but variable failure geometries and incomplete breaks in some specimens reflect how some failure events, such as spalling, could mask the actual UCS failure.

Breccia
The breccia samples (BREC, Figure 37) exhibit UCS values from 95 to 419 MPa. `BREC15705_15715` shows a steep linear increase in stress followed by a relatively gradual post-peak decline, consistent with axial splitting at a lithologic boundary and significant spalling, expected behaviour of a layered breccia. In contrast, `BREC935_9365` shows a

near-linear elastic response followed by a sharp, catastrophic stress drop with minimal post-peak strain, aligned with its explosive failure and highest UCS in the group. `BREC7655_767` and `BREC2133_21345` both show well-defined elastic regions and abrupt drops, though the former suggests more energy absorption prior to failure due to the high number of fractures resulting in double shear/axial split mode. `BREC19345_1936` has a relatively muted peak and continues to deform after partial stress drop, suggesting a more progressive, non-catastrophic failure, likely due to high internal texture, which can be confirmed by prior observation of the sample. `BREC1947_19485` presents a comparatively low UCS and lower stiffness, this can be explained by the fully cross-cutting fracture present in the sample suggesting initial slip and failure along the existing shear fracture due to crack propagation. Most samples show radial dilation near failure and display brittle to quasi-brittle characteristics. Despite heterogeneities resulting in different UCS values, the degree of seating is relatively constant among the specimens.

Quartz Feldspar Porphyry

The QTZFP samples (Figure 38) show relatively consistent behaviour with UCS values ranging from 84 to 399 MPa and moderate stiffness. All samples show relatively gradual post-peak failure, indicating quasi-brittle failure. The failure modes were fairly consistent, `QTZFP17055_1707` had a clean double-plane shear failure. `QTZFP1764_17655` and `QTZFP178_17815` both exhibit low strength with broader peaks and more gradual post-peak behaviour, reflecting the notes on pre-existing full cross-cut fractures. The former did not fully break but showed extensive shear and axial cracking, while the latter failed primarily along the brecciated zones that ran through the core, consistent with the axial splitting seen in the specimen. `QTZFP186_18615` shows axial splitting and severe early spalling, with major post-peak deformation, matching its limited fracturing. `QTZFP9215_923` exhibits the highest UCS and showed continuous ejection of quartz chips during loading, which can also be seen in the radial strain values. This supports an interpretation of progressive spalling rather than a clean fracture event. Overall, the porphyry group is characterised by very strong, quasi-brittle behaviour with a consistent post-peak response depending on the degree of internal texture, brecciation, and fracture concentration. Similarly to the breccia specimen, initial seating was fairly constant.

Cross-Group Trends and Condition-Based Observations

Despite the limited dataset, a cross-comparison of all rock types reveals consistent trends between pre-failure sample descriptions and geomechanical performance. Figure 32 presents a hypothetical mechanical index calculated as the product of UCS and Young's modulus (E). Samples described as 'competent' show the highest UCS and stiffness within 3/5 rock groups, with the exception of the sericite quartzite and andesite group, where a more random distribution is observed. In contrast, specimens exhibiting pre-existing defects generally score lower on the index. In addition, a study of the correlations between UCS and stiffness suggests that competent samples show a strong positive relationship, while fractured or cross-cut specimens show no consistent trend. Due to the small sample size, the plots supporting the correlation analysis have been omitted. Although indicative patterns were observed, claiming statistical significance would be misleading. Furthermore, alterations are also shown in Figure 32. These do not show logical trends, since, for example, the alteration of topaz (T) should theoretically increase the strength of the rock. Thus, one may conclude that, assuming the alteration was logged correctly, the condition of the sample has a much greater influence on the rock's UCS and stiffness than the alteration level.

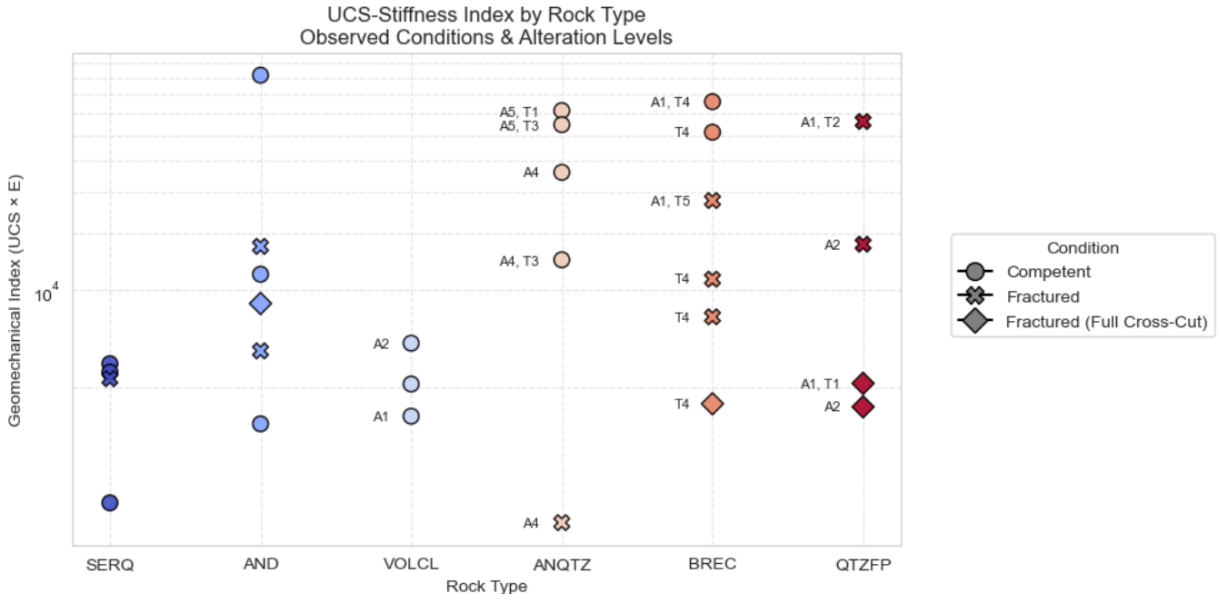

Figure 32: Specimen conditions and alteration versus geomechanical index (UCS x Stiffness).

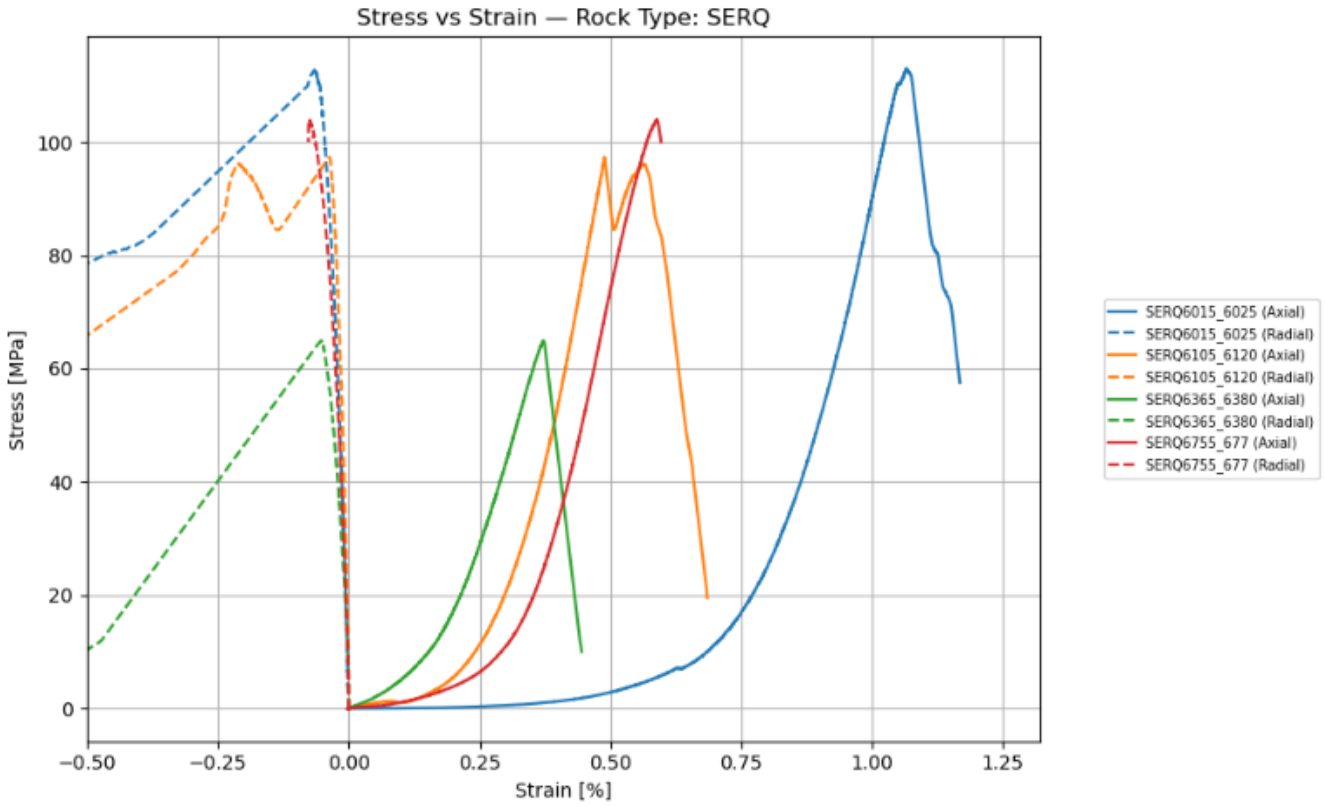

Figure 33: UCS stress-strain plot for Sericite Quartzite.

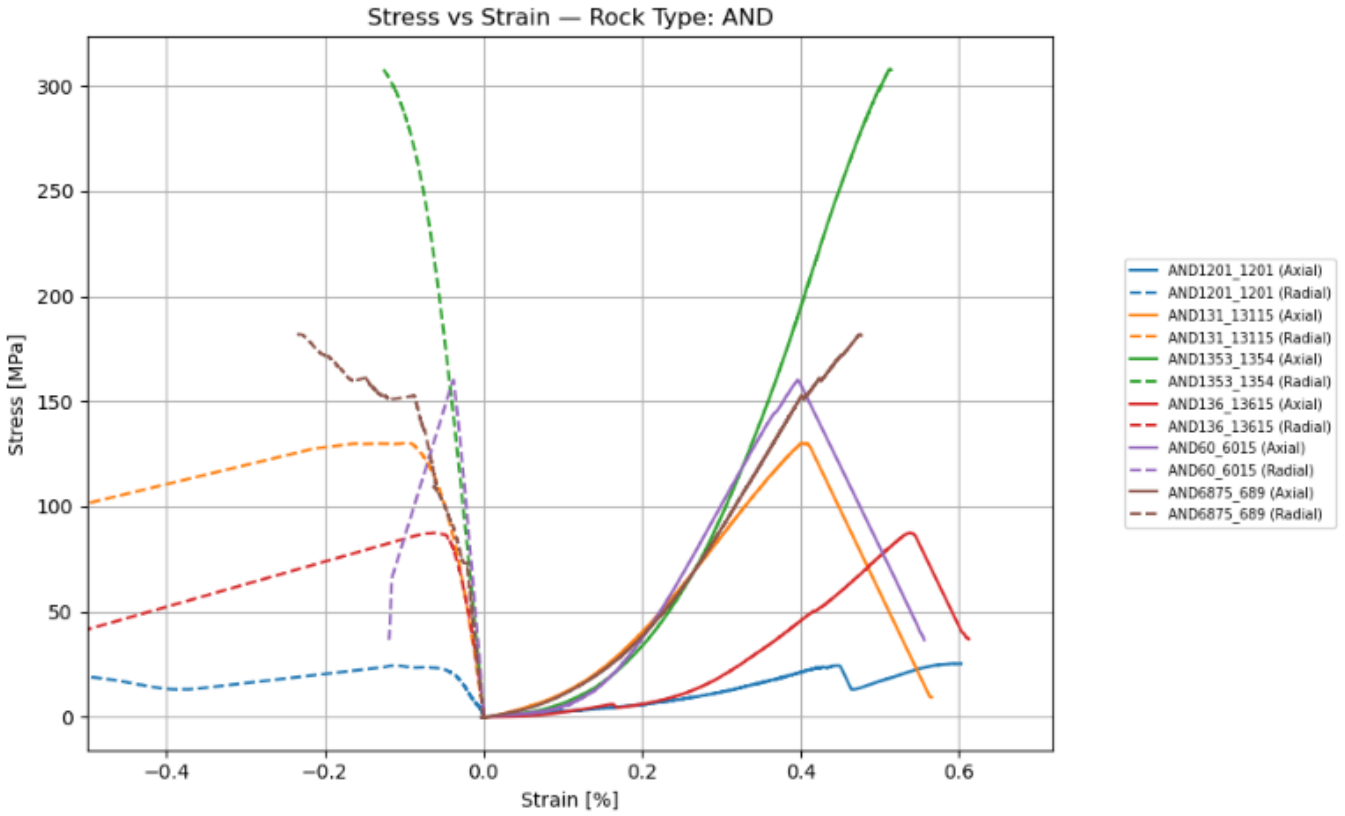

Figure 34: UCS stress-strain plot for Andesite.

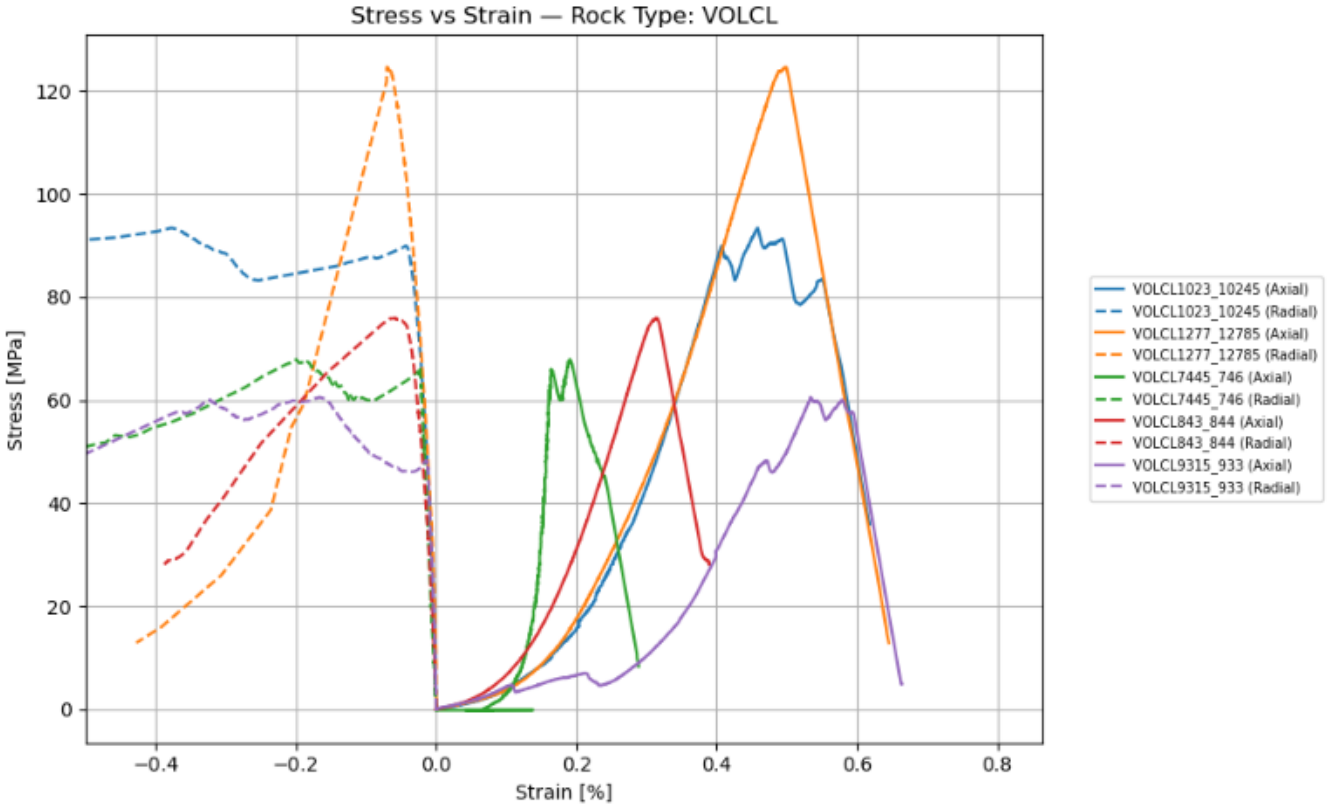

Figure 35: UCS stress-strain plot for Volcaniclastic.

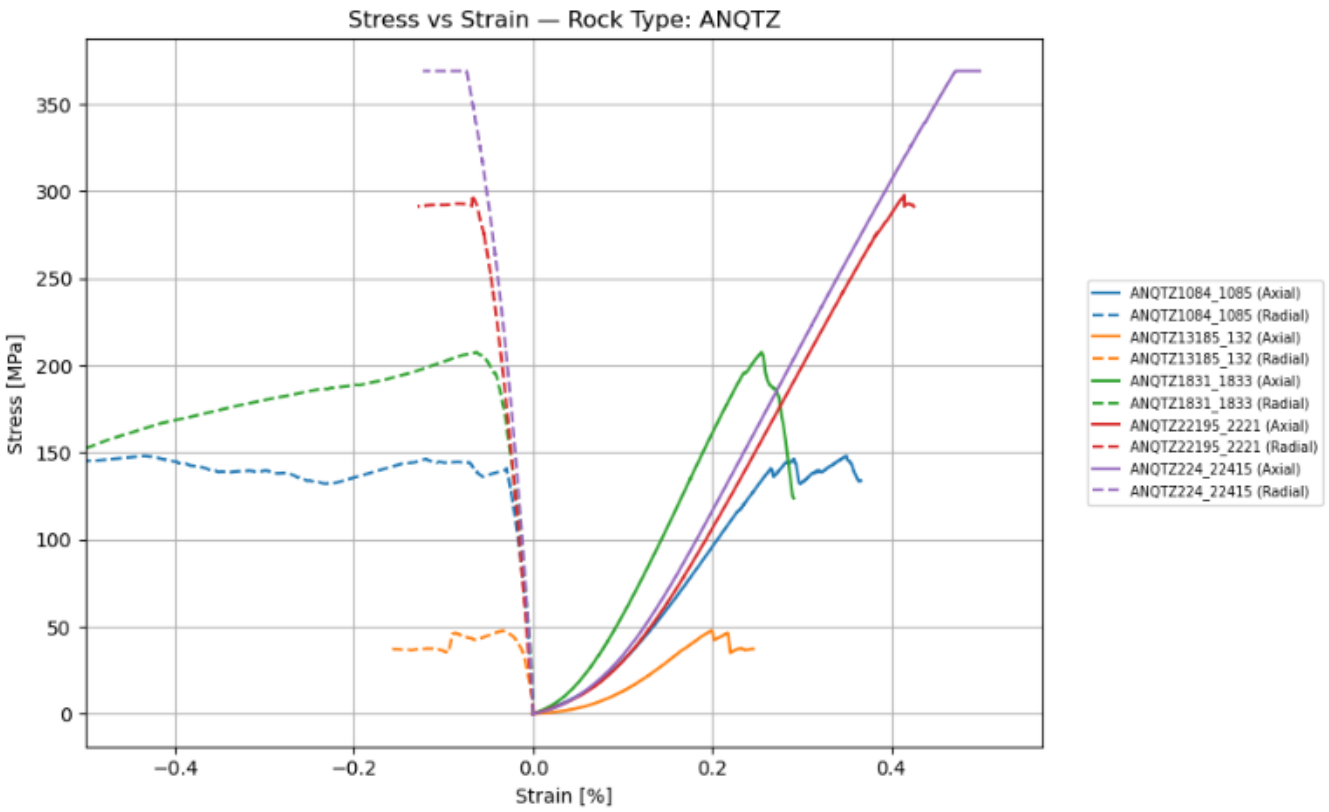

Figure 36: UCS stress-strain plot for Andalusite Quartzite.

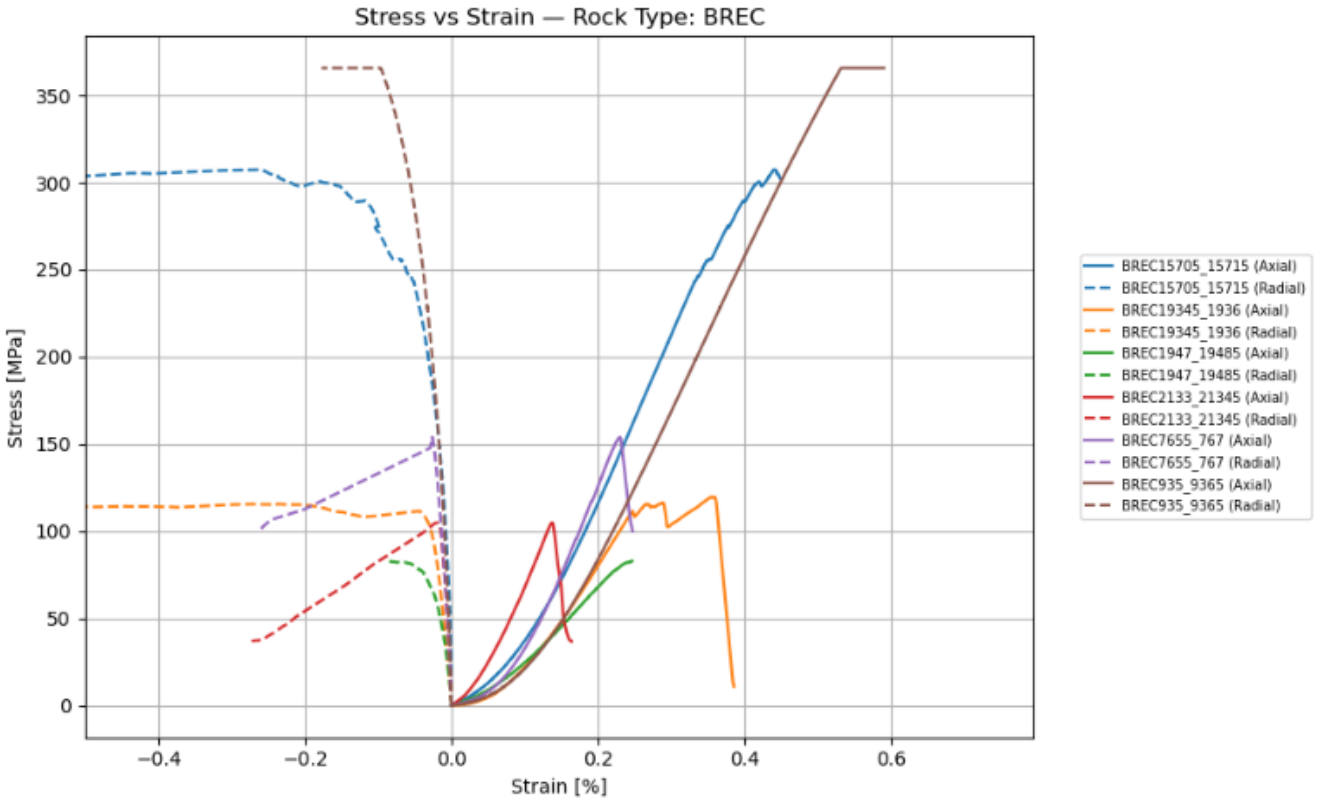

Figure 37: UCS stress-strain plot for Breccia.

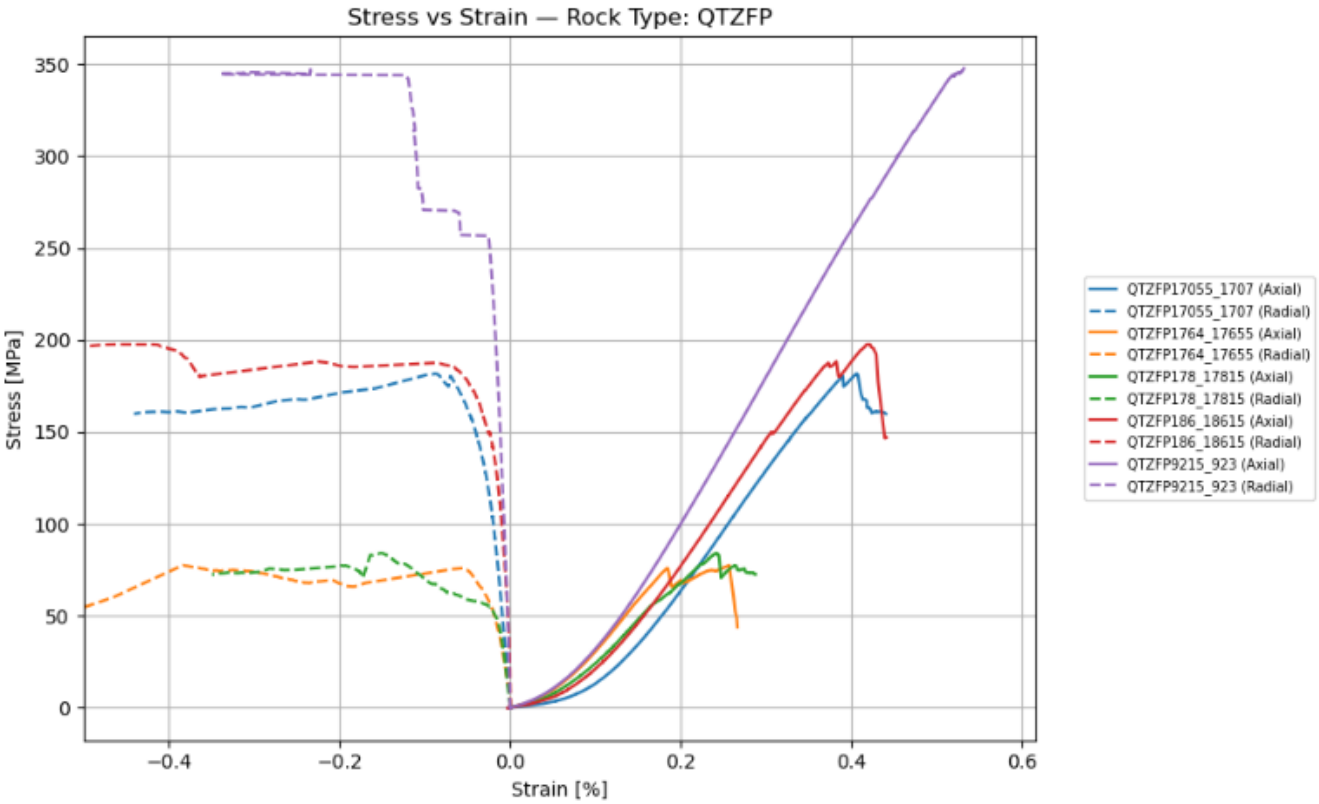

Figure 38: UCS stress-strain plot for Quartz Feldspar Porphyry.

5.2. Blastability Indices

5.2.1. BI and FBI output measures

The calculated index variables were used to generate both the BI and the FBI for the six most common rock types present within the stope (Table 10). The table shows the ranges and mean values of the calculated BI and FBI with an additional normalised column for easier comparison and interpretation. For the mean BI, it can be seen that andesite is generally classified as the rock type that is easiest to blast, followed by breccia, sericite quartzite, volcaniclastic, porphyry and finally andalusite quartzite, which emerges as the most difficult to blast.

Unlike the BI outcome, the mean FBI returns a slightly varied ranking. Andesite and sericite quartzite rank as the rock types that are easiest to blast, with breccia, volcaniclastic, porphyry, and andalusite quartzite once again being the most difficult. This indicates how the FIS, with varying ranges of inputs, groups some of the rock types into corresponding blastability rankings because of the properties of the MFs and the rule base.

In addition to the base results, Table 10 also includes a 'competent' version of the two indices (BI_{comp} and FBI_{comp}) calculated from only the UCS values of the most intact and least disturbed samples to calculate the rock hardness input, H. From Table 32 we can see that not all rock types tested had competent samples, in these cases the highest value was taken as the most competent sample of the rock type. The use of this competent subset is considered appropriate, as the RMD already captures the structural aspects of the rock. Therefore, competent samples should be used when calculating the H. However, the extremely limited sample size requires this method to be a trial instead of the main calculation. The BI values are unsurprisingly higher, as higher H values are fed into the BI calculation. However, the FBI mean values are lower or remain unchanged, with the exception of porphyry, where the competent subset showed an increase.

Table 10: Comparison of input variables, BI and FBI outputs, and their normalized scores across rock types.

Input Variables						*BI Outputs*			*FBI Outputs*			*Normalized (1-10)*			
Rock Type	RMD Range	JPS	JPO	RDI Range	H Range	**BI Range**	**BI Mean**	**BIcomp Mean**	**FBI Range**	**FBI Mean**	**FBIcomp Mean**	**BI**	**FBI**	**BIcomp**	**FBIcomp**
Andesite	20–50	15	25	20–25	4–18	42–67	51	55	30–70	50	50	1	1	1	2
Andalusite Quartzite	40–50	30	25	20–33	2–18	58–78	69	71	45–78	70	70	10	10	10	10
Breccia	20–50	15	25	20–37	5–21	42–74	58	62	30–70	54	54	4	3	5	4
Porphyry	30–50	30	25	16–18	4–20	53–71	65	70	30–67	57	60	8	4	9	6
Sericite Quartzite	20–50	30	25	18–21	3–6	48–66	59	60	30–58	50	47	4	1	3	1
Volcaniclastic	40–50	30	25	18–23	3–7	58–68	64	65	39–70	55	50	8	3	6	2

It can be argued that the competent mean FBI values seem non-sensical, as intuitively it does not make sense for the value of the index to remain unchanged or even decrease when input variables such as UCS increase. However, this phenomenon is an immediate result of the way MFs have been defined and used. In the competent case, the MFs were recalculated solely on the basis of the diminished set of competent UCS samples. This ensures that the fuzzy system evaluates the blastability in accordance with these more constrained conditions. However, because fuzzy logic relies on relative membership grades in the provided fuzzy sets, an absolute increase in input values does not always lead to a proportionally higher FBI score. Rather, the recalibrated membership functions redistribute the competent UCS values throughout the entire recalibrated range. This advantageously maintains the internal distinction within the competent range, but tightens the total spread compared to the original wider dataset. The most dramatic example is the porphyry rock type, where a single competent UCS entry populates the competent MF. Accordingly, when the input data range is limited to only competent samples, the FIS's ability to identify very subtle differences in rock competency can be impaired if MFs overlap too much at the high end of the scale, like in the porphyry case. Overlapping reduces the strength of related fuzzy rules and can lower defuzzified FBI scores.

However, application of the competent subset still provides useful contrast for certain rock types with clearly more pronounced intact strength characteristics, such as breccia and porphyry, which show a more distinct contrast in their index values in the BI_{comp} and FBI_{comp} tests. This indicates that the indices can be used flexibly to provide a more adequate representation of expected in situ rock mass conditions, or increase contrast between rock types. In short, the results highlight that while the BI responds as expected to increased input values, the FBI must pay sharp focus to the definition and adjustment of MFs whenever the input data range changes. This is crucial to be able to produce significant differences between the indices and maintain them as valid.

On another note, it is observed that the ranges of different input parameters, especially RMD, RDI, and H, are still relatively wide. This is mainly due to the intrinsic variability of geotechnical parameters, such as the large standard deviation of BRQD values, the lower number of density and UCS test data and inherent natural rock mass heterogeneity. Consequently, there is a tendency for the mean input values of some variables to cluster around an inner value, potentially reducing the degree of contrast that would otherwise be present in the resulting indices. For example, the range of RMD of andesite is 20 to 50, indicating that high competency and high fracturing andesite were noted in the geotechnical logs. Although such data may be partially lost when only the mean BI or FBI is used, it is still visible when observing the ranges of indices.

Lastly, indices must somehow explicitly contribute to facilitate the decision process for the D&B method. It is therefore essential that they are able to capture and express significant blastability differences without overstatement of differences created from uncertainty or lack of data. This can be done by being careful with what input variables are brought into play and by adjusting the relative weights of each input according to the confidence in their accuracy. For example, as indicated in Section 4.1.2, it is assumed that the JPO value is the same for all types of rock because it is derived from a single natural fracture orientation and the principal stress directions. Furthermore, in reality, JPO should include the adopted slot position within the stope, which depends further on practical considerations such as the accessibility of the jumbo drill, safety, and the shape of the stope. In addition, indices like these do not account for the influences of localised anomalies such as faults or water-bearing fractures. In spite of these constraints, the outcomes confirm that judicious selection and weighting of input parameters have the potential to supplement the ability of both the BI and the FBI to formulate more efficient contrast of blastability conditions in the stopes. The subsequent sections elaborate further on the practical relevance of these observations and detail how the indices can be used to improve the usability of the indices.

5.2.2. Sensitivity Analysis and Model Comparison

To assess performance of the BI and FBI it is critical to assess the sensitivity to input changes and how flexible it is under varying conditions. Additionally, comparing how the BI and FBI models compare when subjected to changing variables will help to establish an understanding of whether the use of a more mathematically and computationally complex system is worthwhile in a practical decision-making perspective.

Weight-based

The Lilly BI index has a certain arrangement of weights, which favours the structural condition of the rock mass over its density and hardness. The FBI, despite building upon Lilly's BI, does not. Fine-tuning weights to find site-specific requirements is even encouraged (Azimi et al., 2010). In order to achieve this, a variety of weight-sets was created as such:

$$\text{Weight Sets (RMD, JPS, JPO, RDI, H)} = \begin{cases} \text{Equal} & : [1,1,1,1,1] \\ \text{H\_high} & : [1,1,1,1,3] \\ \text{RDI\_high} & : [1,1,1,3,1] \\ \text{Structure\_high} & : [2,2,2,1,1] \\ \text{JPO\_zero} & : [1,1,0,1,1] \end{cases}$$

resulting in FBI results per rock type that show their sensitivity to weight changes (Figure 39).

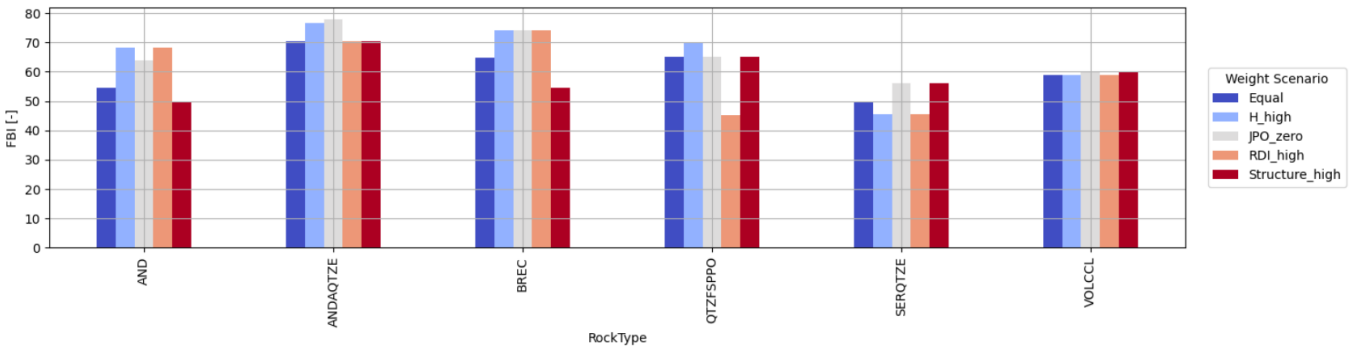

Figure 39: Weight-based Sensitivity Tested FBI Results.

All rock types exhibit variability of FBI scores across the different weighting scenarios, confirming context-dependent blastability. Prioritising hardness generally increases FBI for all rocks except sericite quartzite. Increasing the influence

of density creates a variable response from the different rock types, which may indicate that some rock type density data are more stable than others. Removal of the JPO factor has another effect, which tends to increase FBI values in all lithologies. Stable rock types such as volcaniclastic vary minimally between scenarios and display consistent blast performance, while other rock types like porphyry and andalusite quartzite are extremely sensitive to weighting choices. All this variability shows the importance of aligning blastability models with the locally dominant conditions in each stope. Assigning wrong weights to inputs could lead to over- or underestimation of blast performance, especially in the more sensitive lithologies. However, stable materials might yield more predictable blast outcomes.

Morris Method

Another method of sensitivity analysis is the Morris method, this statistical screening tool that aids in identifying the influence of single variables in the system. Each input variable is iterated over its full theoretical range as defined by the scoring tables or membership functions, while keeping the others stationary. In doing so, metrics on the importance of the variables ($\mu*$) and their nonlinearity or interactions with other variables (σ) can be compared. This method therefore can therefore give quick insight into the most influential inputs. Analysis was performed on both models as can be seen in the following. One should be aware that the nature of the method is stochastic. In other words, numerical differences may appear in $\mu*$ and σ on different runs. However, the relative ranking should and does remain stable.

Table 11: Morris Sensitivity Results for the FBI and BI Models.

Parameter	FBI		BI	
	μ^*	σ	μ^*	σ
RMD	20.10	7.85	20.00	0.003
JPS	20.40	7.51	20.00	0.003
JPO	20.40	6.18	15.00	≈0
RDI	19.20	8.25	10.32	≈0
H	20.40	6.81	9.28	0.003

Table 11 captures the behaviour of the models. For BI, one can now clearly see that input dominance is fully dictated via fixed scoring, as expected. This shows that the model its code is performing as designed. The small interactions and non-linear behaviour seen in the BI results stem from numerical precision limits of the Morris method and should be interpreted as insignificant noise. In contrast, the FBI shows more equal influence distributions and interactions through fuzzy rules. The FIS flattens the sharp differences between variables, reflecting the purpose of the model. This also demonstrates the intended design. It makes a direct one-to-one comparison difficult, yet shows the inherent purpose of both models. The BI was built to follow Lilly's reasoning and expertise to follow the relative weight of variables. However, the FBI aimed at blurring the lines of sharp boundaries and tailoring them to be applicable for the Kankberg site by allowing higher levels of contrast.

Overall Model Comparison

Finally, one can compare the overall outcome of the two models and scenarios per rock type. Figure 40 shows three entries in the two radar plots, one being the BI and the other two being the FBI results. The plot on the left shows the standard UCS handling, and the competent scenario shows the results if only the competent samples are retained. Looking at the standard scenario, one can observe a shape mismatch between the BI and the FBI with equal weights. Unsurprising due to weighting differences that the original FBI inherently has compared to the BI. Therefore, an additional weighted FBI run was performed with roughly the same weighting as Lilly's BI. Table 11 was used to derive new weights for the 5 input variables, respectively [2, 2, 1.5, 1, 1]. The similarity in shape of this run with the BI shows that weighting is the dominant factor between the models' shape differences. The BI shows relatively worse blastability scores than the FBI model, because its sharp scoring transitions force it to be more conservative. The FBI, on the other hand, shows higher levels of smoothing; one extreme value is not enough to push the entire blastability assessment to be more conservative. This is reflected in their size differences. The other radar plot, the competent scenario, shows much more erratic values. As discussed previously, this unstable behaviour and lack of harmony between BI_{comp} and FBI_{comp} (Lilly weights) is a result of the changed MFs and the lack of data to build these new ranges.

All in all, one can observe that the equal-weighted or the Lilly-weighted fuzzy index illustrates how expert judgment about dominant rock mass controls, in this case the relative importance of structural versus mechanical properties, can significantly influence blastability predictions. This underlines the adaptability of the fuzzy system and highlights the importance of proper site calibration of both the FIS weights and the addition of expert knowledge in the form of new fuzzy rules.

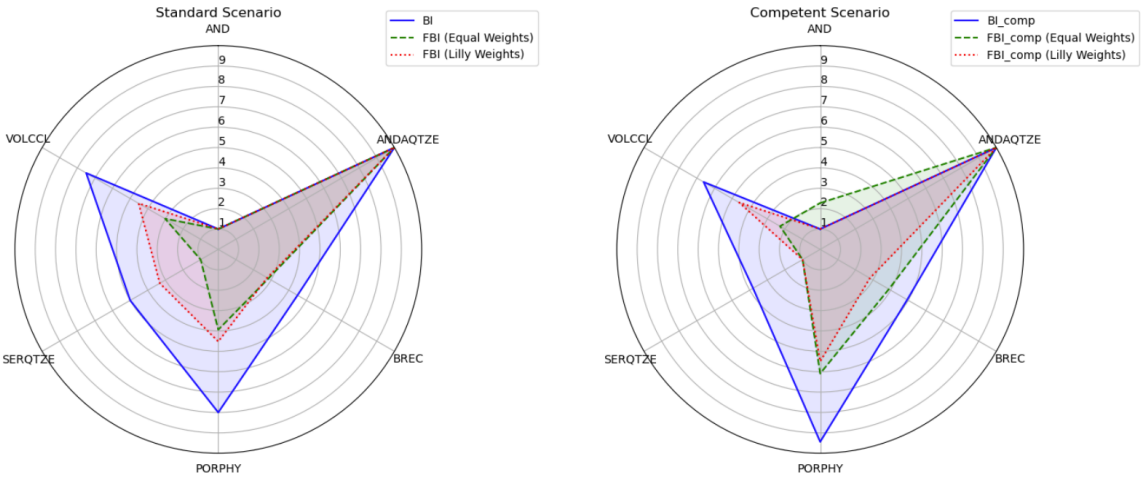

Figure 40: BI and FBI radar plots (normalised).

5.3. Measure While Drilling Rock Index

5.3.1. Processing Pipeline

The 26 drill holes in the S7_a opening slot were processed using the methodology inspired by Navarro et al. (2021), with additional adaptation for time-based filtering and additional depth normalisation due to site-specific observations. This has been thoroughly discussed in the methodology section; however, here some figures will highlight the processing steps. With the exception of depth normalisation, which was previously shown in Figure 26.

The initial data contained 1993 rows of unique observation points. The initial removal of the pauses longer than three minutes resulted in the additional removal of 16 rows. Removal of rod additions contained the most severe filtering, where 358 unique rows were discarded. Figure 41 shows the removal of the rod, leaving a much cleaner and more realistic data set. Finally, outliers were removed from the set, resulting in the removal of an additional 182 rows due to the removal of 2% of the most distant data.

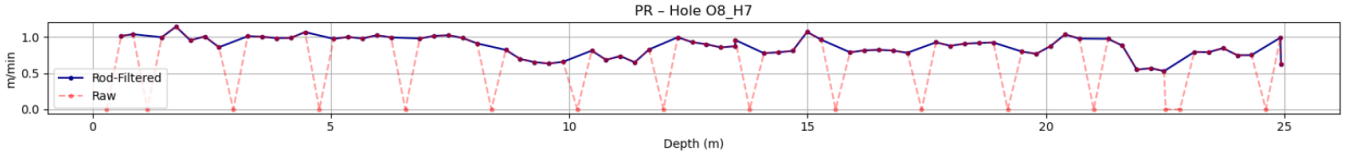

Figure 41: Raw and processed penetration rate of an arbitrary hole.

5.3.2. Factor Trends and Cross-hole Consistency

Following the processing pipeline, structural and strength factors could be calculated based on the results of the PCA analysis. In every hole, one or both factors exhibit expected fluctuations with depth. Although some spatially adjacent holes are in good agreement with each other, such as the holes shown in Figure 42. In contrast, one can also observe the contrary, as shown in Figure 43. It must be considered that these figures depict smoothed signals, where a rolling window of five samples is used to denoise the logs as much as possible for ease of interpretation. In reality, these factors sometimes interpolate between gaps of a metre wide to account for all the removed data that were removed whilst filtering. Due to interpretation being extremely difficult for disconnected strength factors, it was opted to connect them either way. However, this also introduces extra levels of potential error. Additionally, despite the argument that long-term changes in the SuF, SeF and RF may indicate different geologic units. It can also be a signal from mechanical grounds. Unaccounted for drill bit deterioration could be the perpetrator if the SeF tends to creep upward with depth.

Figure 42 shows overall well-structured data that behave relatively stable across different holes. High peaks in the SuF predicatively coincide with lows in the SeF. Structurally massive rocks often exhibit higher strength values, as observed in the UCS test results. Based on the holes O7_H3, O7_H4 and O7_H5 one could argue that the MWD is truly capturing geological features. However, other drill holes suggest the opposite. Figure 43 is an example of how some spatially adjacent holes showed inconsistent and geologically unconvincing trends. For example, holes O6_H8 and O6_H9 show vastly different behaviours, with comparatively stable rock factors along the extent of the holes. It is unlikely, but not impossible, that the behaviour of the rock mass will change over such short lateral distances. Another plausible

explanation is the disturbance of the geologic signal by mechanical noise. Despite a signal being present, it is almost completely filtered out by a stronger non-geologic signal. Without ground-truth data, there is no method to confirm or disprove these suspicions. It therefore illustrates the expected and inherent difficulties of handling coarse MWD data.

To study the cross-hole consistency of the data, one had to compare the adjacent drill holes with respect to every hole. Appendix D containing Figure 54 shows the three derived factors: SuF, SeF and RF for the S7 and S0 openings. One can observe the drill hole correspondences or disagreements. In order to create these figures and conduct a proper analysis, the author ensured a valid comparison between the holes. To evaluate spatial consistency in SuF, SeF and RF, the author computed pairwise comparisons between each drillhole and its five nearest neighbours based on lateral collar position. For the continuous variables (SuF and SeF), the Pearson correlation coefficients were calculated by interpolating each pair's values over their overlapping depth interval. For the categorical RF, the fraction of exact string matches between nearest-neighbour interpolated profiles along the same depth range were computed.

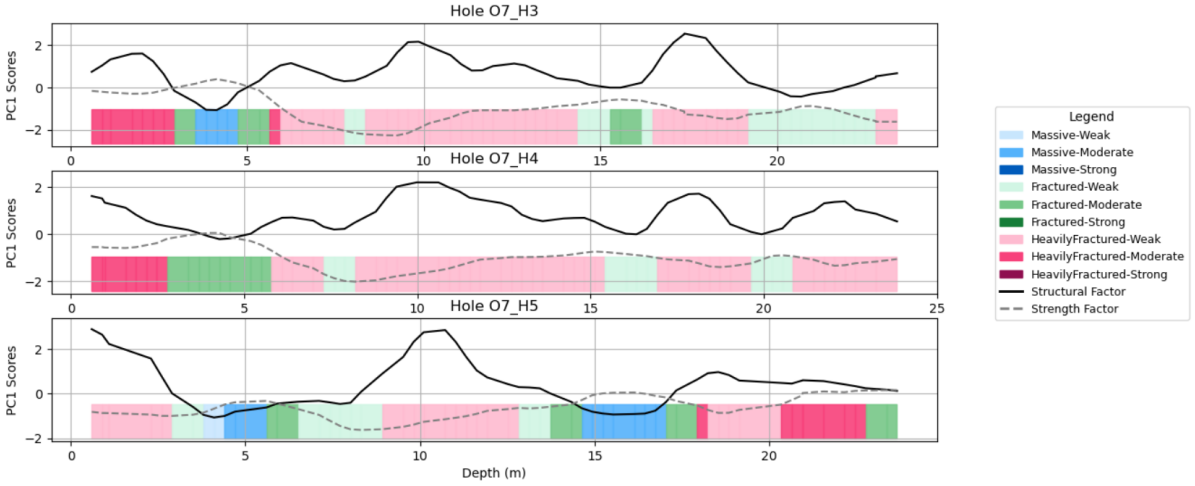

Figure 42: Three adjacent holes that show similar trends for their structural, strength and rock factors.

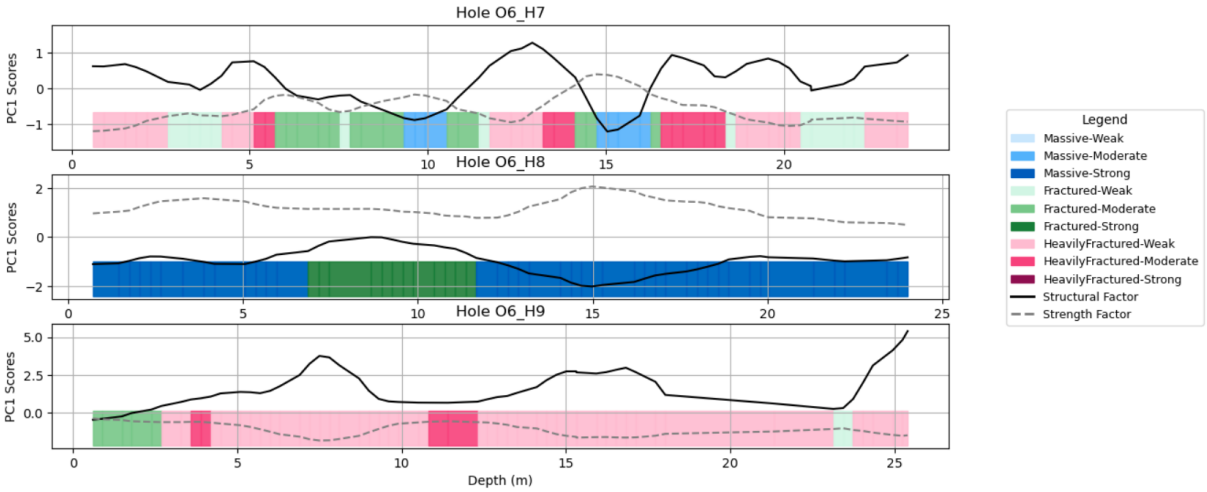

Figure 43: Three adjacent holes that show erratic behaviour in their structural, strength and rock factors.

5.3.3. PCA Variance for Factors

Table 12 summarises the variance explained by the first two principal components for both factors in the two analysed areas. Across datasets, PC1 captures approximately 31–46% of the variance, with PC2 contributing a further 20–27%, yielding 58–67% in the PC1–PC2 plane. This indicates that a single dominant pattern exists but is not overwhelming; variance is distributed across multiple dimensions. Compared with Navarro et al. (2021), whose calibration data exhibited stronger one-dimensionality (SuF: PC1 47%, PC2 18%; SeF: PC1 89%, PC2 6%), the present results are expected given the smaller number of holes and coarser sampling rate. In addition, cross-hole comparisons in this study reveal both aligned and divergent factor trends, consistent with genuine short-range geological heterogeneity that no single component should dominate, while residual mechanical influences likely remain even after processing.

Table 12: PCA explained variance for SuF and SeF determination.

Dataset	Factor	PC1 (%)	PC2 (%)	PC1+PC2 (%)
S7_a_642	SuF	36.98	26.39	63.36
S7_a_642	SeF	46.25	21.06	67.31
S0_612	SuF	40.61	20.12	60.73
S0_612	SeF	30.71	27.46	58.17

Consequently, PC1 should be interpreted as a first-order trend index rather than a complete reconstruction of rock behaviour. A prime example is the SeF of the S0_612 dataset, where PC2 (27.5%) is close to PC1 (30.7%), suggesting at the current stage of data availability that a two-component view would be more believable than a PC1-only projection.

5.3.4. Comparison with Geology and BI

Attempts to cross-reference the structural classifications of the MWD with the geological model were inconclusive. The geological model itself is interpolated at a broader scale and does not significantly reflect the observed variation in the MWD signals. The geological model identifies two geological units in the S7_a opening drill path. These are a sericite host rock and a porphyry unit extending like a bubble. Almost all drillholes pass the porphyry unit at some point, some of them even re-enter the sericite unit. However, no clear indication is observed in the MWD data that shows a clear border between geologic units. This is unsurprising at best, since the geological model is usually just an indicator of the location of geologies. However, without confirmation what lithology is drilled at a certain moment in time makes linking the BI and FBI difficult. At no moment could one be sure that they are corresponding the right MWD logs with the correct geological unit. In the worst case, unreliable MWD data will cloud the original BI estimates. Table 13 shows the distributions of the RF in the two geological units for not only S7, but also S0. For S7, the data show mainly that both geologic units contain a mix of structural conditions, and a trend that stands out is the Heavily Fractured-Weak class, being the largest contributor for the porphyry rock type and the second largest contributor in the sericite unit. Massive-Strong is a strong contributor in a similar fashion. This may indicate that these conditions are not limited to a single lithology and are more widespread. The weighted mean RF allows comparison between lithologies despite different drill meterage, by assigning scoring to every subclass from 1 to 9. Here, one can observe that the two porphyry units are in average matched, but not with respect to their classes.

Table 13: Rock Factor distribution by lithology (%), with weighted mean RF score.

	Breccia (S0)	Porphyry (S0)	Porphyry (S7)	Sericite (S7)
Drill meterage (m)	238.4	26.9	208.0	334.0
HeavilyFractured–Weak	13.3	14.0	28.4	20.6
HeavilyFractured–Moderate	11.3	18.4	8.0	7.1
HeavilyFractured–Strong	8.2	7.7	0.3	2.5
Fractured–Weak	15.2	2.2	7.9	10.1
Fractured–Moderate	15.2	22.3	18.8	14.3
Fractured–Strong	12.1	6.7	7.7	12.8
Massive–Weak	5.6	9.3	—	1.5
Massive–Moderate	7.4	12.7	9.4	7.6
Massive–Strong	11.7	6.7	19.5	23.6
Weighted mean RF (1–9)	**4.74**	**4.61**	**4.68**	**5.14**

A qualitative assessment can be made by comparing the BI/FBI input variables with the MWD factors. In Table 13, it can be seen that the average sericite signal receives the highest RF score. This is striking since this gradation of the RF values does not align with the BI/FBI ranges presented in Table 10. Overall, RF indicates that porphyry and breccia may be less competent and more blastable than their high BI/FBI values imply. Whereas the opposite applies for sericite. Significant sections of heavily fractured material can be seen, yet the BI suggests a more competent rock. Together, this could be an indication of the value of integrating MWD to capture fine-scale structural weakness. This is essentially the difference between these data. Input variables tailored for BI/FBI operate at macro-scale, whereas MWD operates at meso-scale. Where one captures an averaged damage signal at 30 cm and every anomaly influences the outcome, the other uses more broader structures like BRQD over longer pieces of core designed for large-scale faces.

6
Design Implications

This chapter first describes how the Kankberg stopes are categorised into zones of expected blast performance using fuzzy and empirical blastability. Then, describes how these indices can be used in conjunction with real-time MWD signals, although they are currently limited, to verify or improve local drilling conditions. Instead of presuming rock mass homogeneity, the framework combines insights to offer a rational foundation for differentiating drill and blast design parameters, such as burden, spacing, and timing. Since site-specific empirical calibration and post-blast reconciliation are necessary, precise design values are not recommended here. This would be misleading. Rather, the scenarios and real-world considerations that are presented are meant to serve as a proof-of-concept to direct the development of feedback loops and pilot testing in the future. Given its influence on overall stope performance, the opening slot raise is the main focus for these implications.

6.1. Forecasting with Blastability Indices

Based on the BI/FBI values obtained per stope, one can strategically adjust design parameters. BI/FBI outputs will be the first tool that a drilling and blasting engineer will look at to assess the condition of the rock mass. Essentially, an engineer is free to use the tools at his disposal freely. Tools, such as the BI/FBI, can and should be complemented by expert knowledge.

Hypothetically speaking, an engineer can prefer to save as much money as possible by drilling as little as possible while maintaining proper blast results. This could be achieved by using two slot designs, respectively, design A and B. Design A is conservative, requires more drill meterage, and more preparations in terms of positioning the equipment. On the other hand, design B uses a much more aggressive approach. It is faster, cheaper, but also more risky. The aggressive slot design will allow for fewer blastholes and reamed holes, subsequently reducing the required drill meterage, bit replacement, and time spent in a hazardous environment, with the downside of lowering the void ratio. Designs A and B should not be considered as the best slot option, as extensive testing is required to validate the design, and a vast amount of variations are possible.

So, the BI/FBI highlight the stopes within the stoping area that can be considered for initial testing of less-conservative and efficient designs. Therefore, it should be used as a guide for the next steps of optimisation. For the proposed designs, we split the stoping area into four quartiles (Figure 45). the first quartile of blastability values have relatively favourable blasting conditions and are suitable for less conservative setups, the second and third quartiles are seen as a transition zone and should be further analysed, and the fourth quartile is considered to have unfavourable blast conditions and should be approached with a conservative design to limit losses and/or secondary blasting.

6.1.1. Drill Patterns

Figure 44 shows 4 opening slots. Two of them (a and b) were used in the Kankberg mine. Slots c and d are borrowed from the literature. The slots all contain different void ratios; in here, the global void ratio represents Chandrakar et al. (2023)'s method, as introduced in Section 2.4.2. The local void ratio is added, as suggested in Lovitt and Collins (2013). They argue that the global void ratio is a meaningless variable because it is extremely unlikely that all the reamers in the area would be connected by the first shot. A valid concern, but certain studies, such as Chandrakar et al. (2023)'s, indicated the global cut area against blast outcomes. Therefore, the author finds both to be necessary for potential future comparisons with other research.
Based on the respective void ratios, the suitability of a slot to the more aggressive or conservative role can be determined. The most costly by far is the Kankberg slot (a), which requires 10 reamed holes, 26 holes in total, and not even the best void ratios to balance the effort. The second slot, also used in Kankberg, is the Double Burn/Box slot, or simply referred to as the Double Idiot by mine workers (since even idiots can blast a slot with this pattern). Even

though the name is humorous, it still has more than double the proportion of voids for the global and slightly less than double for the local. At the cost of one extra blasthole, but 3 less holes to ream. One potential disadvantage is tighter hole spacing, which requires more careful drilling. Also, there are 7 lines of holes to be layed out, meaning more repositioning of drill rigs. However, this thesis is based on the assumption that the cost of additional reamer drill bits and reaming will exceed the cost of time lost in drilling an additional blasthole and extra positioning. In addition, because of the extra blasthole, the Double Burn/Box/Idiot slot can fit extra explosives to be put inside the hole. This, in turn, creates space to expand the powder factor in case it is needed. But measurements taken after a blast have also shown that the material was too powdery. That would suggest patterns with lower powder factors can work well. This is where the literature-based Double Burn/Box/Idiot slot (c) comes into the equation. It requires a wider spacing, thus lowering the void ratio since there are fewer holes and more area. This slot is unique in its design from the others because it is more protective of the blastholes due to shielding with reamer holes, and thus the freezing risk is minimal. In addition, the spacing is wider and less sensitive to poor drilling accuracy. The last slot, the Swedish slot (d), is also unique. If drilling deviations cannot be controlled to be less than 1-2%, this method offers a good alternative for better drilling outcomes. Its global void ratio is better than the other slots and will guarantee the creation of a void. However, there are major disadvantages, such as that there is no protection for adjacent holes, which can result in misfires, and the need for specialised equipment to conduct parallel drilling.

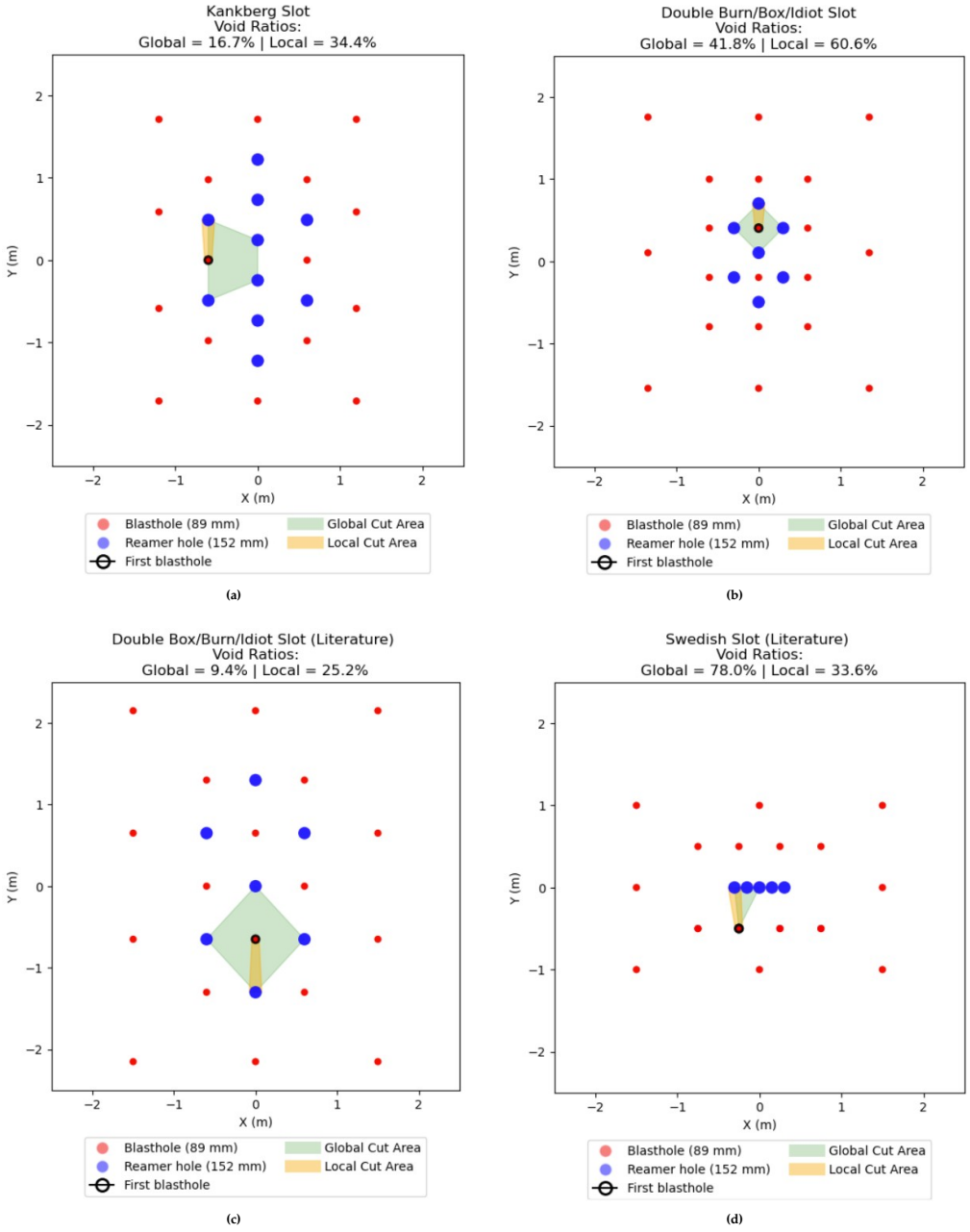

Figure 44: Selection of multiple openings slot designs.

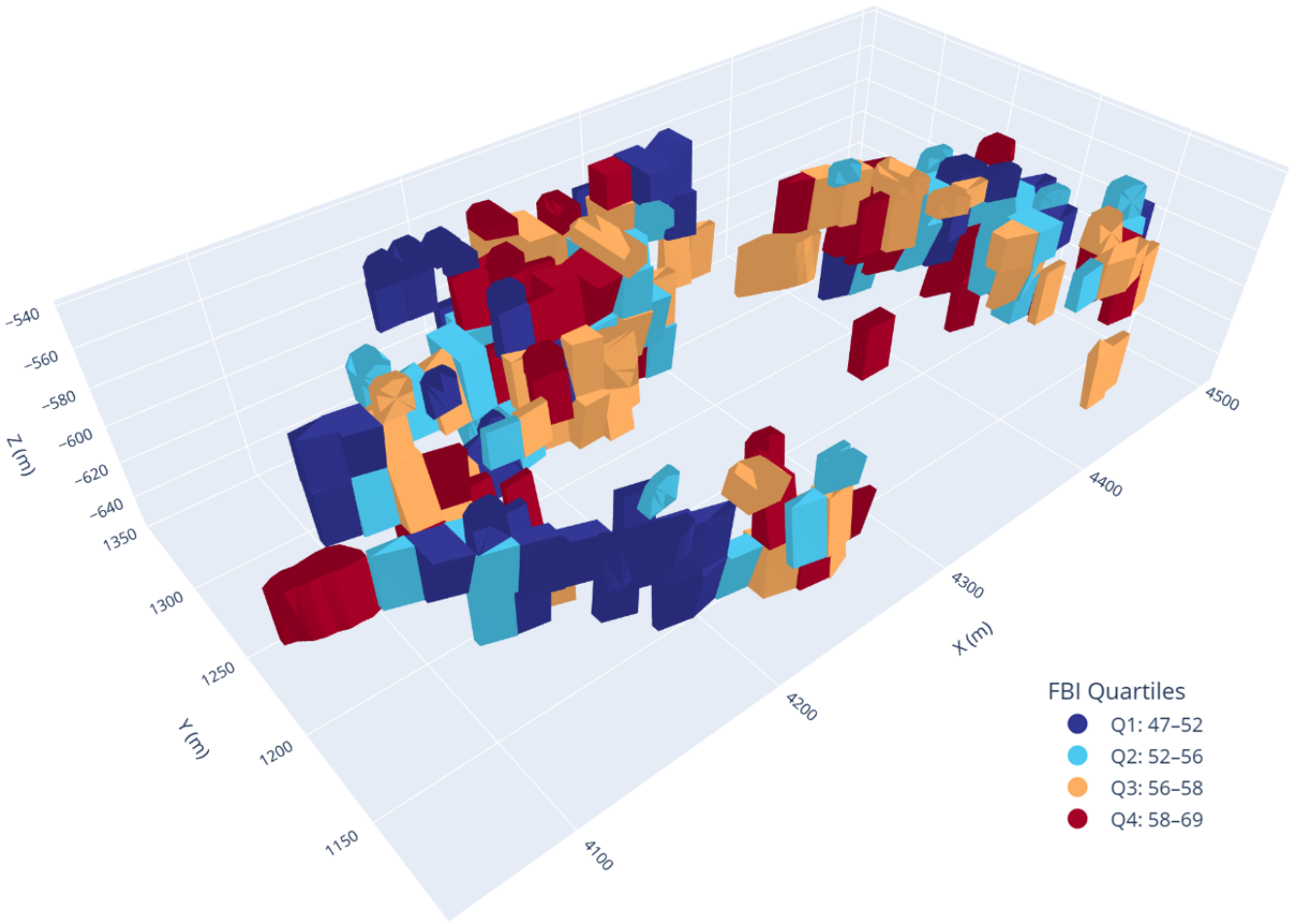

Figure 45: FBI quartiles across stoping area.

Slot Selection Logic

The void ratio, drill effort, reaming costs, and operational risk are all trade-offs for the slot options mentioned in the previous section. The BI/FBI framework identifies areas where design changes may be warranted rather than dictating a single "best" slot. At this stage, the variations among stopes might not justify distinct slot designs for every stope due to the thesis's comparatively small range of FBI values. However, the index can be used to rank which stopes should be used by default for conservative designs and which ones are best suited for testing more aggressive, less expensive slots. MWD signals aid in improving these choices by offering an additional real-time check on local drillability conditions.

6.1.2. Worked Example: Stope S7a

Stope S7a was classified in the lowest FBI quartile and shows a relatively variable MWD-derived Rock Factor for its opening slot, indicating generally favourable blast conditions. Data suggest consistent but locally variable drillability, with signs of fractured zones that could help fragmentation if handled with care. Given these conditions, the framework would recommend considering a more aggressive slot raise pattern in S7a as a pilot test. For example, switching from the current Kankberg slot, which is reaming intensive and costly, to a Double Burn/Box slot which reduces drill meterage, bit wear, and rig time by using fewer reamed holes. However, slightly variable Rock Factor trends highlight that local zones of stronger rock or unexpected structure may still exist. Therefore, the site engineer should treat MWD signals as a last-moment check: fine-tuning charging and delay timing if variable rock is encountered during drilling. Considerations such as delay timing should then follow from the literature, as described in Section 2.4.2.

The S7a scenario shows how FBI and MWD together provide a data-informed basis to trial a less conservative design where risk is acceptable. Post-blast reconciliation of fragmentation, CMS, and actual drill deviation would be critical to confirm whether the design is benefiting from the framework. Either way, insights from this pilot could then feed back into adjusting the pattern selection for future stopes with similar conditions.

7
Discussion

This thesis aimed to develop a rock parameter-based framework for blast design, with more efficient and adaptive practices as the main goal. Through a combination of a literature study, laboratory tests, data processing, and modelling, this work sought to find insights on how the D&B cycle could take a step up from a pure trial-and-error-based approach to a more scientific way of working. The document explored why and how rock breakage occurs, showed that blastability indices and MWD data can offer useful information for better decisions, and tested how well they work together. On top of that, a full conceptual implementation of this was created to support the feasibility of this framework. This chapter will bring together the main points and take a critical look at what worked, what did not, and what it all means. The primary objective here is to keep things honest, outlining where this framework stands today, what gaps still exist, and what would need fixing before any pilot test is conducted. The chapter will first review the work before giving follow-up recommendations.

7.1. Limitations of the Framework

The principal benefit of this framework is that it moves Kankberg's D&B planning beyond a uniform drill pattern towards a more risk-ranked and flexible approach. Despite its constraints, the framework encourages site engineers to reconsider assumptions about rock mass homogeneity and to weigh when conservative versus more aggressive designs may be appropriate. This has clear operational relevance. In more competent rock masses, even modest reductions in drilled metres can result in significant savings, especially given low penetration rates and high bit wear. Currently, data-driven design decisions are not yet routine practice in Kankberg. Introducing a blastability index, supported by fuzzy logic and MWD data, represents a step towards a more informed and potentially semi-automated planning process. Over time, if MWD measurements correspond well with blastability predictions, confidence in this approach could increase. A further advantage is that it does not depend on expensive new equipment, but rather on improved use of existing data, standard laboratory analyses, and routine MWD logging. However, it remains clear that the framework is in a conceptual stage. The following sections summarise the key methodological and data-related limitations and highlight areas that would benefit from additional development.

7.1.1. Methodological Limits

The limitations of the framework must be clear before any pilot tests are conducted. First of all, it is important to recognise that rock type characteristics, which build this framework, are only one part of blast performance. Other critical factors, such as charging accuracy, timing, groundwater, and wave propagation behaviour, strongly influence breakage but are not explicitly captured in the framework. Some of these aspects were discussed in the theoretical background because of their importance in understanding the underlying factors at play, but they remain outside the scope of the current model and should be acknowledged as areas for future integration.

Blastability Indices

Adopting Lilly's BI is reasonable given its widespread use in mining and some applications underground (Alipour et al., 2018; Azimi et al., 2010; Z. Zhou et al., 2024). However, the original scoring system was not specifically developed for complex underground environments. For instance, the powder factors for underground slot raises are typically much higher than for surface operations (Dyno Nobel Asia Pacific Pty Limited, 2025), which complicates the transferability of the outputs between sites. Nevertheless, within this framework, relative differences between stopes are of greater interest than absolute BI values, which partially mitigates this limitation.

The fuzzy logic-enhanced model offers a clear improvement in managing uncertainty and smoothing abrupt transitions that can arise with crisp threshold approaches. However, fuzzy systems rely on rule bases that are inherently subjective and require reliable expert input. In this thesis, the fuzzy MFs and the rule base were defined by the author. Although this provided workable outputs, the subjectivity of these definitions means that the results may vary between

practitioners. So, this work demonstrated a simple rule set to illustrate the concept, but application would realistically require further calibration with experienced blasters and site engineers to ensure that the rules are representative of local conditions. A poorly defined rule base or poorly calibrated membership functions could undermine the reliability of the model. Furthermore, from the sensitivity analysis it was evident that small changes in weighting produced additional variations in the FBI values, again stressing the need for expert judgement and close observation of the rock mass. The results also showed that the volcaniclastic rock type was relatively insensitive to weighting choices, whereas porphyry and andalusite quartzite showed much stronger dependence. This means that data from certain rock types might be more contradictory with respect to blasting, requiring further investigation and calibration. Although a sensitivity analysis was performed, alternative defuzzification methods were not tested. If different defuzzification strategies produce divergent outputs, this would indicate the need for further refinement. Despite these concerns, the fuzzy logic approach represents a practical upgrade, as it allows more realistic transitions between classification boundaries.

MWD Rock Factor

Incorporating MWD data to reflect local rock variability is a promising aspect of this framework and supports the validation of the blastability index to some extent, in addition to being complementary information for the D&B engineer. However, MWD data are known to be affected by several external factors, including rig settings, sensor calibration, bit wear, and hole depth. Although this thesis accounted for depth-related effects, other influences, such as bit replacement timing, were beyond the scope of the project. Future work should include improved data collection practices and, where possible, additional validation methods such as borehole imaging as performed in Navarro et al. (2021) to cross-check MWD trends. This is stressed by the PCA analysis, where PC1 explained relatively little variance. In the results section, it was speculated that it is probably due to the small and noisy data set. However, the PCA results hint at a potential multidimensional factor to describe the rock mass. For follow-up studies, it is therefore encouraged to explore both, by increasing available MWD data and experimenting with higher dimensionality for the indices, contrary to Navarro et al. (2021).

Another important consideration is that MWD-based models cannot be transferred directly between rigs or sites without recalibration. Site-specific lithologies, rig configurations, and operational practices must be considered to avoid misclassifications. However, just like with the indices, the main concern here is to compare stopes with one another instead of looking at the absolute values. This reduces the associated problems with this limitation. In general, MWD data can add significant value to the blastability framework but should be treated as a complementary tool rather than a standalone predictor. This is illustrated by its potential to give contradictory results to the blastability indices. Cross-hole comparisons were mixed, with some poor alignment for rock types compared to the BI's, which likely highlights that small-scale heterogeneity and operational artefacts both affect RF stability much more than the BI inputs. This mismatch illustrates the challenge of reconciling meso- versus macro-scale features, yet also showcases its strength to be able to study the rock at different scales.

7.1.2. Data Limits

In addition to methodological considerations, the success of the framework ultimately depends on the quality and representativeness of the input data. The geological model, laboratory test results, and MWD signals must be consistent and closely aligned with the actual conditions in the stoping area. Sparse, biased, or poorly reconciled data will inevitably affect the reliability of the output. This is not a specific concern for this thesis; models always have to be mindful of RIRO (Rubbish in, Rubbish out).

The input variables for BI were derived from geotechnical logs, laboratory tests, and some underlying assumptions. While parameters such as RMD and JPS are standard practice, the data set showed high variability, reflecting the inherent heterogeneity of the site. The JPO was estimated on the basis of a single natural fracture, which may represent conditions throughout the entire stoping area. However, this claim is, qualitatively speaking, very uncertain. In practice, additional face-mapping would be required to refine this input. Similarly, the RDI and H values were based on a limited number of laboratory samples, many of which contained pre-existing fractures. Ideally, tests would be performed on fully competent samples to better capture intact rock strength, as recommended by ASTM and ISRM standards (ASTM International, 2017; Ulusay & Hudson, 2007). A 'competent only' version of the BI/FBI was also developed to illustrate how intact samples affect index scores. However, the small number of competent samples available means that this scenario still carries its own uncertainties. Additional sampling would be required to strengthen this input. Point-load tests, which have been conducted previously, could, despite their drawbacks, complement UCS measurements to increase confidence in these inputs.
The quality of the geological model is equally important. If this is inaccurate or outdated, the resulting blastability classifications will per definition be unreliable. Although the current data set was sufficient for a proof-of-concept, broader and more representative sampling would be essential for field application.

The MWD data set used in this study was relatively consistent, but sometimes noisy. This was reflected in stope S7a, where inconsistent depth tags and other data inconsistencies do reduce confidence in the RF despite general geological agreement in examples given in the results section. Furthermore, the sampling interval (one reading per 30 cm) may not capture fine-scale variability, especially since rod additions every 1.83 m can overlap multiple data records. Interpolation and smoothing were used here for simplicity, but in practice, over-smoothing should be avoided to retain meaningful variations. Furthermore, cross-checks with borehole videos or face mapping would help verify that trends are genuine and not operational artefacts.

7.1.3. The Feedback Loop

Perhaps the most significant limitation (and opportunity) lies in developing a robust feedback loop. This framework relies on comparing the predicted blastability with the actual blast performance. Although CMS surveys provide valuable input, their data may by itself prove insufficient to pinpoint all factors that contribute to over- or under-break, let alone fragmentation. Therefore, additional fragmentation data would be highly beneficial, particularly since the BI/FBI output can be correlated with powder factors using site-specific equations, as suggested by Lilly (1992).

Establishing this feedback loop would require site engineers to track predicted versus actual results and update the model over time. Although this is sensible in theory, it requires ongoing discipline and allocation of site resources, which may not always be available. However, without it, even the best models will drift from practical reality. Embedding this practice into standard procedures is therefore essential if the framework is to remain useful and reliable.

7.1.4. Implications on Design

Realistically speaking, some parts of the framework are easier to implement than others. For example, translating MWD anomalies into immediate charging or timing changes requires experience and clear protocols, which Kankberg does not yet have.

The use of a BI/FBI to forecast blast conditions is an obvious next step to improve performance and achieve more consistent results. However, since no testing has been done, it is uncertain whether the BI/FBI outcomes, which were relatively similar in value, justify the use of several opening slot designs. Furthermore, slot raises are extremely sensitive to drill deviation. An aggressive pattern that works on paper may freeze if the void space is not opened as intended or if the holes deviate more than anticipated. The risk of a misfire is higher, which means that site engineers will naturally favour conservative designs unless they trust the classification system. The example of Stope S7a illustrated this tension. Although FBI values suggested opting for a more aggressive slot pattern, unvalidated models will make site engineers reluctant to adopt such changes without pilot evidence, especially for stopes that are too costly too lose due to misfiring slots. So, practical gains must outweigh operational risks. Saving drill metres by switching to a more aggressive slot pattern only makes sense if the predicted gains hold up under normal drilling variability. At this stage of development, many uncertainties remain. Some can be addressed fairly easily, while others require more effort and new equipment.

7.2. Future Work

The results and limitations in the previous section tackle several directions for further research and practical testing. These steps are key if the framework's reliability and practical value is to be improved and the framework is to move beyond a conceptual stage. This section will aim to provide some critical future work directions, with a final recommendation on prioritisation of points.

7.2.1. Data Improvements

A clear and relatively straightforward path for improving the framework is to strengthen the input variables, though some improvements are more realistic than others. For example, while it is easy to demand a more accurate geological model, the reality is that Kankberg's model already contains more detail than other Boliden mines. What would make an immediate difference is to add existing PLT-data, despite its drawbacks, to increase confidence in the UCS results that feed into the blastability index. Another practical improvement is better structural mapping. This is critical, not only for the D&B engineer aiming for optimal blast performance, but also for the geotechnical engineer monitoring safety. Although engineers cannot observe the stope before blasting, they do have access to a free face near the stope. Routine mapping will help refine the JPO values and verify assumptions that currently fill the framework's gaps. Lastly, Schmidt-Hammer testing could be used to indirectly estimate UCS values. Although this method is less accurate than lab tests, its main strength is that it is inexpensive and easy to use. If applied consistently, for example during mine rounds, it could help build a larger dataset of estimated UCS values over time. With enough data points, statistical trends guided by laboratory tests as benchmarks can make these estimates more reliable.

With regard to MWD, the first thing that needs immediate action is the way data are recorded and stored. The gathering of MWD data is extremely valuable now and is most likely for advanced projects at a later stage. However, current data storage is unacceptable. MWD data handling will need more refined storage, clear naming, no duplicates, and no concatenated files, preferably at a higher sampling rate to allow for more aggressive filtering of noise and lower data losses during processing. If this does not happen, the data will be wrongly recorded, and, without time-intensive data handling as in this thesis, will essentially compromise the data's value. In addition, if possible, MWD signals should be validated with borehole cameras. Although precise alignment between the signal and actual conditions is less critical when simply reinforcing the BI/FBI, it becomes essential if the MWD data are to be used for last minute adjustments in the charging plan.

7.2.2. Method enhancements

The methods used in this framework are generally sound. The thesis does not rely on untested concepts but combines approaches with proven track records. Lilly's BI, Mamdani FIS, and a modern approach to MWD data have all shown their practical use in other studies and are merely synthesised to work towards a common goal. These are considered sophisticated enough to justify moving towards pilot testing. However, enhancements are still recommended. The rule base and membership functions should be refined with input from site experts, and the weights of the input variables could be adjusted as more reliable data becomes available. Under the assumption that the input data adequately reflect actual blast conditions, future work should use real blast outcomes to calibrate the framework. This would allow the blastability index to be tuned to local conditions and improve its predictive value.

7.2.3. Closing the Feedback Loop

Embedding quantitative reconciliation into the D&B cycle is essential to close the feedback loop and move beyond a static conceptual framework. This means that every blast should become a learning opportunity. Several options for obtaining meaningful post-blast data were discussed in this thesis. Of these, routine particle size distributions are the most practical and are directly related to blast performance. For example, CMS surveys can be complemented by straightforward fragmentation checks, such as muck pile photo analysis, to test if the predicted blastability aligns with real breakage results on the ground. In the long term, the D&B cycle should not stop at static classification of blastability. Once basic post-blast tracking becomes standard, the next step is to add simple fragmentation modelling alongside the blastability tool. This would create a continuous loop where design, execution, and reconciliation feed each other, so that design assumptions can be adjusted based on data before problems become costly. Without this feedback loop, the framework might inevitably drift from reality.

7.2.4. Pilot Testing

Pilot testing is the logical next step, potentially after inclusion of better input data and routine reconciliation are in place. Some pilot work can already be performed at Kankberg without major new equipment or major workflow changes. For example, stopes classified in the most favourable FBI quartile can be used to trial a less conservative slot raise design under controlled conditions. This would test whether the predicted lower blastability actually translates to practical cost or time savings, such as fewer drilled metres or faster slot development. At this stage, performance should be carefully measured. Practical metrics, such as metres drilled, void opening success rates, powder factor used, and basic fragmentation checks, should be recorded for each pilot. Any misfires or unexpected results should feed back into the blastability index and fuzzy rules, rather than being dismissed as outliers. Routine MWD logging can also be used during these pilots to compare real-time Rock Factor trends with the predicted FBI zones. Even if the MWD data are not yet used for live pattern adjustments, it can already show whether the trends match the conceptual model. Over time, consistent agreement would build trust in the framework; consistent divergence would highlight the need to revisit the input variables. To manage operational risk, these pilots should be staged. Early tests should stay low-risk by focussing on stopes with favourable conditions, where a more aggressive pattern has a lower chance of freezing or misfire. In other words, pilot tests should prove the benefits of the framework step by step, not by chasing maximum savings in one attempt. Figure 46 shows the desired feedback loop that this thesis conceptualises. It encompasses the full methodological flow, from the use of the blastability tool in the design phase, up to quantitative monitoring of post-blast metrics.

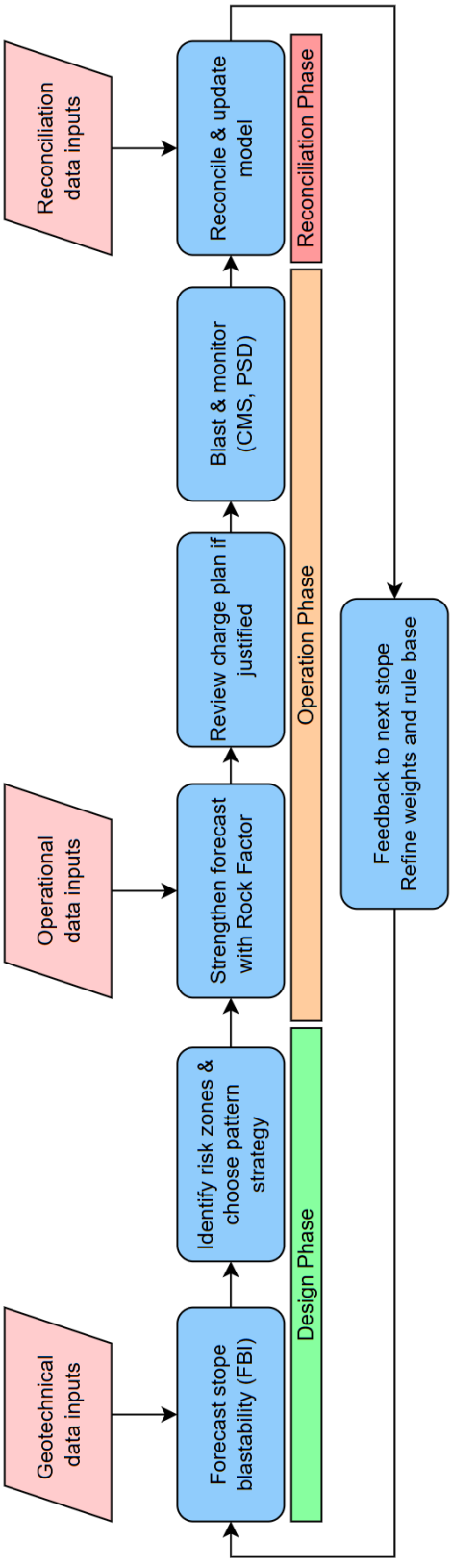

Figure 46: Conceptual feedback loop for adaptive D&B design. Each stage builds on site data and operational feedback, with pilot testing and routine monitoring to close the loop and update the framework.

8

Conclusion

This thesis set out to improve blasting in the Kankberg stopes. It aimed to develop a data-driven design framework that would not only be relevant for site-specific implementation, but also have utility outside of Kankberg. Erratic blasting performance in the stopes incentivised the need to move away from trial-and-error approaches and move to more efficient systems. It became apparent that the understanding of blasting within the mine operations was limited. Therefore, a thorough theoretical background and study area analysis showed why the suggested system matters, what proper reconcilliation can look like, and how the operation will benefit from a more data-informed system. To achieve this, the research itself focused on forecasting the blastability of stopes using geotechnical data, since this was readily available. This was achieved by a combination of fundamental theory, site-specific data, laboratory tests, and the implementation of a fuzzy logic system to show how, mainly geotechnical properties, can support better design practices in sublevel stoping.

Through the integration of an industry-recognised BI with fuzzy logic and additional MWD support, the study demonstrated that it becomes feasible to classify stopes into zone of expected blastability and acknowledged how design decisions can flow from these tools. One should note that the system is not a novel method, courtesy of the author, but relies on grounded and accepted methods. The novelty here arises from the synthesis and site-specific adaptation of these methods. At the same time, the thesis stresses that the predictive power of the framework is constrained at the conceptual stage. Key limitations include unquantified uncertainties with respect to the effectiveness of multi-pattern blast strategies, the lack of high-quality reconciliation metrics, and other practical factors. These include disregard for the influence of groundwater, explosives, and many other factors that are present to some degree in the D&B landscape. The data that fed the blastability indices, especially laboratory tests, were limited by the low number of available samples and the additional assumptions that filled the gaps in the blastability input, such as the JPO. Lastly, the current MWD Rock Factor only covered a single stope, however, to show the true effectiveness of the Rock Factor one would need to compare the blastability and Rock Factor of at least two stopes. If trends point to the same direction, this would suggest that the models perform as intended.

Despite these existing gaps, the thesis shows, on a conceptual level, that feeding geotechnical data into a fuzzy-enhanced blastability index and routine MWD check can help engineers move towards a more risk-assessed and flexible way of working. It forces the practitioner to critically evaluate their designs, without simply copying designs from other mines. The biggest strength of the framework is that it initially builds on practical, accessible methods that are already available in the Kankberg mine and combines them together for greater practical utility. In addition, suggestions for further development of the framework from a concept stage towards real implementation are layed out, aiming to make the system as ready as possible for piloting.

In summary, the findings of the thesis address the research questions as follows:

- *How can site-specific data be used to classify stopes based on their expected blast performance to inform D&B design?*

  Through the combination of various geotechnical data streams, such as geotechnical core logging and laboratory tests, a blastability index can be synthesised. Fuzzy logic effectively enhances the original empirical method. This results in a final single metric that classifies stopes from a mainly geotechnical perspective. If increased confidence is desired, the use of more representative sampling, pilot testing, and the inclusion of overlooked parameters, such as explosive parameters, is required.
- *To what extent does MWD data support the blastability index as a valid predictor of rock behaviour during blasting?*

  MWD Rock Factors trends are theoretically able to support the blastability index. Local drilling signals, which are not fed into the blastability index, can validate or challenge blastability forecasts, but at the current stage of

the framework, more validation of rock factor using borehole imagery, trials across multiple stopes are crucial to truly pinpoint effectiveness.

- *How can theory, blastability index results and MWD data guide theoretical improvements in opening slot design?*

  A worked scenario highlighted that using the FBI classification as a tool for deciding whether a stope is suitable for more aggressive or conservative slot patterns. However, practical risks, such as drill deviations, which current data indicate to be severe, mean that any design changes should be pilot tested under strict conditions (i.e. deviation measurements, meticulous reporting of operational hiccups) before widespread adoption is advisable.

Together, these subquestions answer the main research question:

- *How can rock mass data be used for an actionable drill and blast methodology to improve operational efficiency in the sublevel stoping area of Kankberg?* This thesis shows that by structuring site-specific rock data into a fuzzy enhanced blastability index and complementing it with real-time MWD trend checks, engineers can make more informed pattern choices. Although the framework is conceptual, it provides a practical basis for adaptive design decisions that can reduce unnecessary drilling and manage risk, if paired with routine reconciliation to maintain alignment with site conditions.

Essentially, the study demonstrates that while the framework is not yet a ready-to-go design tool, it is a practical first step towards next generation adaptive, non-erratic and lower-cost D&B operations in Kankberg, and potentially other mines with similar conditions. If the feedback loop is systematically embedded in D&B design cycle, with better data discipline, routine reconciliation, and proper collaboration between operators and engineering teams, this approach can evolve from a concept product to a site-customised tool that reduces wasteful drilling and improves overall blasting results.

Bibliography

Akbay, D., & Altindağ, R. (2020). Reliability and evaluation of point load index values obtained from different testing devices. *Journal of the Southern African Institute of Mining and Metallurgy*, *120*(3), 181–190. https://doi.org/10.17159/2411-9717/759/2020

Alipour, A., Mokharian, M., & Chehreghani, S. (2018). An application of fuzzy sets to the blastability index (bi) used in rock engineering. *Periodica Polytechnica Civil Engineering*, *62*. https://doi.org/10.3311/PPci.11276

Allen, R. L., Weihed, P., & Svenson, S.-A. (1996). Setting of zn-cu-au-ag massive sulfide deposits in the evolution and facies architecture of a 1.9 ga marine volcanic arc, skellefte district, sweden. *Economic Geology*, *91*(6), 1022–1053. https://doi.org/10.2113/gsecongeo.91.6.1022

Anderson, J. D. (2003). *Modern compressible flow: With historical perspective* (3rd). McGraw-Hill Education.

ASTM International. (2017). Standard test methods for compressive strength and elastic moduli of intact rock core specimens under varying states of stress and temperatures [ASTM International, West Conshohocken, PA, USA].

Azimi, Y., Osanloo, M., Aakbarpour-Shirazi, M., & Aghajani Bazzazi, A. (2010). Prediction of the blastability designation of rock masses using fuzzy sets. *International Journal of Rock Mechanics and Mining Sciences*, *47*(7), 1126–1140. https://doi.org/https://doi.org/10.1016/j.ijrmms.2010.06.016

Bauer, T., Skyttä, P., Hermansson, T., Allen, R., & Weihed, P. (2014). Correlation between distribution and shape of vms deposits and regional deformation patterns, skellefte district, northern sweden. *Mineralium Deposita*. https://doi.org/10.1007/s00126-013-0503-2

Bond, F., & Whitney, B. (1959). The work index in blasting. *Proceedings of the 3rd U.S. Symposium on Rock Mechanics (USRMS)*.

Brown, E. (Ed.). (1981). *Rock characterization, testing and monitoring: Isrm suggested methods*. Pergamon Press.

Chandrakar, S., Paul, P., & Sawmliana, C. (2021). Influence of void ratio on "blast pull" for different confinement factors of development headings in underground metalliferous mines. *Tunnelling and Underground Space Technology*, *108*, 103716. https://doi.org/https://doi.org/10.1016/j.tust.2020.103716

Chandrakar, S., Paul, P., & Sawmliana, C. (2023). Long-hole raise blasting in a single shot: Assessment of void ratio and delay time based on experimental tests. *Engineering Structures*, *275*, 115272. https://doi.org/https://doi.org/10.1016/j.engstruct.2022.115272

Cunningham, C. V. B. (1983). The kuz-ram model for prediction of fragmentation from blasting. *Proceedings of the 1st International Symposium on Rock Fragmentation by Blasting (FRAGBLAST-1)*, 439–453.

Cunningham, C. V. B. (2005). The kuz–ram fragmentation model – 20 years on. *Proceedings of the 3rd International Conference on Explosives and Blasting Technique*, 201–210.

Deere, D. U. (1989). *Rock quality designation (rqd) after 20 years* (Contract Report No. GL-89-1). U.S. Army Corps of Engineers. Vicksburg, MS, Waterways Experimental Station.

Deere, D. U. (1964). Technical description of rock cores for engineering purpose. *Rock Mechanics and Enginee-ring Geology*, *1*(1), 17–22.

Dessureault, S. (2004). Mge 415 – rock excavation: Lecture notes and drilling theory [Based on SECOROC Geology Drilling Theory, Document S-96174].

Dey, K., & Sen, P. (2003). Concept of blastability – an update. *Indian Mining and Engineering Journal*, *42*(8&9), 24–31.

Dyno Nobel Asia Pacific Pty Limited. (2025, January). *Explosives engineers' guide* (Technical Report). Dyno Nobel Asia Pacific Pty Limited. https://www.dynonobel.com.au/siteassets/guides/dyno_nobel_explosive_engineers_guide_2025_01_hr.pdf

Faramarzi.H, M., & Esmaeili, K. (2025). 3d rock fragmentation analysis using lidar, based on point cloud deep learning segmentation and synthetic data. *Powder Technology*, *456*, 120861. https://doi.org/https://doi.org/10.1016/j.powtec.2025.120861

Fernández, A., Segarra, P., Sanchidrián, J. A., & Navarro, R. (2024). Ore/waste identification in underground mining through geochemical calibration of drilling data using machine learning techniques. *Ore Geology Reviews*, *168*, 106045. https://doi.org/https://doi.org/10.1016/j.oregeorev.2024.106045

Ghose, A. (1988). Design of drilling and blasting subsystems—a rock mass classification approach. *Proceedings of the Symposium on Mine Planning and Equipment Selection*, 335–340.

Goodman, R. E. (1991). *Introduction to rock mechanics*. John Wiley & Sons.

Han, J., Xu, W., & Xie, S. (2000). Artificial neural network method of rock mass blastability classification. *Proceedings of the Fifth International Conference on GeoComputation*, 23–28.

Harraz, H. (2014, February). *Sublevel stoping underground mining methods*. https://doi.org/10.13140/RG.2.1.4585.0483

Heydari, S., Hoseinie, S., & Bagherpour, R. (2024). Prediction of jumbo drill penetration rate in underground mines using various machine learning approaches and traditional models. *Scientific Reports*, *14*. https://doi.org/10.1038/s41598-024-59753-6

Hino, K. (1959). *Theory and practice of blasting*. Nippon Kayaku Co., Ltd.

Ikeda, H., Sato, T., Yoshino, K., Toriya, H., Jang, H., Adachi, T., Kitahara, I., & Kawamura, Y. (2023). Deep learning-based estimation of muckpile fragmentation using simulated 3d point cloud data. *Applied Sciences*, *13*(19). https://doi.org/10.3390/app131910985

Isheysky, V., Martinyskin, E., Smirnov, S., Vasilev, A., Knyazev, K., & Fatyanov, T. (2021). Specifics of mwd data collection and verification during formation of training datasets. *Minerals*, *11*, 798. https://doi.org/10.3390/min11080798

Jaeger, J., Cook, N., & Zimmerman, R. (2007). *Fundamentals of rock mechanics* (4th). Blackwell Publishing.

Jiang, F., Yang, W., Zhang, S., et al. (2017). Optimization of blastability parameters of ore rock based on multi-source information fusion theory. *2017 10th International Symposium on Computational Intelligence and Design (ISCID)*, 252–255.

Jönsson, H., Koorem, B., Heden, H., Hedman, H., Rigg, D., & Mattsson, B. (1999). *Status Report 1999: Åkulla Ostra Mine Investigation – Geology* (Technical Report). Boliden.

Kay, D. (2002). Digital blasting—an opportunity to revolutionise mass underground blasting. *MasMin2000*, 155–156.

Killick, R., Fearnhead, P., & Eckley, I. A. (2012). Optimal detection of changepoints with a linear computational cost. *Journal of the American Statistical Association*, *107*(500), 1590–1598. https://doi.org/10.1080/01621459.2012.737745

Knapp, R. B. (2004). 4.1 fuzzy inference systems (mamdani) [Lecture notes, COS 436: Human-Computer Interaction, Department of Computer Science, Princeton University. Accessed: 2025-06-01].

Kumar Himanshu, V., Mishra, A., & Roy, M. (2023, May). *Blasting technology for underground hard rock mining*. https://doi.org/10.1007/978-981-99-2645-9

Latham, J.-P., Van Meulen, J., & Dupray, S. (2006). Prediction of fragmentation and yield curves with reference to armourstone production. *Engineering Geology*, *87*, 60–74. https://doi.org/10.1016/j.enggeo.2006.05.005

Latham, J.-P., & Lu, P. (1999). Development of an assessment system for the blastability of rock masses. *International Journal of Rock Mechanics and Mining Sciences*, *36*(1), 41–55. https://doi.org/https://doi.org/10.1016/S0148-9062(98)00175-2

Lilly, P. (1986). An empirical method of assessing rockmass blastability. *Large Open Pit Mine Conference*, 89–92.

Lilly, P. (1992). The use of the blastability index in the design of blasts for open pit mines. *Proceedings of the Western Australian Conference on Mining Geomechanics*, 8–9.

Liu, K., Yang, J., Li, X., Hao, H., Li, Q., Liu, Z., & Wang, C. (2018). Study on the long-hole raising technique using one blast based on vertical crater retreat multiple deck shots. *International Journal of Rock Mechanics and Mining Sciences*, *109*, 52–67. https://doi.org/https://doi.org/10.1016/j.ijrmms.2018.06.020

Lovitt, M., & Collins, A. (2013). Improved tunneling performance through smarter drilling and design. *Tunnelling in rock by drilling and blasting, 1st edn. CRC Press, Boca Raton, USA*, 7–14.

McFadyen, B., Woodward, K. R., Potvin, Y., & Grenon, M. (2020). A new stope reconciliation approach. In J. Wesseloo (Ed.), *Proceedings of the underground mining technology conference 2020* (pp. 335–350). Australian Centre for Geomechanics. https://doi.org/10.36487/ACG_repo/2035_17

M.I.T. (n.d.). Material properties of aluminum [Accessed: 2025-05-07].

Navarro, J., Seidl, T., Hartlieb, P., Sanchidrián, J. A., Segarra, P., Couceiro, P., Schimek, P., & Godoy, C. (2021). Blastability and ore grade assessment from drill monitoring for open pit applications [© The Author(s) 2021]. *Geotechnical and Geological Engineering*, *39*(6), 4701–4720. https://doi.org/10.1007/s00603-020-02354-2

Nordfeldt, P., Allen, R., Pitcairn, I., & Gibson, H. (2019). Topaz-rich breccias at the 1.9 ga kankberg au-te deposit, skellefte district, sweden.

Olsson, M., Nyberg, U., & Fjelborg, S. (2009). *Controlled fragmentation in sublevel caving—first tests* (Swebrec Report No. 2). Swebrec.

Onederra, I., & Chitombo, G. (2007). Design methodology for underground ring blasting. *Mining Technology*, *116*. https://doi.org/10.1179/174328607X282244

Online Mining Exam. (2015). *Explosives and blasting – part 3* [Accessed: 2025-04-02]. https://onlineminingexam.wordpress.com/2015/12/08/explosives-and-blasting-part-3/

Orica. (2023). Fragtrack™ – automated capture and reporting of fragmentation data [Accessed: 2025-06-06].

Ouchterlony, F., Moser, P., Nyberg, U., Olsson, M., & Gränfors, B. (2004). Where does the explosive energy in rock blasting rounds go? *Science and Technology of Energetic Materials*, *65*(2), 54–63.

Palmström, A. (2001). Measurement and characterization of rock mass jointing. *In-situ characterization of rocks*, 49–97.

Paterson, M., & Wong, T. (2005). *Experimental rock deformation–the brittle field* (Vol. 119). Springer.

Persson, P.-A., Holmberg, R., & Lee, J. (1994). *Rock blasting and explosives engineering* (1st). CRC Press. https://doi.org/10.1201/9780203740514

Rijsenbrij, A. (2024). *Larger scale mining in kankberg: A rock mechanical investigation of the transition from post-pillar mining to longhole open stoping* [Master's thesis]. Delft University of Technology, Faculty of Civil Engineering &

Geosciences [Supervisors: D.J.M. Ngan-Tillard, P.O. Bruna; Committee: D. Sandström, T.-O. Latta]. https://resolver.tudelft.nl/uuid:1fbc8909-7a59-4953-b1a7-59080c76b903

Schunnesson, H. (1996). Rqd predictions based on drill performance parameters. *Tunnelling and Underground Space Technology*, *11*(3), 345–351. https://doi.org/https://doi.org/10.1016/0886-7798(96)00024-7

Schunnesson, H. (1998). Rock characterization using percussive drilling. *International Journal of Rock Mechanics and Mining Sciences*, *35*(5), 711–725. https://doi.org/10.1016/S0148-9062(98)00004-2

SECOROC. (2004). *Geology drilling theory* [Document S-96174]. Atlas Copco SECOROC. Sweden.

Segaetsho, G., & Zvarivadza, T. (2019). Application of rock mass classification and blastability index for the improvement of wall control: A hard-rock mining case study. *Journal of the Southern African Institute of Mining and Metallurgy*, *119*(1), 31–40. https://doi.org/10.17159/2411-9717/2019/v119n1a4

Sellers, E., & Jackson, J. (2018). *Geological blasting related indices – key to underground open stope blasting improvements* [Presentation at FragBlast 12, Luleå, Sweden].

Tatiya, R. R. (2005). *Surface and underground excavations: Methods, techniques and equipment*. CRC Press.

Thin, I. (2019). Stope design – the importance of geotechnical and drill & blast interactions [Presented at NGM D&B Workshop, September 10, 2019].

Tshabalala, M., & Pretorius, J. H. C. Quality and reliability analysis of long-hole stope slots: A case study at south deep gold mine based on drilling and blasting practices. In: In *Proceedings of the international conference on industrial engineering and operations management monterrey*. South Africa, 2021.

Twining, B. V., & Lindsey, B. J. (2016). *Evaluation of borehole deviation and positional accuracy using gyroscopic and magnetic survey methods, eastern snake river plain aquifer, idaho national laboratory, idaho* (Scientific Investigations Report No. 2016-5163). U.S. Geological Survey. https://doi.org/10.3133/sir20165163

Ulusay, R., & Hudson, J. A. (2007). *The blue book: The complete isrm suggested methods for rock characterization, testing and monitoring: 1974-2006*. International Society for Rock Mechanics (ISRM).

Van Eldert, J. (2019). *Analysis of excavation damage, rock mass characterization and rock support design using drilling monitoring* [Doctoral dissertation, University of Technology, Luleå, Sweden].

Voigt, B., & Falshaw, S. (2024). *Boliden summary report: Mineral resources and mineral reserves | 2024 – kankberg* (Technical Report) (Prepared by Birger Voigt & Suzanna Falshaw). Boliden AB.

Weihed, P. (2001). A review of palaeoproterozoic intrusive hosted cu-au-fe-oxide deposits in northern sweden. In P. Weihed (Ed.), *Economic geology research* (pp. 4–32, Vol. 1). Sveriges geologiska undersökning.

Wimmer, M., Nordqvist, A., Ouchterlony, F., Nyberg, U., & Furtney, J. (2013). Burden movement in confined drift wall blasting tests studied at the lkab kiruna slc mine. *Rock Fragmentation by Blasting: 10th International Symposium on Rock Fragmentation by Blasting (Fragblast 10)*, 373–383.

Zhang, Z.-X. (2016). *Rock fracture and blasting: Theory and applications*. Butterworth-Heinemann.

Zhou, J., Chen, C., Armaghani, D., & Ma, S. (2022). Developing a hybrid model of information entropy and unascertained measurement theory for evaluation of the excavatability in rock mass. *Engineering with Computers*, *38*, 247–270. https://doi.org/10.1007/s00366-020-01053-4

Zhou, J., & Li, X. (2012). Integrating unascertained measurement and information entropy theory to assess blastability of rock mass. *Journal of Central South University*, *19*, 1953–1960. https://doi.org/10.1007/s11771-012-1231-y

Zhou, Z., Cui, C., Xin, C., & Wang, P. (2024). Blastability evaluation for rock mass: Review and new tendency. *Bulletin of Engineering Geology and the Environment*, *83*(12), 517.

A

BI Scoring Tables

Table 14: Refined scoring ranges for Lilly's BI input parameters.

Parameter	Description / Classification	Score
RMD	BRQD < 25% (friable)	10
	BRQD 25–50% (moderate)	20
	BRQD 50–65% (moderately competent)	30
	BRQD 65–80% (competent)	40
	BRQD > 80% (massive, intact)	50
JPS	Very close spacing (< 5 cm)	10
	Close spacing (5–20 cm)	15
	Moderate spacing (20–60 cm)	30
	Wide spacing (60–200 cm)	45
	Very wide spacing (> 200 cm)	50
JPO	Joints sub-horizontal / parallel to face	10
	Joints dipping out of face	20
	Joints striking normal to face	30
	Joints dipping into face	40
RDI	Calculated from density (ρ) as $RDI = 25 \cdot \rho - 50$	—
H	Calculated from UCS as $H = 0.05 \cdot UCS$	—

Table 15: Fuzzy input variable configuration for the Fuzzy Blastability Index (FBI). Triangular membership functions were used in all cases. SGI and UCS use site-specific minimum and maximum values from laboratory testing.

Variable	Unit	Range	Fuzzy Terms	MF Type
RMD	—	10–50	Very Low, Low, Medium, High, Very High	Uniform
JPS (Spacing Score)	—	10–50	Very Close, Close, Moderate, Wide, Very Wide	Uniform
JPO (Orientation)	—	10–40	Very Favourable, Favourable, Neutral, Unfavourable, Very Unfavourable	Uniform
RDI	—	16.03–36.67	Very Light, Light, Medium, Dense, Very Dense	Data-driven
UCS	—	2.4-20.95	Very Soft, Soft, Medium, Hard, Very Hard	Data-driven

B

UCS Test Results

A. Detailed Test Results

Table 16: Summary of UCS test results, dynamic properties, and elastic parameters by sample (corrected UCS values)

Sample	Rock Type	UCS (MPa)	E (GPa)	ν [-]	R^2	Density (kg/m^3)	Vs / Vp (m/s)
SERQ6015_6025	SERQ	129	46	0.037	0.992	2711	2868 / 4136
SERQ6105_6120	SERQ	97	55	0.049	0.992	2713	3100 / 4502
SERQ6365_6380	SERQ	65	34	0.091	0.992	2747	2369 / 3532
SERQ6755_677	SERQ	119	47	0.064	0.997	2837	2781 / 4073
SERQ mean ± std		103 ± 27	46 ± 9				
AND131_13115	AND	130	50	0.127	0.992	2839	2807 / 4296
AND1353_1354	AND	354	130	0.139	0.979	2977	4384 / 6769*
AND136_13615	AND	88	44	0.067	0.993	2818	2703 / 3968
AND60_6015	AND	160	70	0.066	0.995	3011	3309 / 4853
AND6875_689	AND	182	75	0.206	0.917	2965	3232 / 5314
AND mean ± std		183 ± 96	74 ± 34				
VOLCL1023_10245	VOLCL	107	48	0.064	0.998	2729	2867 / 4200
VOLCL1277_12785	VOLCL	143	48	0.090	0.994	2929	2739 / 4081
VOLCL7445_746	VOLCL	68	211	0.071	0.956	2767	5964 / 8775*
VOLCL843_844	VOLCL	87	47	0.098	0.996	2753	2773 / 4154
VOLCL mean ± std		101 ± 33	89 ± 82				
ANQTZ1084_1085	ANQTZ	170	73	0.081	0.999	2865	3435 / 5088
ANQTZ13185_132	ANQTZ	48	40	0.067	0.999	2872	2567 / 3767
ANQTZ1831_1833	ANQTZ	208	111	0.119	0.999	3318	3860 / 5870
ANQTZ22195_2221	ANQTZ	341	95	0.110	1.000	2825	3892 / 5879
ANQTZ224_22415	ANQTZ	369	97	0.099	1.000	2801	3976 / 5960
ANQTZ mean ± std		227 ± 121	83 ± 28				
BREC15705_15715	BREC	307	100	0.087	0.999	3111	3843 / 5714
BREC19345_1936	BREC	120	69	0.097	1.000	2804	3340 / 5001
BREC1947_19485	BREC	95	47	0.112	0.999	2805	2740 / 4146
BREC2133_21345	BREC	105	103	0.093	1.000	3198	3847 / 5741
BREC7655_767	BREC	175	108	0.084	0.999	3467	3788 / 5620
BREC935_9365	BREC	419	91	0.076	0.999	2866	3838 / 5667
BREC mean ± std		204 ± 109	86 ± 24				
QTZFP17055_1707	QTZFP	208	67	0.076	1.000	2709	3399 / 5018
QTZFP1764_17655	QTZFP	89	58	0.145	1.000	2648	3096 / 4805
QTZFP178_17815	QTZFP	84	52	0.092	0.999	2693	2977 / 4442
QTZFP186_18615	QTZFP	198	70	0.055	1.000	2646	3550 / 5173
QTZFP9215_923	QTZFP	399	83	0.050	1.000	2641	3859 / 5608
QTZFP mean ± std		196 ± 114	66 ± 12				

* Extreme outlier values flagged based on unrealistic high wave velocities or modulus.

B. Photographs of Broken Specimen

B.1. Sericite Quartzite

(a) SERQ6105_6120

(b) SERQ6015_6025

(c) SERQ6365_6380

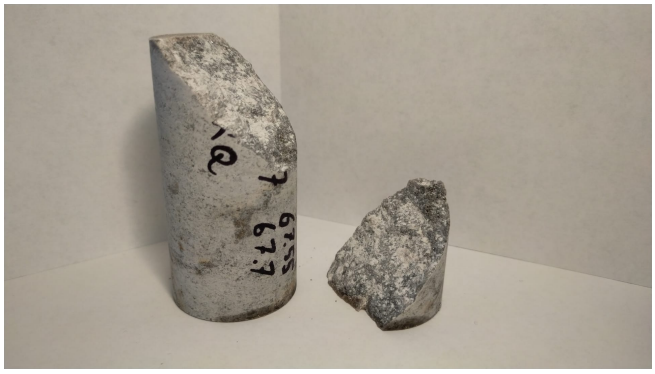

(d) SERQ6755_677

B.2. Andesite

(a) AND131_13115

(b) AND1353_1354

(c) AND136_13615

(d) AND600_6015

(e) AND6875_689

B.3. Volcaniclastic

(a) VOLCL1023_10245

(b) VOLCL1277_12785

(c) VOLCL7445_746

(d) VOLCL843_844

B.4. Andalusite Quartzite

(a) ANQTZ1084_1085

(b) ANQTZ13185_1320

(c) ANQTZ1831_1833

(d) ANQTZ22195_2221

(e) ANQTZ224_22415

B.5. Breccia

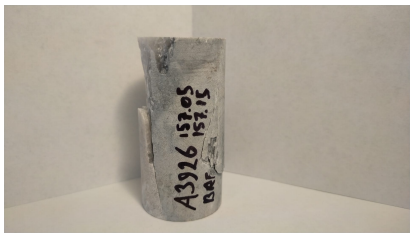

(a) BREC15705_15715

(b) BREC19345_1936

(c) BREC1947_19485

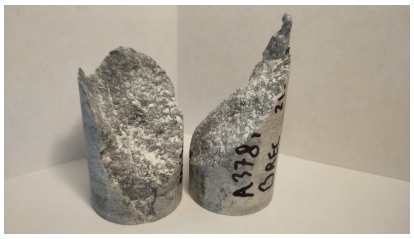

(d) BREC2133_21345

(e) BREC7655_767

(f) BREC935_9365

B.6. Quartzite Feldspar Porphyry

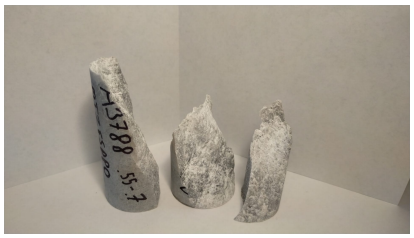

(a) QTZFP17055_1707

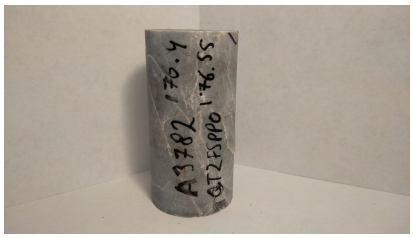

(b) QTZFP1764_17655

(c) QTZFP178_17815

(d) QTZFP186_18615

(e) QTZFP9215_923

C

Rule Base Constraints

To ensure geological consistency in the FIS for the FBI, a series of plausibility constraints were applied during rule generation. These constraints exclude combinations of input parameters deemed structurally or mechanically contradictory based on standard principles handpicked by the author.

1. **RMD =** ***very low*** and **JPS =** ***very wide***
   A rock mass with a very low RMD score indicates highly fractured or poor-quality rock. Such a condition is inconsistent with widely spaced joints, which typically occur in more intact rock masses.
2. **RMD =** ***very high*** and **JPS =** ***very close***
   Conversely, a very high RMD score suggests intact, high-quality rock, which is unlikely to exhibit closely spaced jointing. This combination is geotechnically contradictory.
3. **UCS =** ***very soft*** and **RDI =** ***very dense***
   Very soft rocks are typically weathered, porous, or otherwise structurally degraded. It is unlikely for such materials to exhibit high density. However, this constraint should be treated with some caution, given that UCS values may vary depending on sample integrity and testing method.
4. **UCS =** ***very hard*** and **RDI =** ***very light***
   Dense rocks are generally correlated with higher strength. While it's rare for very lightweight rocks to exhibit very high UCS, exceptions can occur due to unique mineralogy or internal cohesion. Therefore, this rule was also applied conservatively.

Of course, rare but possible geological exceptions exist, they may be addressed via expert judgment on a case-by-case basis, but not considered here.

D

Cross-hole Consistency

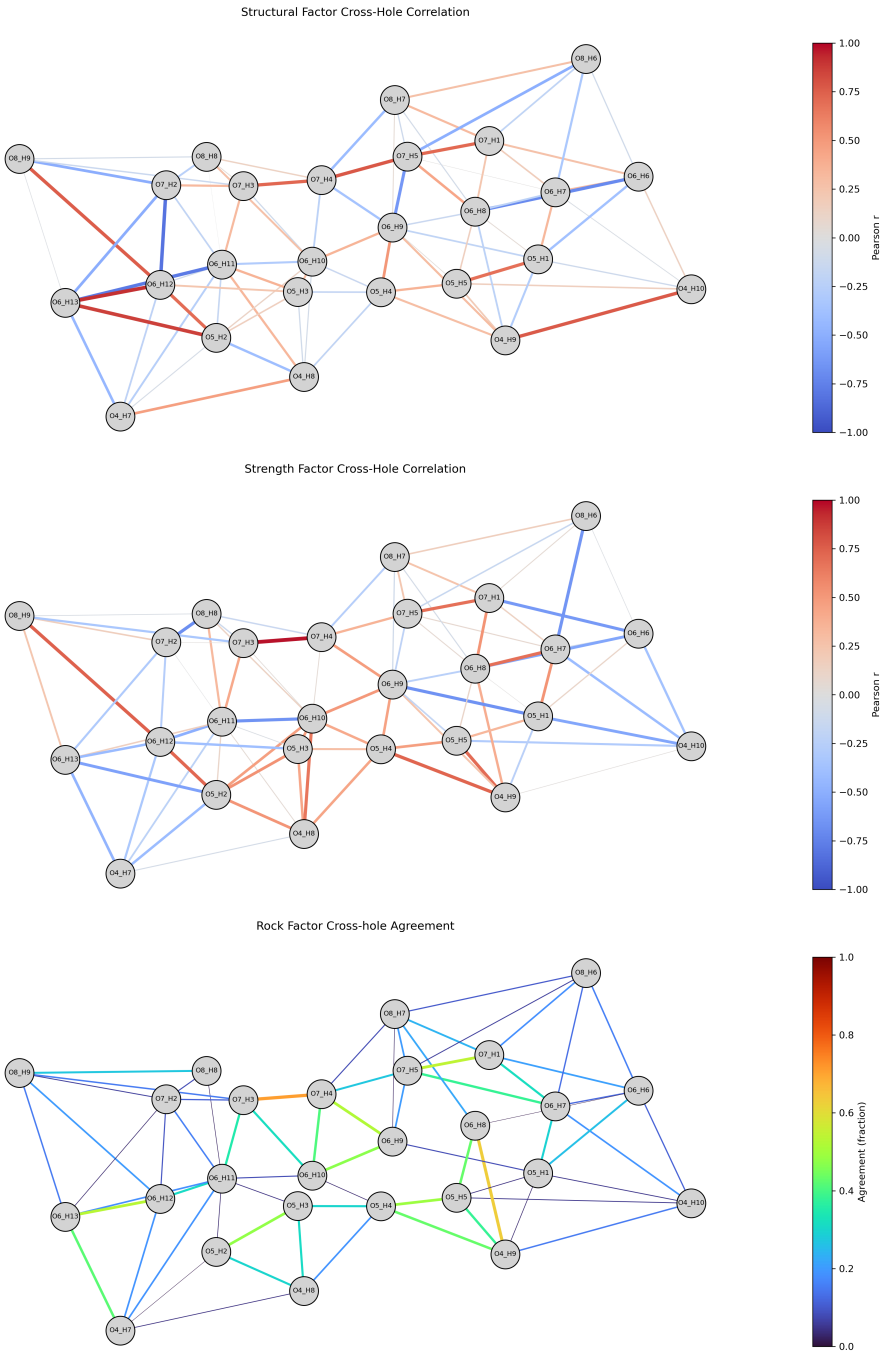

Figure 53: Cross-hole similarity networks for the derived SuF, SeF and RF (S7a_642).

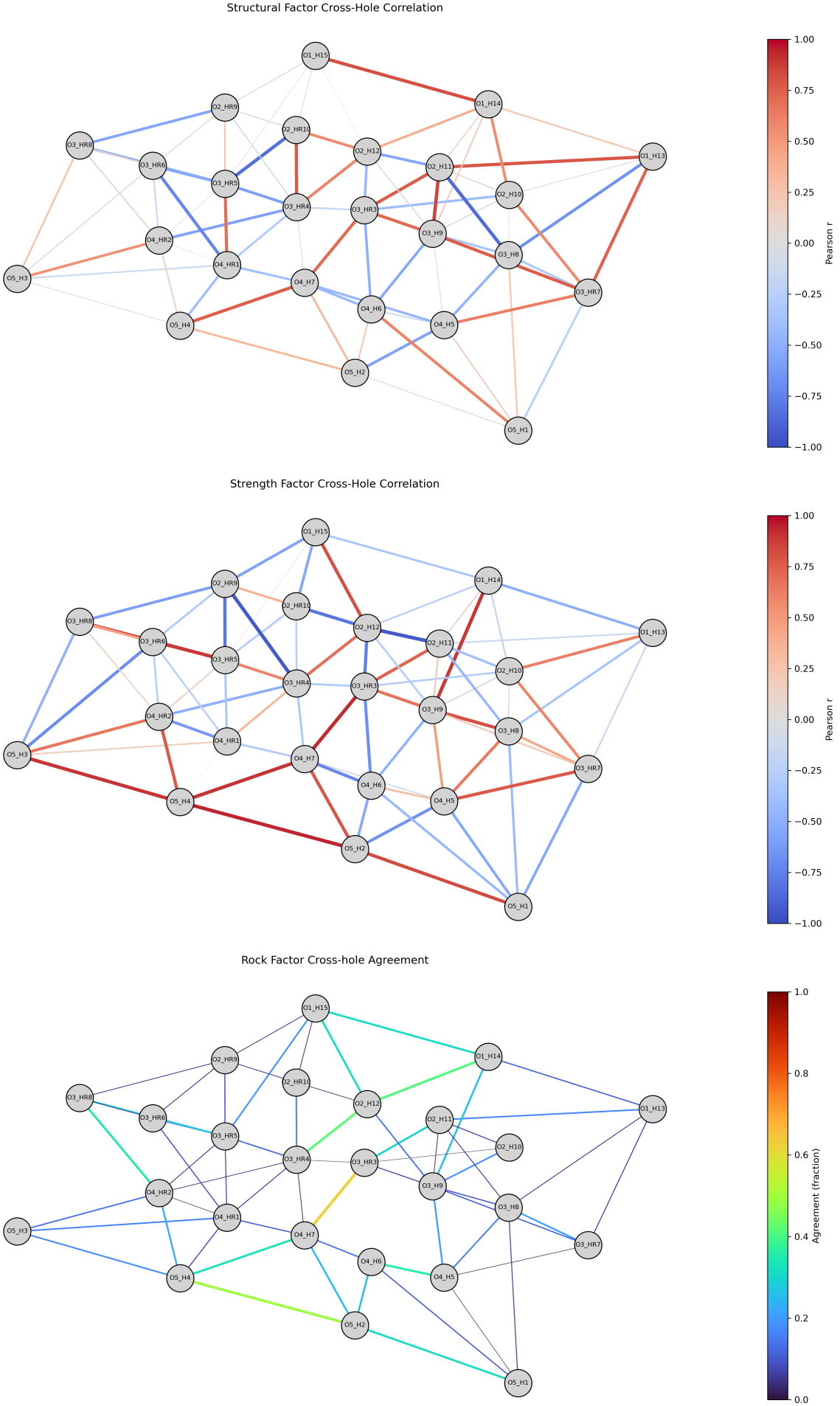

Figure 54: Cross-hole similarity networks for the derived SuF, SeF and RF(S0_612).

E

Python Code

Note: The code formatted as shown here was cleaned and structured with the help of an AI-assisted formatting to improve the interpretability for other users. The code was rerun to verify the correct alignment with the original code.

A. BI & FBI

BI Computation

```python
import numpy as np
import pandas as pd

def assign_rmd_scaled(brqd_mean):
    if brqd_mean < 25:
        return 10
    elif brqd_mean < 50:
        return 20
    elif brqd_mean < 65:
        return 30
    elif brqd_mean < 80:
        return 40
    else:
        return 50

def compute_weighted_jps(spacing_dist):
    scores = {'Very Close': 10, 'Close': 15, 'Moderate': 30, 'Wide': 45, 'Very Wide': 50}
    total = sum(spacing_dist.values())
    if total == 0:
        return None
    weighted_avg = sum(scores.get(k, 0) * v for k, v in spacing_dist.items()) / total
    return min(scores.values(), key=lambda x: abs(x - weighted_avg))

def calculate_rdi(density):
    return round((density / 1000) * 25 - 50, 2)

def assign_h(ucs):
    return round(0.05 * ucs, 2)

def calculate_bi(rmd, jps, rdi, h, jpo=25):
    return 0.5 * round(rmd + jps + rdi + h + jpo, 2)

def compute_bi(df, spacing_lookup, properties_lookup):
    df = df.copy()
    df['RMD'] = df['BRQD_mean'].apply(assign_rmd_scaled)
    df['JPS'] = df['RockType'].map(lambda rt: compute_weighted_jps(spacing_lookup.get(rt, {})))
    df['UCS'] = df['RockType'].map(lambda rt: np.mean(properties_lookup.get(rt, {}).get('UCS', np.nan)))
    df['Density'] = df['RockType'].map(lambda rt: np.mean(properties_lookup.get(rt, {}).get('Density', np
        .nan)))
    df['RDI'] = df['Density'].apply(lambda d: calculate_rdi(d) if pd.notnull(d) else None)
    df['H'] = df['UCS'].apply(lambda u: assign_h(u) if pd.notnull(u) else None)
    df['BI'] = df.apply(lambda row: calculate_bi(row['RMD'], row['JPS'], row['RDI'], row['H']) if pd.
        notnull(row['H']) else None, axis=1)
    return df
```

FBI Computation

```python
import itertools
from collections import defaultdict

def create_triangular_mfs(var_range, labels):
    min_val, max_val = var_range
    step = (max_val - min_val) / (len(labels) - 1)
    mfs = {}
    for i, label in enumerate(labels):
        if i == 0:
            mfs[label] = [min_val, min_val, min_val + step]
        elif i == len(labels) - 1:
            mfs[label] = [max_val - step, max_val, max_val]
        else:
            center = min_val + i * step
            mfs[label] = [center - step, center, center + step]
    return mfs

def percentiles_to_mfs(p_vals, labels):
    return {
        labels[0]: [p_vals[0], p_vals[0], p_vals[1]],
        labels[1]: [p_vals[0], p_vals[1], p_vals[2]],
        labels[2]: [p_vals[1], p_vals[2], p_vals[3]],
        labels[3]: [p_vals[2], p_vals[3], p_vals[4]],
        labels[4]: [p_vals[3], p_vals[4], p_vals[4]],
    }

def fuzzify(value, mf):
    a, b, c = mf
    if value < a or value > c:
        return 0.0
    elif value <= b:
        return (value - a) / (b - a) if b != a else 1.0
    else:
        return (c - value) / (c - b) if c != b else 1.0

def is_plausible(combo):
    rmd, jps, jpo, rdi, ucs = combo['RMD'], combo['JPS'], combo['JPO'], combo['RDI'], combo['UCS']
    if rmd == 'very_low' and jps == 'very_wide':
        return False
    if rmd == 'very_high' and jps == 'very_close':
        return False
    if ucs == 'very_soft' and rdi == 'very_dense':
        return False
    if ucs == 'very_hard' and rdi == 'very_light':
        return False
    return True

def infer_output_term(combo, weights):
    score_map = {'very_low': 0, 'low': 1, 'medium': 2, 'high': 3, 'very_high': 4}
    numeric = [score_map[t] * w for t, w in zip(combo, weights)]
    avg = sum(numeric) / sum(weights)
    if avg <= 0.8: return 'very_low'
    elif avg <= 1.6: return 'low'
    elif avg <= 2.4: return 'medium'
    elif avg <= 3.2: return 'high'
    else: return 'very_high'

def evaluate_fbi(inputs, config, debug=False):
    fuzzified_inputs = {}
    for var, val in inputs.items():
        val = val * 0.05 if var == 'UCS' else val
        fuzzified_inputs[var] = {label: fuzzify(val, mf) for label, mf in config['input_mfs'][var].items
            ()}

    output_activations = defaultdict(float)
    for rule in config['rules']:
        strength = min(fuzzified_inputs[var].get(term, 0.0) for var, term in rule['if'].items())
        output_activations[rule['then']] = max(output_activations[rule['then']], strength)

    numerator = sum(config['output_terms'][term] * strength for term, strength in output_activations.
        items())
    denominator = sum(output_activations.values())
    return round(numerator / denominator, 2) if denominator != 0 else None
```

B. MWD Processing Pipeline

```python
import numpy as np
import pandas as pd
from sklearn.decomposition import PCA

__all__ = ["make_master", "strip_rod_pauses", "depth_normalise",
           "add_navarro_factors", "build_factors"]

def make_master(df_raw: pd.DataFrame,
                pct_clip: tuple[int, int] = (1, 99),
                pause_s: int | None = 180,
                depth_jump_m: float = 5.0,
                rod_tol: float = 1e-3,
                verbose: bool = True) -> pd.DataFrame:
    counts = {}
    n0 = len(df_raw)
    df = df_raw.sort_values(["Hole", "DepthTag"]).copy()
    counts["initial"] = n0

    if "TimeTag" in df.columns and pause_s is not None:
        dt = df.groupby("Hole")["TimeTag"].diff().dt.total_seconds().fillna(0)
        df = df.loc[dt.le(pause_s)]
    counts["pause_removed"] = n0 - len(df); n1 = len(df)

    dz = df.groupby("Hole")["DepthTag"].diff().abs().fillna(0)
    df = df.loc[dz.le(depth_jump_m)]
    counts["depth_jump_removed"] = n1 - len(df); n2 = len(df)

    mask = df["PenetrRate"].abs() > rod_tol
    df = df.loc[mask]
    counts["rod_removed"] = n2 - len(df)

    phys_cols = ["PenetrRate","PercPressure","FeedPressure","RotPressure","DampPressure","FlushPressure"]
    for c in phys_cols:
        vals = df[c].dropna()
        if len(vals) < 5:
            continue
        lo, hi = np.percentile(vals, pct_clip)
        before = len(df)
        df = df[df[c].between(lo, hi) | df[c].isna()]
        counts[f"clip_{c}"] = before - len(df)

    before = len(df)
    df = (df.drop_duplicates(["Hole","DepthTag"])
            .sort_values(["Hole","DepthTag"])
            .reset_index(drop=True))
    counts["duplicates_removed"] = before - len(df)

    if "Rig" not in df.columns:
        df["Rig"] = "R1"

    if verbose:
        print("make_master filtering summary:")
        for k, v in counts.items():
            print(f"  {k:>22}: {v} rows")
    return df

def strip_rod_pauses(df: pd.DataFrame,
                     v_col: str = "PenetrRate",
                     zero_tol: float = 1e-3,
                     pad: int = 0) -> pd.DataFrame:
    mask = df[v_col].abs() > zero_tol
    if pad:
        bad = (~mask).rolling(pad*2+1, center=True, min_periods=1).max().astype(bool)
        mask &= ~bad
    return df.loc[mask]

def depth_normalise(df_in: pd.DataFrame, degree: int = 2) -> pd.DataFrame:
    """Subtract per-rig polynomial trend vs depth; add *Norm columns."""
    df = df_in.copy()
    rename = {"RotPressure":"RP","PenetrRate":"PR","PercPressure":"PP","FeedPressure":"FP","FlushPressure
        ":"FLP","DampPressure":"DP"}
    for col, _ in rename.items():
        norm_col = f"{col}Norm"
```

```
        df[norm_col] = np.nan
        for rig, g in df.groupby("Rig"):
            g = g[["DepthTag", col]].dropna()
            if len(g) <= degree: continue
            poly = np.poly1d(np.polyfit(g["DepthTag"], g[col], degree))
            m = (df["Rig"]==rig)
            df.loc[m, norm_col] = df.loc[m, col] - poly(df.loc[m,"DepthTag"]) + poly(0)
    return df

def _rolling_variability(values: np.ndarray, depths: np.ndarray, half_m: float) -> np.ndarray:
    out = np.empty_like(values, dtype=float)
    for i, z in enumerate(depths):
        win = (depths >= z-half_m) & (depths <= z+half_m)
        x = values[win]
        out[i] = np.abs(x - np.nanmean(x)).sum() if x.size else np.nan
    return out

def _zscore(s: pd.Series) -> pd.Series:
    return (s - s.mean()) / s.std()  # pandas ddof=1

def _run_pca(df: pd.DataFrame, cols: list[str], out_col: str) -> None:
    X = df[cols].dropna()
    if X.empty:
        df[out_col] = np.nan
        return
    X_std = (X - X.mean()) / X.std()
    pca = PCA(n_components=2)
    pcs = pca.fit_transform(X_std)
    df.loc[X.index, out_col] = pcs[:, 0]

def add_navarro_factors(df_norm: pd.DataFrame, win_m: float = 0.6, smooth_n: int = 5) -> pd.DataFrame:
    df = df_norm.copy()
    for hole, g in df.groupby("Hole"):
        idx = g.index; z = g["DepthTag"].to_numpy()
        df.loc[idx, "PRvar"] = _rolling_variability(g["PenetrRateNorm"].to_numpy(), z, win_m)
        df.loc[idx, "RPvar"] = _rolling_variability(g["RotPressureNorm"].to_numpy(), z, win_m)
        df.loc[idx, "FPvar"] = _rolling_variability(g.get("FeedPressureNorm", pd.Series(index=idx)).
            to_numpy() if "FeedPressureNorm" in g else np.full(len(idx), np.nan), z, win_m)

    for v in ("PRvar","RPvar","FPvar"):
        df[f"{v}_z"] = _zscore(df[v])
    df["DI"] = np.sqrt(0.5*df["PRvar_z"]**2 + 0.5*df["RPvar_z"]**2)

    _run_pca(df, ["PRvar_z","RPvar_z","FeedPressure","DI","PercPressureNorm"], "Structural_raw")
    _run_pca(df, ["PenetrRateNorm","RotPressureNorm","FeedPressure","PercPressureNorm"], "Strength_raw")

    for col in ("Structural_raw","Strength_raw"):
        df[f"{col}_smooth"] = (df.sort_values(["Hole","DepthTag"])
                               .groupby("Hole")[col]
                               .transform(lambda s: s.rolling(smooth_n, center=True, min_periods=1).
                                   mean()))
    return df.rename(columns={"Structural_raw_smooth":"StructuralFactor",
                              "Strength_raw_smooth":"StrengthFactor"})

# PIPELINE
def build_factors(combined_mwd: pd.DataFrame,
                  pct_clip: tuple[int,int]=(1,99),
                  pause_s: int | None = 180,
                  depth_jump_m: float = 5.0,
                  degree: int = 2,
                  win_m: float = 0.6,
                  smooth_n: int = 3) -> pd.DataFrame:
    df = make_master(combined_mwd, pct_clip, pause_s, depth_jump_m)
    df = depth_normalise(df, degree)
    df = add_navarro_factors(df, win_m, smooth_n)
    core = ["PenetrRateNorm","RotPressureNorm","FeedPressureNorm","PRvar_z","RPvar_z","FPvar_z"]
    return df.dropna(subset=core, how="all").reset_index(drop=True)
```

F

Geologic Unit Percentage Per Stope

Handle	Breccia	Porphyry	Topaz Fragment	Andelusite Quartzite	Chlorite Quartzite	Dacite	Sericite Quartzite	Volcaniclastic	Andesite	Sericite Schist	Siltstone	Talc Schist	Clastic Sediment
1388C59	90.35	4.03	5.62	0.00	0.00	0.00	0.00	0.00	0.00	0.00	0.00	0.00	0.00
1388C61	3.55	82.85	0.00	0.00	1.62	0.00	11.93	0.06	0.00	0.00	0.00	0.00	0.00
1388CA2	0.00	43.29	0.00	0.00	0.00	0.00	52.05	0.00	4.66	0.00	0.00	0.00	0.00
1388CA9	4.63	81.04	11.08	0.00	0.00	0.00	0.00	0.84	2.42	0.00	0.00	0.00	0.00
1388C96	0.00	19.95	0.00	74.67	0.00	0.00	5.38	0.00	0.00	0.00	0.00	0.00	0.00
1388CD9	56.02	38.71	0.00	0.00	0.00	0.00	0.00	0.09	5.18	0.00	0.00	0.00	0.00
13D1818	0.00	25.72	0.00	0.00	0.00	0.00	71.37	0.73	2.18	0.00	0.00	0.00	0.00
1388CAE	0.18	31.11	0.00	51.60	0.00	0.00	12.25	3.89	0.97	0.00	0.00	0.00	0.00
1388CE2	0.00	81.24	0.00	0.00	0.00	0.00	0.00	18.76	0.00	0.00	0.00	0.00	0.00
1388C6F	28.31	28.73	15.88	24.26	0.00	0.00	0.06	2.75	0.00	0.00	0.00	0.00	0.00
1388C58	19.82	22.10	0.00	0.00	0.00	0.00	0.00	2.17	55.91	0.00	0.00	0.00	0.00
1388CD2	0.00	16.79	0.00	8.38	0.00	0.00	28.60	4.48	12.62	29.13	0.00	0.00	0.00
1388C51	0.00	7.33	0.00	0.00	0.00	0.00	0.00	92.67	0.00	0.00	0.00	0.00	0.00
1388CA3	0.00	54.43	0.00	0.00	0.00	0.00	35.15	10.42	0.00	0.00	0.00	0.00	0.00
1388CD4	0.00	98.94	0.00	0.00	0.00	0.00	0.13	0.00	0.94	0.00	0.00	0.00	0.00
1388CC3	0.00	58.09	12.61	0.00	0.00	0.00	0.00	29.30	0.00	0.00	0.00	0.00	0.00
1388CDD	0.00	85.63	0.00	0.00	0.00	0.00	14.35	0.02	0.00	0.00	0.00	0.00	0.00
1388C85	9.02	42.45	0.00	24.20	0.00	0.00	2.67	21.66	0.00	0.00	0.00	0.00	0.00
1388C4B	10.52	64.16	25.32	0.00	0.00	0.00	0.00	0.00	0.00	0.00	0.00	0.00	0.00
1388CAF	0.00	0.00	0.00	0.00	0.00	0.00	91.11	0.00	8.89	0.00	0.00	0.00	0.00
1388CC6	0.00	13.24	1.48	0.00	0.00	0.00	7.27	78.00	0.00	0.00	0.00	0.00	0.00
1388CBF	0.00	58.25	7.04	0.00	0.00	0.00	0.01	34.66	0.05	0.00	0.00	0.00	0.00
1388CA5	54.71	13.34	0.35	4.54	0.00	0.00	1.95	25.11	0.00	0.00	0.00	0.00	0.00
1388C9F	0.00	29.14	0.01	0.00	0.08	0.00	57.85	6.77	6.15	0.00	0.00	0.00	0.00
1388C93	0.00	0.00	0.00	0.00	0.00	0.00	25.58	70.44	3.98	0.00	0.00	0.00	0.00
1388CE1	0.00	36.53	0.00	0.00	0.00	0.00	51.83	11.64	0.00	0.00	0.00	0.00	0.00
1388CDF	34.26	29.34	0.00	0.00	0.00	0.00	19.33	17.08	0.00	0.00	0.00	0.00	0.00
1388CE6	0.00	37.01	12.57	0.00	0.00	0.00	0.00	50.42	0.00	0.00	0.00	0.00	0.00
1388CB0	0.00	27.41	0.00	0.00	0.00	0.00	62.51	0.00	10.02	0.06	0.00	0.00	0.00
1388C88	34.42	60.00	0.00	0.00	0.00	0.00	5.58	0.00	0.00	0.00	0.00	0.00	0.00
13D181D	0.00	10.31	0.00	1.36	0.00	0.00	88.33	0.00	0.00	0.00	0.00	0.00	0.00
1388C99	0.00	51.03	4.67	11.54	0.00	0.00	11.42	21.34	0.00	0.00	0.00	0.00	0.00
13D1819	0.00	25.77	0.00	0.00	1.48	0.00	66.69	0.00	6.06	0.00	0.00	0.00	0.00
1388C8C	0.00	34.41	0.00	9.51	0.00	0.00	17.08	38.24	0.76	0.00	0.00	0.00	0.00

Continued on next page

Handle	Breccia	Porphyry	Topaz Fragment	Andelusite Quartzite	Chlorite Quartzite	Dacite	Sericite Quartzite	Volcaniclastic	Andesite	Sericite Schist	Siltstone	Talc Schist	Clastic Sediment
1388C69	0.00	46.52	0.00	0.00	0.00	0.03	6.98	42.40	4.01	0.00	0.06	0.00	0.00
1388C71	0.78	66.27	0.00	1.48	0.00	0.00	0.15	32.41	0.00	0.00	0.00	0.00	0.00
1388C6C	0.00	81.54	0.00	0.00	0.00	0.00	0.00	18.46	0.00	0.00	0.00	0.00	0.00
1388C90	13.76	65.21	0.00	0.00	0.00	0.00	2.44	15.75	0.00	2.83	0.00	0.00	0.00
1388CB8	0.00	4.12	0.00	0.00	0.00	0.00	94.88	0.00	0.28	0.00	0.00	0.72	0.00
1388C81	1.72	30.09	0.00	0.00	0.00	0.00	0.00	0.00	68.19	0.00	0.00	0.00	0.00
1388CA6	0.00	78.17	15.48	0.00	0.00	0.00	0.00	0.00	6.35	0.00	0.00	0.00	0.00
1388C7F	0.00	83.15	0.00	0.00	0.00	0.00	0.21	16.64	0.00	0.00	0.00	0.00	0.00
1388CA7	0.00	0.00	0.00	2.46	0.66	0.00	89.69	0.00	7.19	0.00	0.00	0.00	0.00
1388CB7	5.58	44.72	0.00	0.00	0.00	0.00	0.00	49.70	0.00	0.00	0.00	0.00	0.00
1388CD7	0.00	62.27	0.84	14.56	0.00	0.00	14.14	6.14	2.05	0.00	0.00	0.00	0.00
1388CD6	0.24	3.61	0.00	1.13	0.00	0.00	74.99	18.35	1.68	0.00	0.00	0.00	0.00
1388CD5	49.70	27.74	0.00	0.00	0.00	0.00	17.33	5.22	0.00	0.00	0.00	0.00	0.00
1388C52	0.00	15.88	0.00	0.00	0.00	0.00	62.73	21.39	0.00	0.00	0.00	0.00	0.00
1388C64	0.00	71.15	0.00	0.00	0.00	0.00	28.85	0.00	0.00	0.00	0.00	0.00	0.00
14EE6F9	0.09	93.93	0.00	0.00	0.00	0.00	0.00	0.00	5.98	0.00	0.00	0.00	0.00
1388CB5	24.23	64.80	7.96	0.08	0.00	0.00	0.00	2.93	0.00	0.00	0.00	0.00	0.00
1388CDE	0.00	2.01	0.00	50.36	0.00	0.00	46.85	0.78	0.00	0.00	0.00	0.00	0.00
13D180D	0.00	94.78	0.00	0.00	0.00	0.00	5.22	0.00	0.00	0.00	0.00	0.00	0.00
1388CE5	0.00	63.27	2.16	0.00	0.00	0.00	24.85	9.71	0.00	0.00	0.00	0.00	0.00
1388C73	0.00	38.16	0.00	0.00	0.00	0.00	0.35	58.72	2.77	0.00	0.00	0.00	0.00
1388C75	64.02	35.63	0.00	0.00	0.00	0.00	0.35	0.00	0.00	0.00	0.00	0.00	0.00
1388CC8	0.00	80.23	0.00	0.00	0.00	0.00	9.68	0.00	10.09	0.00	0.00	0.00	0.00
1388C5F	0.00	42.04	0.00	0.00	0.00	0.00	0.00	57.96	0.00	0.00	0.00	0.00	0.00
1388C72	0.00	19.28	0.00	0.00	0.00	0.00	3.11	54.09	23.51	0.00	0.00	0.00	0.00
1388C5A	3.30	66.84	16.16	8.23	0.00	0.20	0.61	3.45	1.20	0.00	0.00	0.00	0.00
1388C4F	24.63	25.31	0.25	0.00	0.41	0.00	12.39	23.52	13.50	0.00	0.00	0.00	0.00
1388C98	3.20	36.54	0.00	2.71	3.81	0.00	39.14	14.59	0.00	0.00	0.00	0.00	0.00
1388C67	8.96	91.04	0.00	0.00	0.00	0.00	0.00	0.00	0.00	0.00	0.00	0.00	0.00
1388CBC	0.20	1.19	0.00	27.67	0.00	0.00	38.58	32.16	0.18	0.01	0.00	0.00	0.00
1388C9B	42.56	57.44	0.00	0.00	0.00	0.00	0.00	0.00	0.00	0.00	0.00	0.00	0.00
1388C4C	0.00	0.00	0.00	0.00	0.00	5.99	81.09	7.35	5.57	0.00	0.00	0.00	0.00
1388CCB	0.00	9.01	0.00	11.91	0.00	0.00	38.45	40.64	0.00	0.00	0.00	0.00	0.00
1388C82	0.41	33.62	0.00	0.00	0.00	0.00	0.75	12.12	53.09	0.00	0.00	0.00	0.00
1388C62	0.00	95.54	0.00	0.00	0.00	0.00	0.00	0.00	4.46	0.00	0.00	0.00	0.00
1388C4D	0.00	9.53	0.00	13.34	0.00	0.00	42.36	34.76	0.00	0.00	0.00	0.00	0.00
13D181A	0.00	36.07	0.00	0.00	0.00	0.00	61.09	0.00	2.84	0.00	0.00	0.00	0.00
1388C5B	0.00	86.65	0.00	0.00	0.00	0.00	10.16	3.18	0.00	0.00	0.00	0.00	0.00
1388C94	0.00	47.44	0.00	0.00	0.00	11.85	5.77	34.93	0.00	0.00	0.00	0.00	0.00
1388C5D	3.39	95.27	0.00	0.00	0.00	0.00	0.00	1.34	0.00	0.00	0.00	0.00	0.00
1388C66	0.36	4.63	0.00	0.00	0.00	0.00	0.00	58.90	36.11	0.00	0.00	0.00	0.00
1388C9A	0.00	3.68	0.00	30.01	0.00	0.00	66.25	0.00	0.05	0.00	0.00	0.00	0.00
1388C97	0.00	18.08	0.00	0.00	0.00	2.30	63.01	5.15	11.45	0.00	0.00	0.00	0.00
1388C6B	0.00	0.00	0.00	78.10	0.00	0.00	21.90	0.00	0.00	0.00	0.00	0.00	0.00
1388CB4	23.39	39.96	0.00	9.03	0.00	0.00	21.32	5.56	0.00	0.00	0.00	0.00	0.73
1388CB9	0.00	56.29	0.00	0.00	0.00	0.81	0.00	23.52	18.92	0.00	0.40	0.00	0.06
1388CB2	0.00	84.18	0.00	0.00	0.00	0.00	0.00	15.82	0.00	0.00	0.00	0.00	0.00
1388CC7	21.98	59.27	0.00	0.00	0.00	0.00	0.11	18.64	0.00	0.00	0.00	0.00	0.00
1388C65	1.42	94.97	2.26	0.00	0.00	0.00	0.00	1.36	0.00	0.00	0.00	0.00	0.00

Continued on next page

Handle	Breccia	Porphyry	Topaz Fragment	Andelusite Quartzite	Chlorite Quartzite	Dacite	Sericite Quartzite	Volcaniclastic	Andesite	Sericite Schist	Siltstone	Talc Schist	Clastic Sediment
13D180A	0.00	19.94	22.52	4.63	0.00	0.00	52.91	0.00	0.00	0.00	0.00	0.00	0.00
13D181C	0.00	0.00	0.00	0.00	0.00	0.00	100.00	0.00	0.00	0.00	0.00	0.00	0.00
1388CA1	0.42	86.12	0.00	0.00	0.00	0.00	0.00	7.17	6.30	0.00	0.00	0.00	0.00
1388CB3	0.00	0.18	0.00	86.76	0.00	0.00	13.07	0.00	0.00	0.00	0.00	0.00	0.00
1388CBE	0.99	40.65	0.00	27.46	0.00	0.00	30.90	0.00	0.00	0.00	0.00	0.00	0.00
1388CCF	0.00	30.70	0.00	0.00	0.00	0.00	12.33	56.97	0.00	0.00	0.00	0.00	0.00
1388CE3	0.00	4.22	0.00	0.00	0.11	0.00	63.99	0.00	6.32	0.00	0.00	25.36	0.00
1388CDA	0.00	86.25	2.39	0.00	0.00	0.00	11.36	0.00	0.00	0.00	0.00	0.00	0.00
1388C6A	0.00	22.88	0.00	0.00	0.00	0.00	0.72	70.27	6.13	0.00	0.00	0.00	0.00
1388C79	0.08	58.93	0.00	21.47	0.00	0.00	18.75	0.77	0.00	0.00	0.00	0.00	0.00
13D1817	0.00	100.00	0.00	0.00	0.00	0.00	0.00	0.00	0.00	0.00	0.00	0.00	0.00
1388C91	0.00	2.60	0.00	0.00	0.00	0.00	66.60	30.81	0.00	0.00	0.00	0.00	0.00
13D1835	0.00	0.00	0.00	0.00	0.00	0.00	100.00	0.00	0.00	0.00	0.00	0.00	0.00
1388C54	0.00	65.85	0.00	0.00	0.00	0.00	34.15	0.00	0.00	0.00	0.00	0.00	0.00
1388C9D	8.82	62.31	3.28	0.00	0.00	0.00	0.00	16.53	9.05	0.00	0.00	0.00	0.00
1388C60	0.00	74.13	0.00	0.00	0.00	0.00	25.87	0.00	0.00	0.00	0.00	0.00	0.00
13D180C	3.29	50.94	0.00	0.00	0.00	0.00	45.77	0.00	0.00	0.00	0.00	0.00	0.00
1388C84	9.69	23.97	0.00	4.71	0.00	0.00	31.23	30.40	0.00	0.00	0.00	0.00	0.00
1388CE4	2.11	93.73	0.00	3.39	0.00	0.00	0.00	0.77	0.00	0.00	0.00	0.00	0.00
1388C9C	0.00	72.43	0.00	0.00	4.31	0.00	13.02	10.24	0.00	0.00	0.00	0.00	0.00
1388C5E	7.24	22.18	29.75	40.83	0.00	0.00	0.00	0.00	0.00	0.00	0.00	0.00	0.00
1388C49	30.59	53.79	0.00	0.38	2.04	0.00	13.19	0.00	0.00	0.00	0.00	0.00	0.00
1388C76	0.00	38.63	0.00	1.94	0.00	0.00	58.77	0.66	0.00	0.00	0.00	0.00	0.00
1388CCE	0.57	99.43	0.00	0.00	0.00	0.00	0.00	0.00	0.00	0.00	0.00	0.00	0.00
1388C74	32.75	58.27	0.00	0.00	0.00	0.00	1.30	7.68	0.00	0.00	0.00	0.00	0.00
1388CAC	0.00	0.00	0.00	0.00	0.00	0.00	56.98	43.01	0.00	0.00	0.00	0.00	0.00
1388C63	1.19	45.95	0.00	0.00	0.00	0.00	0.00	45.94	6.93	0.00	0.00	0.00	0.00
1388C38	2.37	1.66	14.76	80.68	0.00	0.00	0.52	0.00	0.00	0.00	0.00	0.00	0.00
1388C7D	0.00	41.19	0.00	39.19	0.00	0.00	15.04	0.00	4.58	0.00	0.00	0.00	0.00
1388C8A	0.00	1.45	0.00	41.26	0.00	0.00	11.89	42.55	2.84	0.00	0.00	0.00	0.00
1388C8D	0.00	97.49	1.56	0.00	0.00	0.00	0.22	0.00	0.72	0.00	0.00	0.00	0.00
1388C55	0.00	68.12	0.00	0.00	0.00	0.00	0.00	30.42	1.46	0.00	0.00	0.00	0.00
1388C86	20.67	79.33	0.00	0.00	0.00	0.00	0.00	0.00	0.00	0.00	0.00	0.00	0.00
13D180B	0.00	91.90	8.10	0.00	0.00	0.00	0.00	0.00	0.00	0.00	0.00	0.00	0.00
1388CDC	0.00	12.67	0.00	0.00	0.00	0.00	86.98	0.34	0.00	0.00	0.00	0.00	0.00
1388CBA	0.00	87.31	1.26	0.00	0.00	0.00	11.42	0.01	0.00	0.00	0.00	0.00	0.00
13D180F	0.00	55.34	0.00	26.58	0.00	0.00	18.08	0.00	0.00	0.00	0.00	0.00	0.00
1388CCA	0.00	67.43	0.00	3.47	0.00	0.00	28.70	0.00	0.40	0.00	0.00	0.00	0.00
1388C8B	10.90	68.60	20.37	0.00	0.00	0.00	0.00	0.12	0.00	0.00	0.00	0.00	0.00
1388CC1	0.00	0.00	0.00	18.76	0.00	0.00	79.65	0.00	0.00	1.59	0.00	0.00	0.00
1388C6E	0.00	63.78	4.40	0.00	0.00	0.00	0.00	21.41	10.41	0.00	0.00	0.00	0.00
1388C70	2.67	19.58	0.00	0.00	10.04	0.00	35.62	7.40	24.69	0.00	0.00	0.00	0.00
1388C42	72.88	23.47	0.49	0.12	0.00	0.00	0.00	0.00	3.05	0.00	0.00	0.00	0.00
1388CBB	0.00	83.03	0.00	16.97	0.00	0.00	0.00	0.00	0.00	0.00	0.00	0.00	0.00
1388C68	10.27	89.63	0.00	0.00	0.00	0.00	0.10	0.00	0.00	0.00	0.00	0.00	0.00
1388CCC	16.41	74.56	0.00	1.66	0.00	0.00	0.00	7.37	0.00	0.00	0.00	0.00	0.00
1388C3A	0.00	83.32	0.07	0.00	0.00	0.00	16.61	0.00	0.00	0.00	0.00	0.00	0.00
1388C57	0.00	62.01	0.00	28.11	0.00	0.00	10.60	1.48	0.00	0.00	0.00	0.00	0.00
1388C7E	0.00	47.72	22.53	0.00	0.00	0.00	29.75	0.00	0.00	0.00	0.00	0.00	0.00

Continued on next page

Handle	Breccia	Porphyry	Topaz Fragment	Andelusite Quartzite	Chlorite Quartzite	Dacite	Sericite Quartzite	Volcaniclastic	Andesite	Sericite Schist	Siltstone	Talc Schist	Clastic Sediment
1388CDB	0.00	12.74	0.00	0.00	0.00	0.00	84.84	2.43	0.00	0.00	0.00	0.00	0.00
1388CB6	5.31	58.40	0.00	0.00	0.00	0.00	0.00	36.29	0.00	0.00	0.00	0.00	0.00
1388C50	0.00	17.73	0.00	0.00	0.00	0.00	0.00	82.27	0.00	0.00	0.00	0.00	0.00
1388C95	2.30	75.41	8.73	0.00	0.00	0.00	13.29	0.00	0.28	0.00	0.00	0.00	0.00
1388C53	0.00	28.38	0.00	14.11	0.00	0.00	7.54	49.97	0.00	0.00	0.00	0.00	0.00
1388C5C	2.23	34.02	0.00	0.00	0.00	0.00	0.38	63.38	0.00	0.00	0.00	0.00	0.00
1388C78	41.52	7.75	0.00	0.00	0.00	0.00	9.00	41.73	0.00	0.00	0.00	0.00	0.00
1388CA0	0.00	35.42	3.05	0.00	0.39	0.00	52.69	0.56	7.89	0.00	0.00	0.00	0.00
1388C7A	0.00	8.13	0.00	0.00	0.00	0.00	77.01	14.86	0.00	0.00	0.00	0.00	0.00
1388CD1	0.00	42.20	0.00	0.25	0.00	0.00	27.85	29.70	0.00	0.00	0.00	0.00	0.00
1388C44	2.31	37.38	0.00	8.59	0.00	0.00	51.72	0.00	0.00	0.00	0.00	0.00	0.00
13D181B	0.00	87.02	0.00	0.00	0.00	0.00	0.00	0.00	12.98	0.00	0.00	0.00	0.00
1388CC4	0.77	54.18	17.30	0.00	0.00	0.00	27.75	0.00	0.00	0.00	0.00	0.00	0.00
1388C80	16.81	42.20	0.00	0.00	0.00	0.00	5.14	19.76	16.08	0.00	0.00	0.00	0.00
1388C6D	1.63	70.86	0.00	0.00	0.00	0.00	1.41	22.95	1.19	0.00	0.00	0.00	1.96
1388CA8	0.00	30.84	0.00	0.00	0.01	0.00	56.22	0.00	7.88	5.06	0.00	0.00	0.00
1388C48	0.00	87.10	0.00	0.00	0.00	0.00	0.00	3.34	9.57	0.00	0.00	0.00	0.00
1388CC2	0.00	10.09	0.00	6.00	0.00	0.00	77.88	5.13	0.00	0.90	0.00	0.00	0.00
1388CB1	4.42	75.77	7.47	0.00	0.00	0.00	1.80	8.17	2.36	0.00	0.00	0.00	0.00
1388CC5	0.00	78.71	0.26	0.00	0.00	0.00	10.35	7.49	3.18	0.00	0.00	0.00	0.00
1388CC0	0.61	27.67	0.00	17.52	0.52	0.00	53.68	0.00	0.00	0.00	0.00	0.00	0.00
1388CD3	0.00	8.31	0.00	0.00	0.00	0.00	45.20	46.50	0.00	0.00	0.00	0.00	0.00
1388CAD	0.00	75.86	0.00	0.00	0.00	0.00	2.21	1.84	20.10	0.00	0.00	0.00	0.00
1388C4A	0.00	9.82	0.00	32.23	0.00	0.00	57.95	0.00	0.00	0.00	0.00	0.00	0.00
1388C7C	0.00	33.36	0.00	2.05	0.00	0.00	1.72	62.87	0.00	0.00	0.00	0.00	0.00
1388C89	46.73	33.19	0.00	0.00	0.00	0.00	14.54	1.13	0.00	4.40	0.00	0.00	0.00
1388CAA	0.00	76.91	0.00	0.00	0.00	0.00	4.17	0.02	11.07	7.84	0.00	0.00	0.00
1388CD0	67.74	18.49	0.00	0.00	0.00	0.00	13.77	0.00	0.00	0.00	0.00	0.00	0.00
13D180E	0.00	80.64	0.00	0.00	0.00	0.00	14.03	1.92	3.41	0.00	0.00	0.00	0.00
1388CAB	1.47	55.40	0.00	0.00	0.00	0.00	9.28	33.86	0.00	0.00	0.00	0.00	0.00
1388C47	0.00	97.54	0.00	0.00	0.00	0.00	0.00	2.46	0.00	0.00	0.00	0.00	0.00
1388C87	10.99	49.27	0.00	3.81	1.56	0.00	32.32	2.06	0.00	0.00	0.00	0.00	0.00
80	44.86	48.07	0.00	0.00	0.00	0.00	4.73	2.34	0.00	0.00	0.00	0.00	0.00
1388C4E	4.41	77.93	13.26	3.25	0.00	0.00	0.00	1.15	0.00	0.00	0.00	0.00	0.00
1388CC9	0.00	98.20	0.00	1.79	0.00	0.00	0.00	0.00	0.00	0.00	0.00	0.00	0.00
1388CBD	0.00	0.00	0.00	0.00	0.00	0.00	96.13	0.00	3.84	0.03	0.00	0.00	0.00
1388C8F	0.00	23.80	0.00	0.00	0.00	0.00	76.20	0.00	0.00	0.00	0.00	0.00	0.00
1388C92	0.00	9.46	0.00	0.00	0.00	0.00	0.00	90.54	0.00	0.00	0.00	0.00	0.00
1388CD8	5.61	9.82	0.00	5.99	0.00	0.00	78.58	0.00	0.00	0.00	0.00	0.00	0.00
1388C77	0.00	17.23	0.00	11.59	0.17	0.00	11.81	59.19	0.00	0.00	0.00	0.00	0.00
1388C7B	22.37	57.56	0.00	0.00	0.00	0.00	0.00	20.07	0.00	0.00	0.00	0.00	0.00
1388CA4	0.00	0.00	0.00	0.00	0.00	0.00	34.47	65.51	0.02	0.00	0.00	0.00	0.00
1388C46	0.02	92.71	0.00	0.00	0.00	0.00	3.70	3.56	0.00	0.00	0.00	0.00	0.00
1388C56	0.00	88.49	1.07	0.00	0.00	0.00	0.00	8.51	1.93	0.00	0.00	0.00	0.00
1388C9E	2.96	46.84	0.00	0.00	0.00	0.00	0.00	50.20	0.00	0.00	0.00	0.00	0.00
1388C83	1.89	76.87	0.00	0.00	0.00	0.00	1.04	20.20	0.00	0.00	0.00	0.00	0.00
1388CE0	0.00	0.00	0.00	26.89	0.00	0.00	57.39	15.72	0.00	0.00	0.00	0.00	0.00
1388CCD	0.00	81.07	5.61	0.00	0.00	0.00	0.00	7.53	5.55	0.00	0.00	0.00	0.24